PhD Thesis

Depth resolved stress gradient and dislocation analyses in III-N multilayer structures

Michael Andreas REISINGER

Montanuniversität Leoben
Department of Materials Physics

November 2017

This work was funded by the Austrian Research Promotion Agency (FFG, Project No. 860424).

© 2017 Michael Andreas REISINGER

All rights reserved

Department of Materials Physics

Montanuniversität Leoben

Jahnstraße 12

8700 Leoben, Austria

Affidavit

I declare in lieu of oath, that I wrote this thesis and performed the associated research myself, using only literature cited in this volume.

Leoben, November 2017

Acknowledgments

I would like to express my gratitude towards all people, who have supported me both, professionally and personally. In particular I want to thank following persons:

Prof. Jozef Keckes, my supervisor, for guiding me patiently on my way through the PhD studies. I am grateful for our numerous scientific discussions and his always open door, which have been a great support. I am also thankful, that he send me to several interesting conferences and workshops, where I got the possibility to present my scientific results.

Johannes Zechner, who coordinated our research at Montanuniversität in Leoben with the interests of our collaborating company Infineon/KAI in Villach. Many prosperous ideas and inspirations were gained during our scientific discussions at work as well as at ski touring in the mountains.

Jakub, for introducing me into the world of TEM. He has been a great help in various professional as well as personal situations and I really appreciate our friendship. Rainer Lechner, who helped me to perform and analyse my XRD experiments. Gabi for preparing a multitude of TEM samples. Sabine and Daniela, our secretaries, who have had to deal with my sometimes insufficient travel expense reports and times sheets. The rest of our research group, Juraj, David, Michael, Tobias and Sabine which was a great support. My former and present office mates and friends, Karoline, Thomas, Zhou, Manuel and Alexander, for many cheerful distractions as well as private and scientific discussions. All my colleagues and friends at ESI, which I might have missed here for the great working environment, the day-to-day discussions and support.

I am also deeply grateful to KAI and Infineon Austria, for giving me the financial support and the opportunity to carry out this thesis. In particular, I would like to thank Manuel Tomberger, Ingo Daumiller, Clemens Ostermaier and Lauri Knuuttila for providing samples and discussing GaN as well as deposition process related questions.

All co-workers from various research departments, who have invited me to perform analyses on their facilities.

My wife Raffaela, for her great love and understanding of the long working days of PhD students. Together with my family and friends, she created the background required for my successful PhD studies

Abstract

III-N semiconductor materials possess superior physical properties, which make them very attractive for various optoelectronic and microelectronic applications. Despite their great features, such as the large band gap energy, the high critical electric field and the superior thermal and chemical stability, III-N materials have not been well-established at the semiconductor market, yet. A major challenge for the industrial growth of III-N structures, is the lack of economically reasonable substrate materials, which fulfil all significant requirements, such as electric and thermal conductivity, compatible crystal structure and negligible thermal and lattice mismatch. In the semiconductor industry, the mainly used substrate materials are SiC, Al_2O_3, and Si.

Due to its attractive economical features combined with good electrical properties, Si substrates are very promising for the application in the microelectronic sector. The major drawbacks of Si substrates are the large lattice and thermal mismatches with respect to III-N semiconductors. In order to compensate these mismatches and to fulfil all electronic requirements, III-N structures are usually grown as multilayer stacks. Although the overall stress is negligible, there are locally high sublayer stress concentrations, which have a significant influence on the reliability of the actual device.

The stress profile of various high electron mobility transistors (HEMTs) deposited on Si have been characterized. Typically, a HEMT is based on $Al_xGa_{1-x}N$ alloys and consists of a nucleation-, a transition-, a buffer- as well as a thin barrier-layer on top. For a comparative study, there have been applied several techniques based on (i) focused ion beam milling combined with digital image correlation (FIB-DIC) (ii) transmission electron microscopy (TEM), (iii) X-Ray diffraction, (iv) wafer curvature and (v) Raman spectroscopy.

All analyses have indicated a high tensile stress in the nucleation layer, a compressive to tensile stress transition in the transition layer and tensile stress within the buffer layer. Subsequently, the stress profiles have been correlated with the sublayer microstructures using TEM. The comparison of different heterostructures has shown, that the transition layer design has a significant impact on the microstructure and the stress gradient across the multilayer stack. In a final step, the advantages and disadvantages of the individual techniques have been discussed.

Kurzfassung

Aufgrund besonderer Eigenschaften, wie der großen Bandlücke, der hohen kritischen Feldstärke und der guten Thermostabilität, besitzen III-N Halbleiter ein großes Potential für verschiedenste optoelektronische und mikroelektronische Anwendungen. Jedoch kann dieses Potential noch nicht voll ausgeschöpft werden. Ein Hauptgrund ist das Fehlen kostengünstiger Substrate, die alle wichtigen Voraussetzungen erfüllen. Entscheidend sind unter anderem der Unterschied zwischen den Gitterkonstanten als auch der thermischen Ausdehnungskoeffizienten und die thermische bzw. elektrische Leitfähigkeit des Substratmaterials. Mögliche Substrate für III-N Wachstum sind SiC, Al_2O_3 und Si.

Aus wirtschaftlichen Aspekten kommen in der Mikroelektronik jedoch vermehrt Si Substrate zum Einsatz. Der große Nachteil von Si Substrate ist allerdings der große Unterschied zwischen den Gitterkonstanten sowie der Ausdehnungskoeffizienten. Um diese Unterschiede auszugleichen, werden zuerst verschiedenste Zwischenschichten gewachsen, welche das Fundament für die eigentliche Transistorstruktur bilden. Obwohl die mittlere Spannung des fertigen Mehrlagensystems meist vernachlässigbar klein ist, kommt es in den verschiedensten Einzelschichten lokal zu sehr starken Eigenspannungsspitzen. Diese haben einen negativen Einfluss auf die Zuverlässigkeit und bestimmen unter anderem die Lebensdauer und Leistungsfähigkeit des Transistors.

In dieser Arbeit wurden die Eigenspannungsgradienten von verschiedenen Transistor Strukturen, welche aus mehreren $Al_xGa_{1-x}N$ Schichten bestehen, untersucht. Bei den einzelnen Schichten unterscheidet man zwischen einer Ankeim-, einer Übergangs-, einer Buffer- und einer Sperr-Schicht. Um einzelne Untersuchungsmethoden vergleichen zu können, wurden folgende Messtechniken angewendet: (i) Fokussierter Ionen Strahl in Kombination mit digitaler Bildkorrelation, (ii) Transmissionselektronenmikroskop, (iii) Röntgenbeugung, (iv) Wafer Krümmung und (v) Raman Spektroskopie.

Alle Analysen zeigten hohe Zugspannungen in der Ankeimschicht, einen Wechsel von Druck auf Zugspannung in der Übergangsschicht und eine moderate gleichbleibende Zugspannung in der Bufferschicht. Die Korrelation des Spannungsprofiles mit der Mikrostruktur der Einzelschichten zeigt, dass der Aufbau der Übergangsschicht eine tragende Rolle für das Eigenspannungsgradienten des Mehrlagensystems spielt. Am Ende wurden die Vor- und Nachteile der einzelnen Analysemethoden diskutiert.

Contents

Affidavit V

Acknowledgments VII

Abstract IX

Kurzfassung XI

1. Introduction 1

1.1 Overview of III-N semiconductors 2

1.2 Properties of III-N semiconductor structures 4

2. Challenges in the growth of AlGaN structures 9

2.1 Substrates for commercial AlGaN epitaxy 9

2.2 Growth and design of HEMT structures on Si(111) substrates 12

2.3 Defect and stress formation in AlGaN structures 16

2.4 Defect and stress related phenomena in AlGaN devices 19

3. Methods for stress and defect analyses of HEMT structures 21

3.1 Focused Ion Beam – Digital Image Correlation methods (FIB-DIC) 21

3.2 Transmission Electron Microscopy (TEM) 27

3.2.1 High Resolution Transmission Electron Microscopy (HRTEM) *27*

3.2.2 Precession Electron Diffraction (PED) *31*

3.2.3 Scanning Transmission Electron Microscopy (STEM) *35*

3.3 X-ray Diffraction (XRD) 37

3.4 Wafer Curvature 43

3.5 Raman Spectroscopy 47

3.6 Advantages and disadvantages of the applied stress analyses 53

4. Bibliography 59

5. List of Appended Publications 65

5.1 Papers in Scientific Journals 65

5.2 Contribution of the authors to the papers 66

A. Cross-sectional stress distribution in $Al_xGa_{1-x}N$ heterostructure on Si(111) substrate characterized by ion beam layer removal method and precession electron diffraction 67

A.1 Introduction 68

A.2 Experiment 70

A.3 Results 75

A.4 Discussion 79

A.5 Conclusion 82

B. Resolving alternating stress gradients and dislocation densities across $Al_xGa_{1-x}N$ multi-layer structures on Si(111) 89

B.1 Introduction 90

B.2 Experiments 91

B.3 Results and Discussion 93

B.4 Conclusion 100

B.5 Supplementary Material 104

C. Matching *in-situ* and *ex-situ* recorded stress gradients in an $Al_xGa_{1-x}N$ heterostructure: Complementary wafer curvature analyses in time and space 109

C.1 Introduction 110

C.2 Experiment 111

C.3 Results and Discussion 114

C.4 Conclusion 120

1 Introduction

For decades, silicon has been the material of choice in semiconductor based transistors. The undisputed success and dominant position of silicon is owed however more to economic and production related considerations than outstanding electronic properties. In the main, Si has a good availability in combination with relatively low costs. However, ever rising demands from the microelectronic industry, means, that Si based transistors are pushed closer and closer to their physical limits within high-power and high-frequency applications. This development opens up new possibilities for a new class of transistor materials. One very promising class of successors is the group of III-N semiconductors.

In particular, GaN has outstanding electrical properties which can be exploited in many microelectronic as well as optoelectronic applications. Unique features, as a wide direct bandgap, piezoelectric characteristics as well as superior thermal and chemical stability offer the potential for III-N based structures to dominate the future market of high-speed and high-power transistors. In order to realise this potential however, a number major issues still have to be resolved. One significant challenge is the lack of available and low cost substrate materials, compatible to III-N structures. In consequence, III-N structures still suffer from high residual stress states caused by thermally induced and lattice mismatches between the used substrate materials and the deposited semiconductor structures. The presence of residual stress downgrades the film crystal quality, and consequently the performance of the actual later devices. In order to cope with this issue, the semiconductor industry has developed various heterostructure designs, which counterbalance mismatches between substrates and device structures.

In the industry, the residual stress of developed heterostructure designs is usually evaluated using wafer curvature techniques, Raman spectroscopy and/or X-ray diffraction. Neither of these commonly used techniques offers the ability to reveal critical local stress

concentrations. However, high stress concentrations have a significant impact on the cracking behaviour as well as the generation of dislocations, which determine the later reliability of the actual device.

The prime focus of this thesis is, as a first step to find and develop suitable approaches, for the evaluation of multilayer stress gradients. As a second step, the aim is to improve the employed techniques, in terms of resolution and accuracy. Subsequently, the stress concentrations have been correlated microstructural features (e.g. dislocations). Such basic understanding is crucial for the development of appropriate multilayer designs. In addition, critical process steps can be defined, in order to tune deposition parameters in an even more sophisticated manner. The thesis closes with a discussion of the applicability, advantages and disadvantages of the techniques employed.

1.1 Overview of III-N semiconductors

In general III-N semiconductors belong to the class of III-V semiconductors. Depending on the containing group V element, one can distinguish between different material systems as (i) nitrides (III-N), (ii) arsenides (III-As) and (iii) phosphides (III-P).

Since the physical properties of semiconductors are highly influenced by the underlying band structure, the semiconductor industry has used alloying for tuning the band structure and the electrical and the optical characteristics [1]. Hence, III-N semiconductors are often synthesised as ternary (InGaN, AlGaN, InAlN) and quaternary (InAlGaN) alloys of the individual binary (GaN, AlN, InN) compounds [2].

The chart in Figure 1 shows an overview of different III-V systems, where the band gap energy levels (E_g) of III-N (blue), III-As (red) and III-P (green) are plotted against the corresponding lattice parameter a [3].

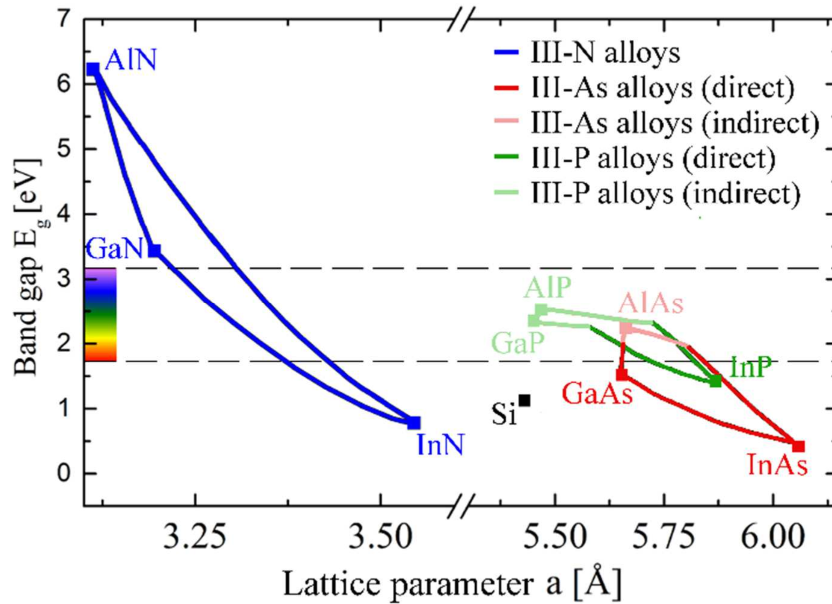

Figure 1.: The band gap energies E_g of III-V systems and Si are plotted against the lattice parameter a at room temperature: III-N (blue), III-As (red), III-P (green), Si (black). Different colours indicate direct band gap alloys (dark blue, dark red, dark green) and indirect band gap alloys (light red, light green, black). Two lines mark the energy range of the visible spectrum. Data were taken from Vurgaftman *et. al.* [4] and Zhu *et. al.* [3].

As depicted, III-N structures continuously cover band gap energies in the range of 0.8 eV to 6.2 eV, whereas III-As and III-P systems are limited to the region of about 0.4 eV to 2.4 eV and 1.4 eV to 2.4 eV, respectively. Hence, solely III-N materials can be employed as short wavelength emitters (blue light).

Another advantage of III-N semiconductors is, that the band gap remains direct over the entire compositional range. In contrast, III-As alloys and III-P alloys both exhibit, direct and indirect band gap behaviour. As indicated by the colour change in Figure 1 (dark red to light red and dark green to light green), the band gap type changes from direct to indirect for compositions with large energy band gaps [4]. Hence, III-N systems are able to emit photons more efficiently over the entire visible spectrum, which gives them a great potential for optoelectronic applications such as light emitting diodes (LEDs), laser diodes and photodetectors [3]. For electrical applications, it was found that the broad range of band

gap energies results in rather high bulk material breakdown voltages [5]. Consequently, III-N structures are well suited for the application in high-power-high frequency devices, such as high electron mobility transistors (HEMTs) and metal oxide semiconductor field effect transistors (MOSFETs) [6].

1.2 Properties of III-N semiconductor structures

The outstanding properties of III-N semiconductor materials have made them very attractive for various applications in electronic and optoelectronic devices. In general, III-N materials can crystallise in three different phases: (i) wurtzite, (iii) zinc blende and (iii) rock salt. Under ambient conditions, the wurtzite crystal structure is thermodynamically stable for bulk AlN, GaN and InN. Since the rock salt structure only appears under high pressure conditions, there is no significant technological importance for this phase. The metastable zinc blende phase can be epitaxially grown on various substrates. In the literature there has been reports comparing the electrical and optical properties of hexagonal wurtzite GaN with those of its cubic zinc blende form [7].

The prime focus of this thesis is on the investigation of hexagonal GaN alloys, which are commercially more significant than the zinc blende polytype. As a result, the subsequent sections are concerned solely with wurtzite III-N structures, as shown in Figure 2. There a hexagonal GaN crystal structure (black contours) is visualised by stick and ball model. The crystal consists of Ga^{3+} cations (red balls) and N^{3-} anions (blue balls), which are bonded ionically (grey sticks). Since this structure does not have any mirror plane, being perpendicular to the c-axis, there are non-polar ($\{kh0\}$ e.g. c-planes), semi-polar ($\{khl\}$ as well as polar ($\{00l\}$ e.g. m-plane) crystal cuts possible, with particular $\{khl\}$ planes parallel to the surface (see Figure 2b). Since the semiconductor industry takes advantage of polarisation characteristics, GaN thin films are frequently grown in polar plane orientation, where the direction of growth is perpendicular to the m-plane with either N^{3-} or Ga^{3+} on top.

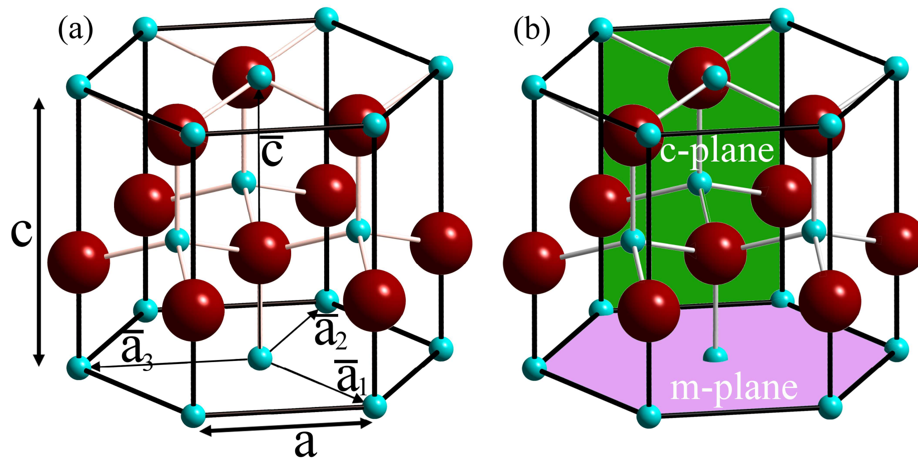

Figure 2: Stick and ball model of a wurtzite GaN crystal structure. The Ga (red) and the N (blue) atoms are ionically bonded (grey sticks). (a) The model indicates the lattice parameters a and c and the unit cell vectors ($\bar{a}_1$, $\bar{a}_2$, $\bar{a}_3$, $\bar{c}$) and (b) the c-plane and m-plane (b).

As already stated, III-N semiconductors and their alloys cover a band gap energy range from 0.8 eV to 6.2 eV. The large spectrum is a direct consequence of the strong ionic bonds between the group III element (Al, Ga or In) and N. As a result, III-N semiconductors based light emitting diodes can operate highly efficient at a wavelength spectrum, ranging from ultraviolet (UV) to the infrared (IR).

The microelectronic industry takes advantage of the large energy band gap as well. Based on the large gap, III-N structures can withstand impact ionization even under high potentials. Thus they have a very high critical electric field (E_c), which determines the limit before an avalanche breakdown is induced. As a consequence, very confined drift regions can be achieved [8].

Based on the polar crystal structure, III-N semiconductors show a strong piezoelectric behaviour. This means, that already minor lattice distortions generate high electric fields. The semiconductor industry came up with a way to exploit this effect in order to enhance the performance of microelectronic structures, by the formation of highly conductive regions. However, for the achievement of certain characteristics, it is crucial to control the

lattice strain within the grown structure. This requires to set certain strain conditions by the growth of a specific hetero-interface (e.g. GaN/$Al_xGa_{1-x}N$). Such an interface defines the piezoelectric polarisation in a controlled manner and forms a two-dimensional electron gas (2DEG). This region, having a thickness of only a few atoms, has a very high carrier concentration in the range of $n_s > 10^{13}$ cm^{-2} at room temperature. In addition to the high carrier concentration, the confined dimension increases the electron mobility (μ_n) from about 1000 cm² V^{-1} s in unstrained bulk GaN to 1500 cm² V^{-1} s to 2000 cm² V^{-1} s within the 2DEG [8]. Due to the superior combination of high carrier concentration with enhanced electron mobility the 2DEG provides a very efficient drift region for carrier transport within microelectronic applications [8]. Since the exact properties of the 2DEG depend on a multitude of different parameters, such as alloy composition, strain state, layer thickness, crystal quality, doping level as well as polarity, the device characteristic can be tuned by employing an appropriate hetero-interface design [9], [10].

Also, the high saturation electron velocity (υ_s), which is based on the unique characteristic of the conduction band, enhances the conductivity of III-N semiconductors. As a result, high electric fields have a positive impact, even in comparison with other wide-band-gap materials [11], [12].

Additionally, the strong ionic bonding gives rise to superior thermal and chemical stabilities, as well as the relatively high thermal conductivity. Hence, depending on the used substrate heat dissipates well and the device can sustain relatively high operational temperatures. Additionally, the device lifetime benefits from the high resistance of III-N structure against chemical and thermal degradation.

The combination of all these features (high conductivity, high operation voltage, high thermal and chemical stability) enables the realization of superior power densities. This means, that III-N structures are well suited for micro-electronic down scaling and high-power applications.

A comparison of crucial material properties is provided for III-N semiconductors (GaN and AlN) with competing semiconductor materials (Si, 4H-SiC, AlN, GaAs) in Table 1. Apparently, GaN has great high field transport properties. Particularly within the 2DEG

region, the achievable power density output is significantly higher than within other commercial semiconductor structures.

	GaN	Si	GaAs	4H-SiC	AlN
Lattice Constant [3]					
a (Å)	3.189	5.431	5.451	3.073	3.112
c (Å)	5.185			10.053	4.982
Crystal Structure [5]	W	D	Z.B.	W	W
Band Gap Type [13]	direct	indirect	direct	indirect	direct
Band Gap Energy [13]					
E_g (eV)	3.39	1.12	1.43	3.26	6.28
Break Down Field (T = 300 K) [13]					
E_c ($10^6 \cdot V \cdot cm^{-1}$)	3.3	0.3	4.0	2.0	11.7
Carrier Mobility (T = 300 K) [13]					
μ_n ($cm^2 \cdot V^{-1} \cdot sec$)	1500*	1350	8500	720	1100
Thermal Conductivity [13]					
κ ($W \cdot cm^{-2} \cdot K^{-1}$)	1.3	1.5	0.5	4.5	3.4
Saturation Velocity (T = 300K) [14][15]					
υ_s ($10^6 \cdot cm \cdot sec^{-1}$)	25	10	17	20	14
Opertation Temperature limit [16]					
T_{max}(°C)	700	300	300	600	-

Table 1.: Some key properties of commonly used semiconductor materials, with wurtzite (W), diamond (D) and zinc blende (Z.B.) structure. The data were taken from Quay *et. al* [5], Zhu *et. al.* [3], Kamata *et. al.* [13], Lidow *et. al.* [8], Flack *et. al.* [14], Pengelly*et.al.* [16].

* The carrier mobility for the 2DEG region of a $GaN/Al_xGa_{1-x}N$ interface [8].

2

Challenges in the growth of AlGaN structures

Due to the superior physical properties of III-N semiconductors, the growth of high quality III-N heterostructures has been studied extensively in the semiconductor industry. In 1969, the first GaN films were grown epitaxially with poor crystal quality on a sapphire substrate by using hydride vapour phase epitaxy (HVPE) [17]. Since then, the GaN crystal quality has been successively improved by introducing various buffer layer designs and tuning the deposition parameters [18].

2.1 Substrates for commercial AlGaN epitaxy

Today $Al_xGa_{1-x}N$ structures are commonly grown by using metal-organic-chemical-vapour-deposition (MOCVD) or molecular beam epitaxy (MBE). However, there is still a large gap between the theoretical material properties, as listed above and the achievable device characteristics. A major obstacle for the fabrication of high quality III-N devices is the lack of high quality bulk III-N substrate materials. Hence, there is no native substrate material with equal physical properties available and III-N structures have to be grown by heteroepitaxy on foreign substrates as Al_2O_3 (sapphire), 6H-SiC and Si [14], [19].

In practice the substrate characteristics strongly influence the final device performance. Consequently, substrate properties which have to be considered are (i) crystal structure (lattice parameter – a, c and mismatch to III-N film), (ii) thermal properties (expansion coefficient (CTE) – α_a, α_c and heat conductivity – κ), (iii) electrical properties (resistivity - ρ), (iv) economical considerations (price and availability of large diameter wafers), (v) quality issues (crystal, defect density, surface quality and wafer bow) as well

as (vi) mechanical and chemical properties (for manufacturing process and device operation) [5]. Table 2. lists the most important properties of commonly used substrate materials (Al_2O_3, 6H-SiC, Si).

The overview in Table 2. shows, that due to its physical properties, such as small lattice mismatch, the negligible mismatch as well as the good thermal conductivity, 6H-SiC looks like a perfect substrate material for GaN epitaxy. However, its very high price limits the utilization of 6H-SiC substrates in GaN growth on an industrial scale. The second option, Al_2O_3 shows inferior thermal conductivity, limiting it's applicability as substrate for high-power devices. A second reason for its limited applicability is the high price and that six inches is the maximal size of available high quality wafers. Nevertheless, Al_2O_3 substrates are the first choice for GaN based LEDs [18]. Although Si has the largest lattice and thermal mismatch with respect to GaN, it seems to be the only economically reasonable option for electrical applications. Especially for cost-sensitive mass product devices, such as automotive converters, Si has the highest significance of all substrate materials in the semiconductor industry. There is a good supply of large high quality wafers (8 and 12 inch) and Si/GaN structures can be easily integrated into the well-established processes of Si technology [20]. Due to its three-fold surface symmetry, Si(111) wafer represents the best suited orientation for the growth of wurtzite $Al_xGa_{1-x}N$ structures with an epitaxial relationship of (0001) $Al_xGa_{1-x}N$ parallel to (111) Si and $(11\bar{2}0)$ $Al_xGa_{1-x}N$ parallel to $(1\bar{1}0)$ Si [3]. Furthermore, in this configuration the in-plane thermal expansion mismatch can be reduced to about ~56%. Nevertheless, the rather high differences in lattice spacing and CTEs induce tensile stress formation in $Al_xGa_{1-x}N$ during film growth and subsequent cooling from deposition to room temperature. Hence, there is a significant negative impact on crystal quality due to the presence of (i) wafer bow, (ii) lattice strain, (iii) lattice defects and (iv) microcracks, which have to be prevented with a dedicated multilayer design and deposition process.

	Al_2O_3	Si	6H-SiC
Lattice Constant [3]			
a (Å)	4.759	5.431	3.081
c (Å)	12.991		15.117
Lattice Mismatch [3]			
to GaN (%)	-16.0	17.0	-3.5
to AlN (%)	-13.3	19.0	-1.0
Thermal Conductivity [5]			
κ (W cm^{-1} K^{-1})	0.5	1.5	4.9
CTE [3]			
α_a (10^{-6} K^{-1})	7.3	2.6	4.46
α_c (10^{-6} K^{-1})	8.5	2.6	4.16
Thermal Expansion Mismatch, *a* [3]			
to GaN (%)	-23.4	-115	-25.3
to AlN (%)	-43.2	-60	7.0
Resistivity [5]			
ρ (Ω cm)	$\geq 10^{11}$	$\geq$ 1-3 10^4	$\geq 10^{11}$
Relative Costs [6]	high	low	very high

Table 2.: Overview of the basic properties of the major substrate materials for GaN epitaxy. The data were taken from Zhu *et. al.* [3], Quay *et. al.* [5], Su *et. al.* [6].

2.2 Growth and design of HEMT structures on Si(111) substrates

HEMTs are the most common GaN based structures for high-power applications, such as power amplifiers and power switches. As previously stated, the most significant deposition processes are MOCVD and MBE, with typical deposition temperatures (T_D) of T_D > 1000°C and T_D = ~700°C, respectively. Although MBE allows for the growth of highly precise interfaces, MOCVD is the technique favoured for wafer deposition on industrial scale. The main reasons for this are of economic nature, e.g. lower production costs due to higher deposition rates (typically 2 µm/h). There are also reports, where both techniques are combined, in particular so-called migration enhanced MOCVD [5,8].

Prior to film deposition, the wafer has to be polished and cleaned *ex-situ* in order to reduce surface roughness and to avoid reactor contamination. In the case of Si substrate, there are reports about various approaches for *in-situ* substrate annealing and cleaning in specific atmospheres (such as H_2). This step removes oxygen and improves film growth and the final crystal quality. After this pre-treatment, the actual deposition process can be started, which usually consists of successive growth of (i) AlN nucleation sublayer, (ii) $Al_xGa_{1-x}N$ transformation sublayer, (iii) GaN buffer layer and (iv) $Al_xGa_{1-x}N$ barrier layer.

There exist several reactor designs and concepts for HEMT growth via MOCVD. The schematic in Figure 3 depicts the main reactor components.

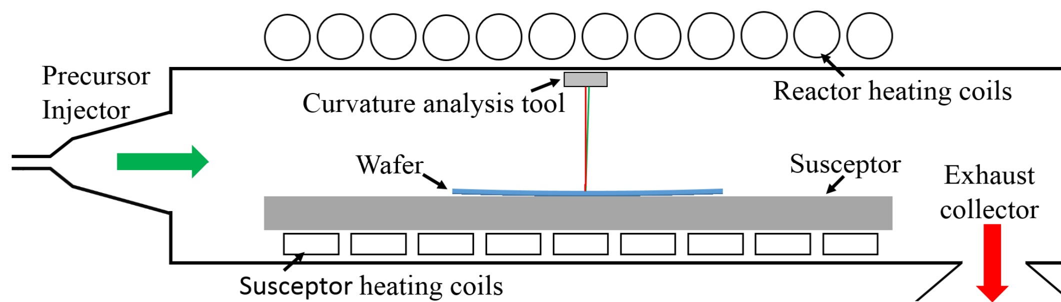

Figure 3 shows a schematic of an MOCVD reactor for epitaxial growth of HEMT structures on Si substrates.

Here the substrate is placed on top of the graphite susceptor, which is heated by coils from the bottom. The heating from solely one side causes temperature gradients and wafer bow occurs (see Figure 3) [3]. After reaching the deposition temperature, the individual precursors are injected and delivered via a carrier gas (typically H_2) to the substrate surface, where they react and form the semiconductor film. The commonly used precursors are trimethylaluminum (TMA), trimethylgallium (TMG) and ammonia (NH_3) for Ga, Al and N, respectively. The detailed chemical reactions between the TMA/TMG and NH_3 are very complex and haven not been fully understood yet. However, the principle reactions can be described via Eq.1. and Eq.2.:

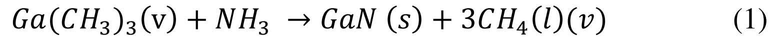

$$Ga(CH_3)_3(\mathrm{v}) + NH_3 \rightarrow GaN\ (s) + 3CH_4(l)(v) \quad (1)$$

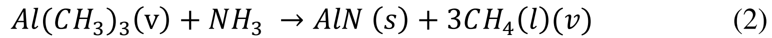

$$Al(CH_3)_3(\mathrm{v}) + NH_3 \rightarrow AlN\ (s) + 3CH_4(l)(v) \quad (2)$$

The samples which have been investigated for this thesis were grown within an Aixtron 5G planetary reactor. This reactor is capable of depositing on eight six-inch wafers simultaneously. In order to achieve uniform wafer deposition, the susceptor is rotated in a planetary motion during the film deposition. The most important tuneable process parameters are the deposition temperature and the partial precursor pressures. However, due to presence of wafer bow, the deposition parameters variate slightly across the wafer, which has to be compensated. Therefore, among others following data are recorded: deposition time, deposition temperature, surface reflectivity, reactor temperature, wafer curvature, and reactor pressure.

Figure 4 shows the schematic drawings of three different HEMT heterostructures, which have been investigated within the scope of this thesis.

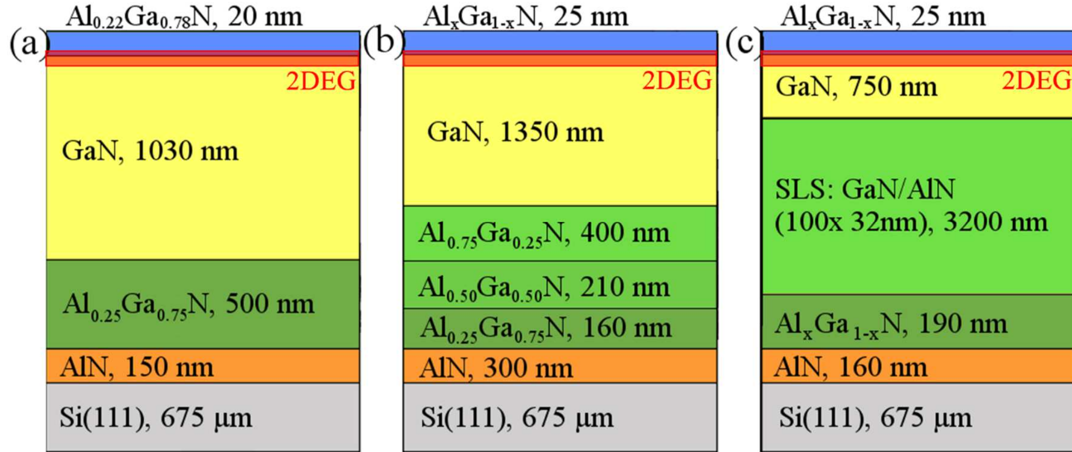

Figure 4: Schematic drawings of various HEMT heterostructures, which consist basically of a nucleation- (orange), a transition- (green), a buffer- (yellow) and a barrier-layer (blue) and which were characterised within this thesis. The 2DEG is located at the buffer/barrier interface (red).

Subsequently, the individual deposition stages (i) to (iv) and sublayers of the most extensively characterised HEMT structure (see Figure 4a) are described:

(i) First, a 150 nm thick nucleation layer was deposited on the Si(111) substrate. This nucleation layer consists of a 30 nm thick low temperature AlN (LT-AlN) section and a 120 nm thick high temperature AlN (HT-AlN) section, which were grown at deposition temperatures of 993°C and 1100°C, respectively. This two-step approach promotes threading dislocation (TD) inclination and reduces the dislocation density. The AlN layer is required, since direct contact between Ga and the Si surface should be avoided, as these elements react rather strongly, which causes Si etching. Consequently, the substrate surface becomes very rough and deteriorates crystal quality of the deposited GaN. In addition, the electrically insulating character of the AlN layer is beneficial, since it prevents parallel conduction in the Si substrate. However, there is still a large lattice and thermal mismatch between AlN and Si, which causes high tensile stress within this nucleation layer.

(ii) Secondly, a 500 nm thick $Al_{0.25}Ga_{0.75}N$ transition layer was grown, to provide an intermediate step for the transition from the smaller AlN lattice to the larger GaN lattice.

This layer grows compressively stressed at a temperature of 1086°C. The composition and the thickness of the transition layer has to be designed properly, to introduce sufficient compressive stress, to counterbalance the tensile stress, which is caused by the thermal mismatch between the $Al_xGa_{1-x}N$ heterostructure and the Si substrate during cooling from deposition to room temperature. Otherwise cooling would result into film cracking. In the literature, HEMT structures with different transition layer concepts [2,21] have been discussed. Figure 4 depicts three different kind of HEMT structure designs, which have been characterised within this thesis.

(iii) Subsequently, a 1030 nm thick GaN buffer layer was grown at 1100°C. The main purpose of this layer is the reduction of the heterostructure dislocation density and the improvement of the film crystal quality. Therefore, a certain layer thickness is required, to enable interaction reactions of dislocations, such as fusion and annihilation (see *section 2.3*). However, an increasing buffer layer thickness gives rise to larger tensile stresses during cooling. Thus, the maximal layer thickness is limited by film cracking.

(iv) Finally, a 20 nm thick $Al_{0.22}Ga_{0.78}N$ barrier layer is deposited on top of the GaN buffer layer at a temperature of 1083°C. The pseudomorphic $GaN/Al_{0.22}Ga_{0.78}N$ heterointerface provides the required lattice strain, to generate a 2DEG. This a few atom layer thick area is induced by piezoelectric polarisation and acts as electron channel for the actual later device. The properties of the 2DEG depend on many factors, such as the lattice mismatch between the GaN buffer and the $Al_xGa_{1-x}N$ barrier layer, the doping level, crystal quality as well as the barrier layer thickness. Consequently it is crucial to design the HEMT structure properly, to fulfil all requirements for later applications.

In the literature, there also have been examples shown of further approaches for the fabrication of high-quality GaN structures. One very successful technique is the epitaxial lateral overgrowth (ELO). Although this technique successfully reduces the dislocation density of GaN based structures, it is not suitable for industrial applications. Due to its many different process steps, it is a rather expensive and time-consuming process [22], [23].

2.3 Defect and stress formation in AlGaN structures

Despite the intensive research into the development of stress-compensating concepts, GaN based heterostructures grown on Si(111) are still suffering from poor crystal quality and alteration of microstructure across the wafer diameter. Various kinds of defects, such as misfit and threading dislocations (TD), stacking faults, voids and inversion domain boundaries as well as stress concentrations were found to downgrade the performance and lifetime of GaN based devices. Within HEMT structures, threading dislocations are the most critical kind of defects. Depending on the HEMT design, typically TD density values down to $10^8 – 10^{10}$ cm^{-2} within the active region can be obtained via industrial MOCVD processes [24]. However, this is still several magnitudes higher than within other semiconductor systems (e.g. 10^5 cm^{-2} for GaAs). In order to reveal the full potential of III-N structures, the number of TDs has to be further reduced.

By definition, threading dislocations are line defects, which grow through the film surface with a dislocation line ($\vec{l}$) parallel to GaN $\langle 0001 \rangle$ direction. Depending on the Burger's vector ($\vec{b}$) there can be distinguished between three different kinds of TDs, as shown in Figure 5: a-type TDs, which have edge character with $\vec{b} = \frac{1}{3}\langle \bar{2}110 \rangle$ (Figure 5a); c-type screw TDs, which have screw character with $\vec{b} = \langle 0001 \rangle$ (Figure 5b), as well as a+c type TDs, which have screw and edge character with $\vec{b} = \langle 11\bar{2}3 \rangle$ (Figure 5c). However, mixed type TDs can also appear with inclined dislocation lines in order to compensate compressive stress [25].

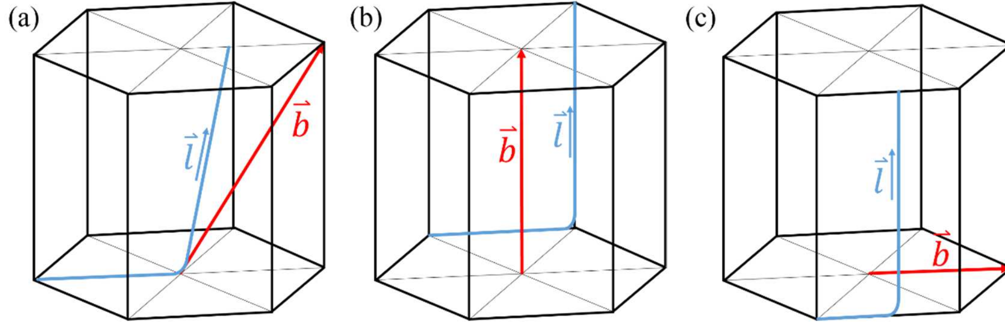

Figure 5: Geometry of the 3 different types of TDs within a hexagonal GaN unit cell: pure edge TDs (a), pure screw TDs (b), mixed type TDs with an inclined dislocation line (c) are shown.

In the main, dislocations are generated within epitaxial layers, which exceed a critical thickness. This threshold value, which is usually in the range of a few nanometers, depends on various parameters, such as lattice mismatch or growth temperature. Below the critical thickness, the formation of dislocations is energetically unfavourable and the epitaxial layers remain coherently strained. Above the critical thickness, dislocations are generated to relax coherent strain caused by lattice misfit between the substrate and the deposited layer. For large lattice-mismatched films it is energetically favourable to nucleate as isolated islands which coalesce during subsequent growth, rather than growing instantly as continuous films [26]. Consequently, TDs are formed during islands coalescence, to compensate tilt and twist misorientations of neighbouring islands, as well as during growth and cooling to relax high elastic strains Within $Al_xGa_{1-x}N$ structures a-type TDs are the dominant type of TDs, while c-type TDs are rather uncommon. Since, a+c type TDs are the only ones, which appear with inclined dislocation lines, they have a significant influence on the sublayer microstructure. Thus, they may contribute to the compensation of initial compressive stress and stress gradient formation. During subsequent layer growth inclined a+c type TDs move laterally towards other dislocations, where they meet and intersect. As a result, the dislocation density decreases by (i) dislocation annihilation or (ii) dislocation fusion reaction with the increasing film thickness [25].

However, island coalescence gives also rise to the formation of tensile stresses. After nucleation, the individual islands grow laterally and in thickness. Right before coalescence occurs, the gaps between the islands are very narrow. Tensile stress is generated by stretching of the individual islands in order to merge and to replace the two crystal/atmosphere interfaces with one grain boundary [26]. Nix and Clemens have found, that the magnitude of the tensile stress depends on the island size, the Young's modulus as well as the surface and grain boundary energy [27]. It was also reported, that the generated tensile stress has a minimum at the substrate/film interface and increases nonlinearly trough the film coalescence thickness. Since the lattice constant of AlN is smaller than GaN, within HEMT structures, $Al_xGa_{1-x}N$ and GaN layers nucleate compressively stressed on AlN and $Al_xGa_{1-x}N$ substrate layers, respectively. For these sublayers, the change in growth mode (from three dimensional island to two dimensional layer growth) and the associated tensile stress generation, would give rise to the formation of stress gradients [28], [29].

It should also be mentioned however, that in the literature there exists a second theory for the origin of stress gradients. Here, Romanov *et. al.* and Follstaedt *et. al.* have theoretically as well as experimentally described that initial compressive stress can trigger the inclination of dislocation lines [30], [31]. The inclined TDs act in place of interfacial misfit dislocations, to compensate compressive stress by tensile stress generation. In subsequent film growth the misfit segment of inclined TDs increases and the compressive stress decreases with increasing film thickness. Since inclined dislocations are "frozen in" and do not incline back, the resulting stress gradient can even cause a transition into the tensile stress regime. However, the reduction mechanism of inclined TDs can stop further tensile stress generation and the stress level remains constant after this stage.

2.4 Defect and stress related phenomena in AlGaN devices

Speck *et. al* have summarised the great impact of TDs on the physical properties of GaN structures [32]. Under commonly used growth conditions TDs initiate the formation of V-defects during the growth of $Al_xGa_{1-x}N$ sublayers, which is very serious for the top barrier layer. Here, these surface pits are not buried by any succeeding layer. In finale HEMT device structures the pits act as electric fields concentrations at the source/drain/gate contact and deteriorate the electrical performance [32].

The efficiency of optoelectronic devices such as LEDs suffers from TD as non-radiative recombination centres. Consequently, these defects cause an instant recombination of holes and electrons without photon emission but heat generation. However, it was found that the tolerable dislocation density for efficient light emission is several orders of magnitude higher for GaN based structures than for conventional III-V systems (e.g. GaAs). First, TD glide is inhibited within hexagonal III-N structure and thus TD motion does not contribute to device malfunction. However, TDs act as pathways for diffusion of dopants (e.g. Mg) which can cause structure degradation [25]. Second, GaN alloys have a rather small carrier diffusion length of 50 nm. Nevertheless, TDs have a great impact on the electrical properties and the lifespan, a further decrease of dislocation density is very desirable [23].

In microelectronic structures TDs can act as current leakage pathways. Consequently, TDs act as conduits for charge breakdown, and the theoretically possible breakdown strength cannot be obtained. Experimental works have shown that dislocations cause carrier scattering and recombination [33]. The piezoelectric properties of the GaN crystals give rise to local electric fields caused by dislocation strain fields. Due to Coulomb interaction passing carriers get scattered at TDs. Furthermore, theoretical calculations have indicated that edge dislocations give rise to deep levels within the forbidden energy gap, which act as traps for carriers. Hence, the mobility and the carrier concentrations are decreased within areas with a high dislocation density and the efficiency suffers from the presence of the dislocations [34].

Since TDs are formed to relax elastic strain, their evolution across the heterostructure is closely related to the presence of sublayer stresses. As a consequence, the control of

residual stress across a heterostructure is crucial for (i) the reduction of TD density, (ii) the control of overall wafer bow and (iii) the devices reliability. However, the formation of stress gradients within HEMT structures is still not fully understood and stress gradient are still the main source for TDs formation and cracking [26].

Industrial applications require the use of large diameter Si wafers, which are even more sensitive to the negative effects of residual stress gradients. Due to the large wafer size already minor overall stress values induce a significant wafer bow. As previously described the deposition temperature is adjusted by bottom wafer heating. Due to the presence of wafer bow, large scale wafers do not lie completely flat on the susceptor surface and thus cannot be heated homogenously. As a result, there is a variation in deposition temperature across the wafer diameter and subsequently the growth of homogeneous films becomes very challenging. These non-uniformities limit the production yield in GaN processes.

Furthermore, the presence of tensile stress concentrations has a negative impact on the device reliability. Especially cracking of thick sublayers with compressive to tensile stress transition, limits the reliability of GaN based structures [35].

With regards to the electrical properties, the piezoelectric behaviour of GaN causes very local electric fields in regions with high lattice strain [36]. An uncontrolled stress state within the 2DEG area results in band structure modifications and deteriorates the concentration and mobility of carriers. It is therefore crucial to control the microstructural strain gradient in order to enhance the performance and lifespan of electrical devices. The development of depth resolved stress analyses is of great interest for semiconductor industry in relation with the development and design of high quality GaN structures.

3

Methods for stress and defect analyses of HEMT structures

Due to the importance of stress control within semiconductor devices various methods to determine the residual stress gradient as a function of the film thickness have been developed. In general, it can be distinguished between techniques, which are based on (i) focused ion beam milling combined with digital image correlation (FIB-DIC) (ii) transmission electron microscopy (TEM), (iii) X-Ray diffraction, (iv) wafer curvature monitoring and (v) Raman spectroscopy. Within the scope of this thesis various experimental methods have been performed and the obtained results have been compared. Several advantages and disadvantages for the application of the individual methods in the semiconductor industry have been found.

3.1 Focused Ion Beam – Digital Image Correlation methods (FIB-DIC)

FIB-DIC analyses are a new class of techniques for the characterization of residual stress gradients within planar surface structures. The FIB-DIC approach is based on incremental FIB milling in combination with the scanning electron microscopy (SEM) analysis and DIC after each milling step. Depending on the FIB milling geometry, there can be distinguished between several techniques, such as single slot milling, double slot milling, H-bar milling, ring core milling, ion layer removal or hole drilling [37,38] .

In general, FIB milling of stressed structures releases the residual stress within the structure. Hence, the stress state changes and the FIB sample geometry deforms. Changes within the geometry are quantified by SEM imaging with subsequent DIC. Depending on

the used technique, finite element simulations are required to calculate the incremental stress changes from the detected deformations, the elastic material constants and the sample dimensions. Thus, the incremental removal of a surface structure can reveal the residual stress gradient across the FIB milled area [39].

As presented in *section A* and *C*, the stress gradient of the heterostructure illustrated in Figure 4a have been analysed using the Ion Beam Layer Removal method (ILR-method). This approach was introduced by Massl *et. al.* in 2007 [40]. Figure 6 shows a three-dimensional illustration, of a microcantilever, which was the basis of the ILR study discussed in this thesis. The cantilever was fabricated by FIB milling and consisted of the heteroepitaxial film and the Si substrate. For the presented study, there have been used a cantilever dimension of 110.9×5.9×3.4 μm^3 in the x, y and z direction, respectively (see coordinate system in Figure 6). Subsequently the ILR beam was divided in section A and section B.

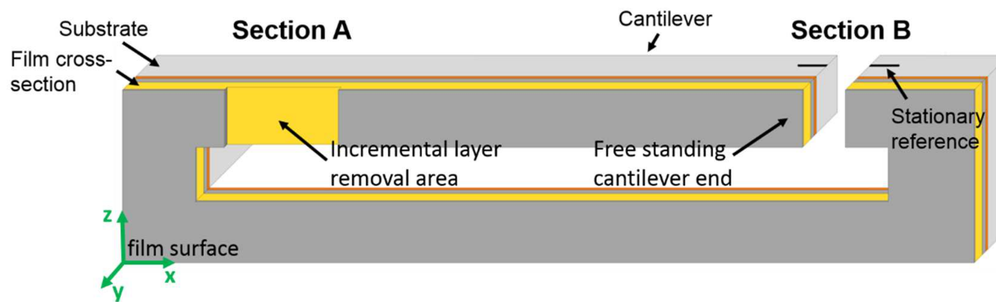

Figure 6: A three dimensional schematic of an ILR microcantilever, which consists of the heterostructure and the substrate.

After cutting the cantilever into its final form, the cantilever initially bends in y direction owing to the global residual stress within the film. Deflections of the free end (δ) to positive and negative y directions can be associated with in-plane tensile and compressive stress, respectively. Subsequently the film is incrementally removed in section A, where the depth resolution of the obtained stress profile is mainly determined by the size of single FIB milling steps. The investigation discussed in this thesis has been carried out with a FIB milling step size of 100 nm. In order to prevent ion beam damage, the cantilever polishing

as well as the gradual layer removal were carried out with a relatively low ion current of 50 pA and at high voltages of 30 kV. Figure 7 shows SEM cross-section images (normal to the x-y-plane) of sections A and B at various FIB milling steps *i*, where i = 0 is the initial state. Due to the stepwise removal of the film, the residual stress of the removed material volume reliefs and the deflection of the free cantilever end changes.

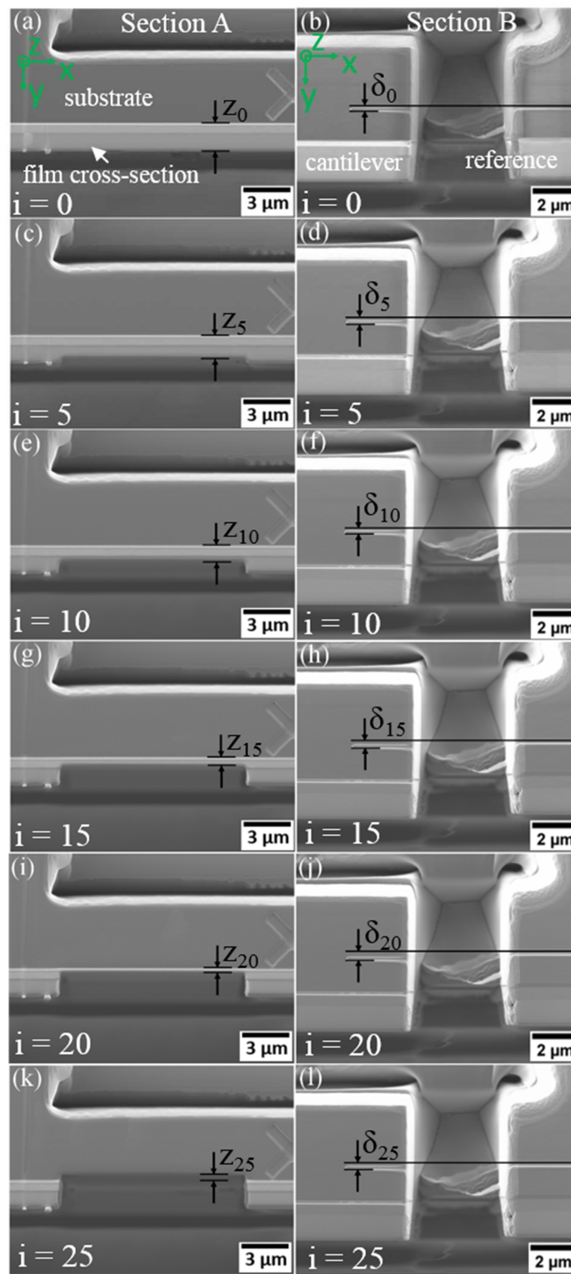

Figure 7: SEM cross-section images of sections A and B after FIB milling step *i*. The deflections (δ_i) and the associated layer thickness (z_i) were determined via DIC.

The deflection change ($\Delta\delta = \delta_i - \delta_{i+1}$) was determined using DIC, which quantifies the relative shift between the cantilever and the stationary reference mark in section B. The associated remaining layer thickness (z_i) was also determined by DIC of the cross-section images from section A. In Figure 8, the cantilever deflection is plotted as a function of the associated film thickness. On the basis of this dependence, the heterostructure stress gradient was calculated by finite element simulation, as shown in Figure 8. For more details about data evaluation, see reference [40]. The used elastic properties are documented in the article of *section A*.

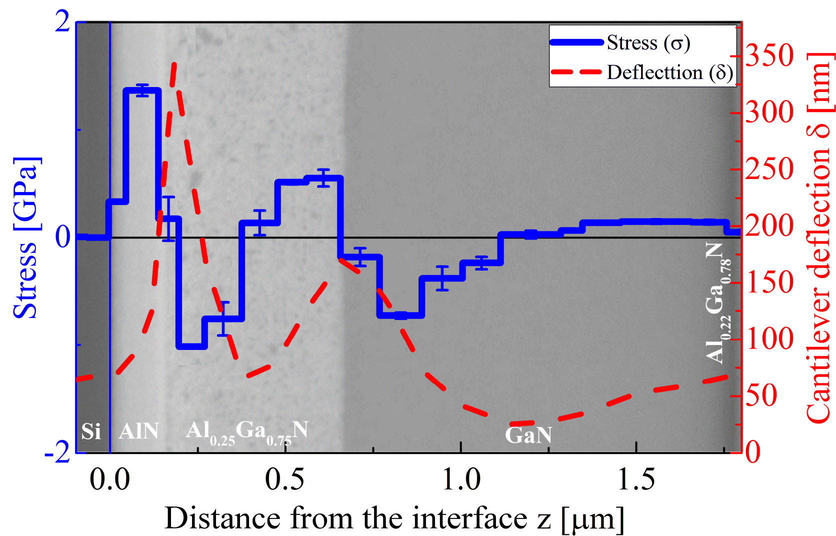

Figure 8: The cantilever deflection (δ) as well as the simulated stress gradient are plotted as a function of the distance to the interface (z). In the background, a SEM image shows the cross-section of the heterostructure depicted in Figure 4a.

As a next step, the residual stress profile of the more complex superlattice structure depicted in Figure 4c was characterized. In this study the ILR analysis was carried out with milling step sizes of 30 nm. The acquired stress profile is shown in Figure 9. Owing to the spatial resolution of 30 nm, sublayer stress gradients are revealed within the 160 nm and 190 nm thin AlN and $Al_xGa_{1-x}N$ layers. The stress increase of the final data point indicates tensile stress within the 25 nm thin $Al_xGa_{1-x}N$ barrier layer.

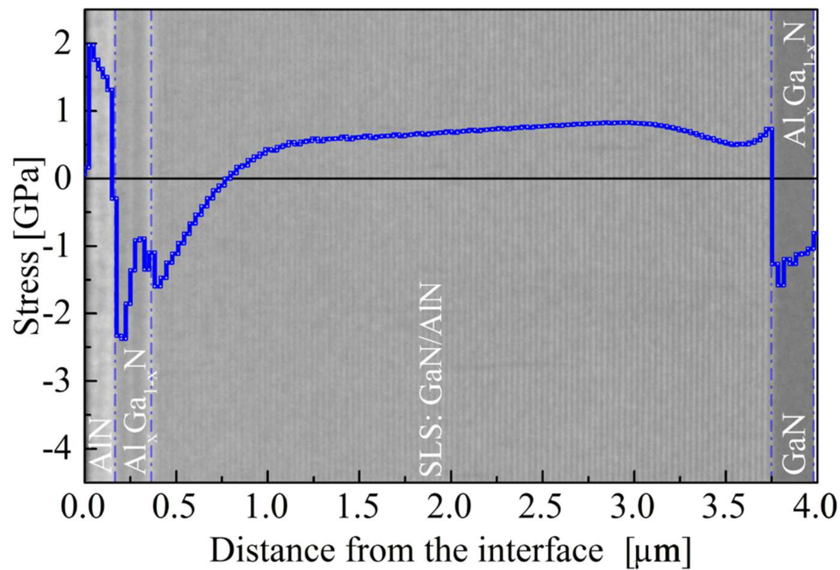

Figure 9: The stress profile of the heterostructure depicted in Figure 4c is plotted with a resolution of 30 nm. In the background, a SEM image shows the cross-section of the heterostructure depicted in Figure 4c.

One major advantage of the FIB-DIC based approach is that the method can be applied independent of the film's crystal structure, i.e. also amorphous materials can be investigated. Schöngrundner *et. al.* have studied the limits and the reliability of ILR-analysis [37], reaching the conclusion that an appropriate cantilever design can prevent significant errors due to FIB damage, cracking and stress redistribution during film removal [39–41]. A guideline for the choice of correct cantilever dimensions can be found in the literature [41]. However there still remain minor influences from cantilever fixation and fabrication, which relieve film stress at the initial state. In addition, the resolution limits of the SEM imaging and FIB milling precision have to be taken into account. Nevertheless, latest publications show, that ILR-analysis can reveal surface stress gradients with spatial resolutions down to 10 nm [42].

3.2 Transmission Electron Microscopy (TEM)

In TEM electrons are focused by electromagnetic lenses and transmitted through thin samples. While the electrons pass the sample volume, they interact both, elastically an inelastically with atoms. These interactions give rise to different signals, such as transmitted electrons, elastically scattered electrons, inelastically scattered electrons and X-rays/visible light emission. Depending on the type of signal which is detected, TEM can provide microstructural images, electron diffraction patterns and analytical spectra. Due to the small wavelength of electrons, TEMs can achieve sub-Angstrom resolution. Owing to its versatility and high resolution TEM has become a very important tool and multitude of operational techniques has been developed. In order to learn more about TEM, this thesis addresses the textbook “Transmission Electron Microscopy” from Williams and Carter. This book is a comprehensive review of transmission electron microscopy, which gives more information about the physical principles and the basic operation modes [43].

In the framework of this thesis, TEM has been used in diffraction and imaging mode, to characterise the microstructure and the strain gradient of HEMT heterostructures. This involved the following measurements: (i) high resolution transmission electron microscopy (HRTEM); (ii) precession electron diffraction (PED); (iii) scanning transmission electron microscopy (STEM).

3.2.1 High Resolution Transmission Electron Microscopy (HRTEM)

HRTEM is an imaging based technique, operating at magnifications larger than 400000 times to image the atomic structure of crystalline materials. To acquire quantitative lattice information, some basic requirements have to be fulfilled. First, quantitative HRTEM imaging is very sensitive to sample thickness and thus the region of interest has to be very thin (< 50 nm). Otherwise multiple electron scattering (> 1 scattering events) occurs and basic considerations are not valid. Second, despite the small electron wavelength, which provides a superior theoretical resolution limit, the actual resolution is limited by imperfections in electromagnetic lenses. These imperfections cause astigmatism as well as spherical and chromatic aberrations, which have been a major issue in HRTEM. Most state-of-the-art transmission electron microscopes however, are equipped with aberration

correctors. Due to their superior resolution, these microscopes are favourable for quantitative HRTEM imaging (for more details see [43]).

In order to acquire information about the lattice spacing as well as the atomic structure of various HEMT structures (Figure 4) HRTEM measurements were performed on a JEOL 2100 F, which is equipped with a spherical aberration corrector. The HRTEM image in Figure 10 shows the atomic structure of the GaN sublayer from the multilayer stack depicted in Figure 4a. The sample was observed along the $[1000]$ axis. The individual atom columns were resolved and subsequently indexed by comparing the experimental image with the simulated crystal model, as shown in Figure 10c. Hence, lattice spacings of d_{0001} = 5.19 Å and $d_{1\bar{1}00}$ = 2.76 Å were determined by measuring and averaging the atom column position of several intensity plots (Figure 10d-e). Next, the in-plane and out-of-plane lattice constant (*a, c*) were calculated using following equations [43]:

$$\frac{1}{d_{0001}} = \frac{1}{c} \qquad \frac{1}{d_{\bar{1}100}} = \frac{2}{\sqrt{3}a} \qquad (3), (4)$$

Subsequently, the in-plane and out-of-plane lattice strains (ε_{xx}, ε_{zz}) were evaluated by using unstrained reference values, which were taken from the literature (a_{GaN} = 3.186 Å, c_{GaN} = 5.186 Å) [44]:

$$\varepsilon_{xx} = \frac{a_{exp} - a_{GaN}}{a_{GaN}} \qquad \varepsilon_{zz} = \frac{c_{exp} - c_{GaN}}{c_{GaN}} \qquad (5), (6)$$

With this approach strain values of $\varepsilon_{xx} = 3 \cdot 10^{-4}$ and $\varepsilon_{zz} = 7 \cdot 10^{-4}$ were revealed within the investigated region of interest. Since the strain resolution limit is in the range of $1 \cdot 10^{-3}$ the investigated GaN structure can be assumed as strain-free [45]. However, such a "real-space" analysis is very time consuming and sensitive to crystal defects such as dislocations or stacking faults.

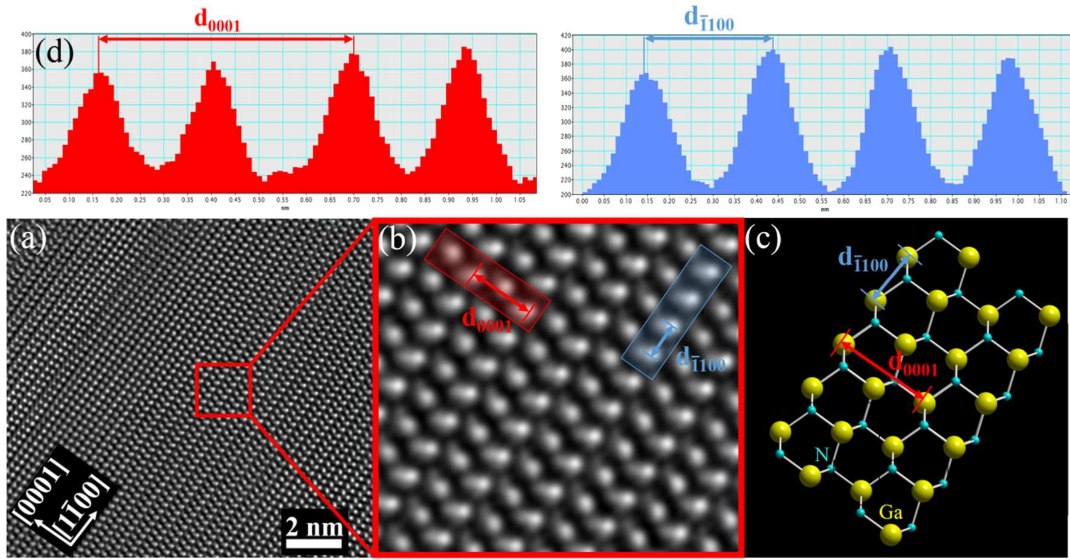

Figure 10: (a) HRTEM image of the GaN sublayer within a HEMT structure. (b) An enlarged view displays the distance of the GaN atom columns. (c) Simulated GaN crystal structure to correlate the atom column positions with the lattice spacings d_{0001} and $d_{1\bar{1}00}$. Vertical and the horizontal intensity plots were used to determine the lattice strain (d-e).

To cope with these issues, Hytch *et. al.* have introduced a "reciprocal space" approach, namely “*Geometrical Phase Analysis*” (GPA), where strain maps are extracted from HRTEM images [46]. This method performs a Fast Fourier Transformation (FFT) on the HRTEM image, to acquire virtual Diffraction Patterns (DP), which displays the recorded image within the reciprocal space (details about DP are addressed in the *PED section*). The obtained DP is filtered by applying a mask, which is associated to the present sets of lattice planes. Subsequently a new image is formed on the basis of the filtered DP. In a final step, a strain map can be deduced employing an algorithm, which measures the relative lattice plane shift, with respect to a selected reference area [47].

The results of such a GPA approach can be seen in Figure 11, where the top GaN/$Al_{0.22}Ga_{0.78}N$ interface of the structure depicted in Figure 4a was investigated. The in-plane and out-of-plane strain maps (Figure 11b-c) were acquired from the HRTEM image in Figure 11a. Since the ε_{xx}-map appears homogeneous, the in-plane lattice constant

does not vary across the interface owing to the pseudomorphic growth of the $Al_{0.22}Ga_{0.78}N$ barrier on the GaN buffer. However, within the ε_{zz}-map, both layers can be clearly distinguished. According to Vergard's law the *c*-lattice parameter is about 0.67% smaller for $Al_{0.22}Ga_{0.78}N$ than for GaN crystals. This correlates well with the ε_{zz}-map, which exhibits an average difference of 0.72%.

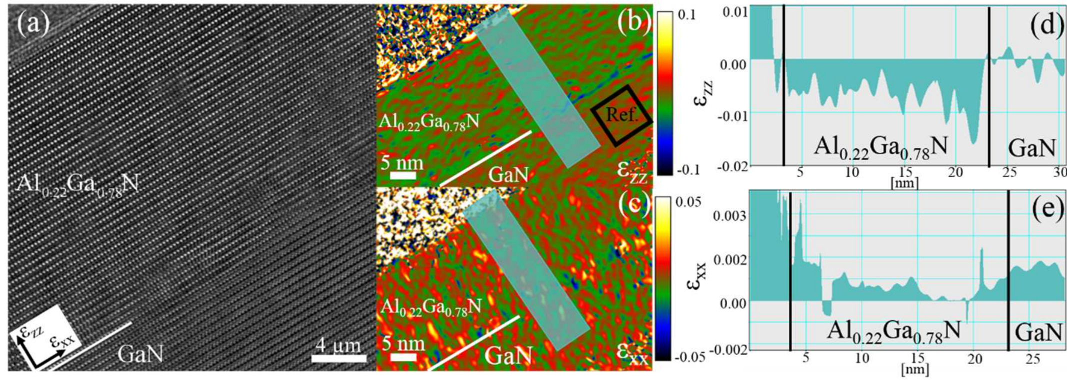

Figure 11: GPA analysis of a HRTEM image of the $Al_{0.22}Ga_{0.78}N$/GaN interface (a). The out-of-plane (b) and in-plane (c) strain maps have been determined with respect to the reference area as indicated in (b). The ε_{xx}- and ε_{zz} charts display the strain evolution across the $Al_{0.22}Ga_{0.78}N$/GaN interface (d-e).

As demonstrated, HRTEM is a remarkably powerful technique for the characterization of highly local strain concentrations, with a precision of about $1 \cdot 10^{-3}$ [45].Since GaN has a Young's Modulus of about 286 GPa [48], the stress resolution limit of HRTEM analyses is in the range of 286 MPa. Moreover, due to the limited field of view (maximum $100 \times 100\ nm^2$), HRTEM is not suitable for analysis of strain profiles across thick heterostructures.

As reported in the article of *section B*, additional HRTEM studies were performed to investigate the atomic structure at sublayer interfaces. Figure 12 shows a HRTEM image of the Si/AlN interface of the multilayer stack, illustrated in Figure 4a. The image exhibits a 2 nm thick SiN_x interlayer, which originates from the AlN nucleation step, during which the Si substrate was exposed to N before supplying Al. Despite the interlayer, the AlN

sublayer grew with an epitaxial relationship of $[01\bar{1}0]$ AlN parallel to $[11\bar{2}]$ Si as well as $[0001]$ AlN parallel to $[111]$ Si, as indicated in Figure 12. The epitaxial relation can be seen in both, the HRTEM image, as well as the virtual DP obtained by FFT of the AlN the Si layer (insets Figure 12).

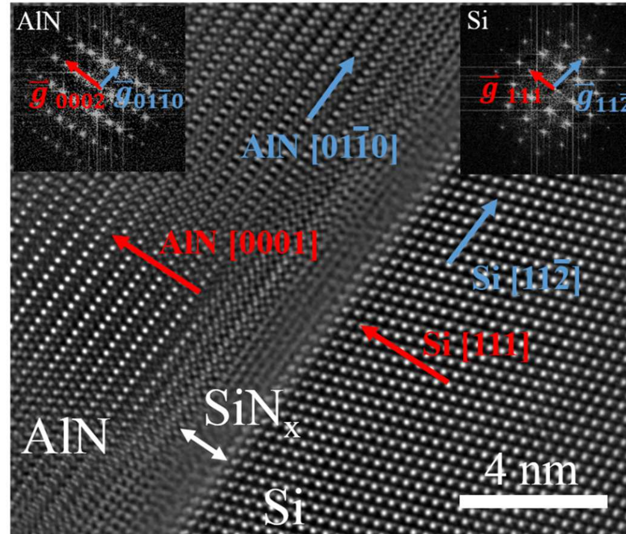

Figure 12: HRTEM image of the Si/AlN interface of the HEMT structure illustrated in Figure 4a. The sublayer DPs (insets) reveal the epitaxial relationship between both sublayers.

3.2.2 ***Precession Electron Diffraction (PED)***

PED is a rather new technique, which is used to determine the lattice strain and crystal structure based on diffraction pattern (DP) evaluation. Diffraction occurs at the crystal lattice due to the wave nature of electrons and the subsequent interference of diffracted electron waves gives rise to the characteristic diffraction patterns. For single crystalline materials DPs appear as spot patterns, where each spot can be associated with a particular set of lattice planes [43].

Figure 13a shows a DP, which was recorded from a GaN crystal by selected area electron diffraction (SAED). Here, the sample was orientated to the $[11\bar{2}0]$ zone axis. In order to acquire DPs from a particular region of interest, a selected area aperture was inserted to confine the illuminated area. The diffraction pattern displays the reciprocal lattice, which

is the Fourier transformation of the real lattice. Hence the reciprocal lattice vector ($\vec{g}$) as well as the reciprocal lattice spacing (d^*_{hkl}) share the same direction and are the inverse of their real space equivalents ($\vec{r}$, d_{hkl}):

$$d_{hkl} = {}^{1}/_{d^*_{hkl}} \tag{4}$$

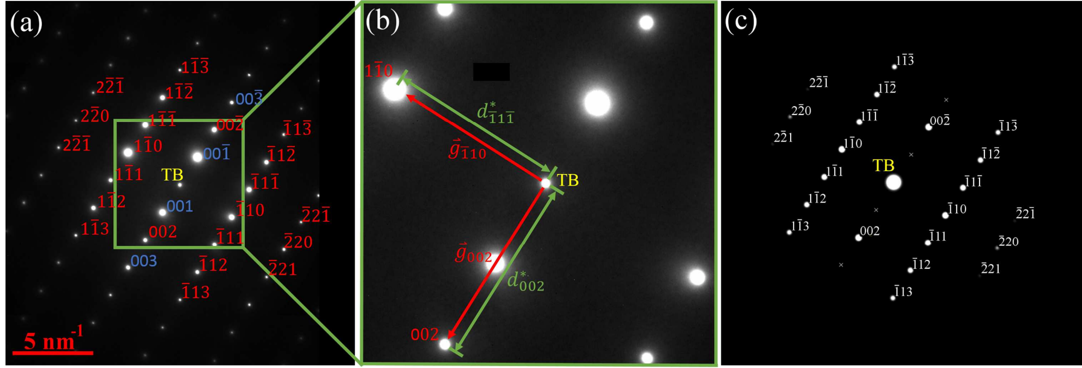

Figure 13: Experimental (a) and simulated (c) GaN diffraction pattern viewed along the $[11\bar{2}0]$ zone axis. Transmitted beam (TB), different diffraction spots, the reciprocal lattice vectors ($\vec{g}_{hkl}$) as well as the reciprocal lattice spacings (d^*_{hkl}) are labelled. Blue labels are associated with forbidden reflections.

By considering only single scattering events (kinematical conditions), the diffraction intensity varies for particular lattice planes. Hence, the spot intensities within DPs depends on the crystal structure, which can be described mathematically by the so-called structure factor. The simulated DP in Figure 13c demonstrates, that certain spots, which are kinematically forbidden (e.g. 001) are missing within GaN DPs. Since electrons have strong interactions with matter, it is highly likely that multiple scattering events occur within thick samples. As a consequence, the spot intensities of DPs are affected by dynamical effects and even forbidden diffraction spots, such as 001, appear (see Figure 13a). Hence, kinematical approaches are not valid and a more complex dynamical approximation has to be applied. Moreover common diffraction techniques, such as SAED, are not suitable for depth resolved strain measurements across multilayer structures [43].

However, there exist two diffraction modes, namely nanobeam electron diffraction (NBED) and PED, which are dedicated for strain measurement with high spatial resolution. Since PED is less sensitive to sample bending/misorientation and dynamical scattering, this thesis has focused on PED analysis [49]. In this approach, the electron beam is tilted with respect to the zone axis and precessed around the axis (without changing the tilt angle), as illustrated in Figure 14a. In order to obtain stationary DPs, the electron beam rocking above the sample is compensated by beam de-rocking below the sample plane. The resulting diffraction pattern is the superposition of individual partial DPs, which were taken from various tilt directions while precessing the electron beam. Due to the tilted electron beam, only few reflections fulfil Bragg's condition within one single partial DP. Hence, dynamical effects are supressed even in thick samples and resulting in a quasi-kinematic diffraction pattern (see Figure 14b). Consequently, the spot intensity is proportional to the structure factor which enables phase determination. Furthermore high order reflections are visible, which improves the measurement precision [50].

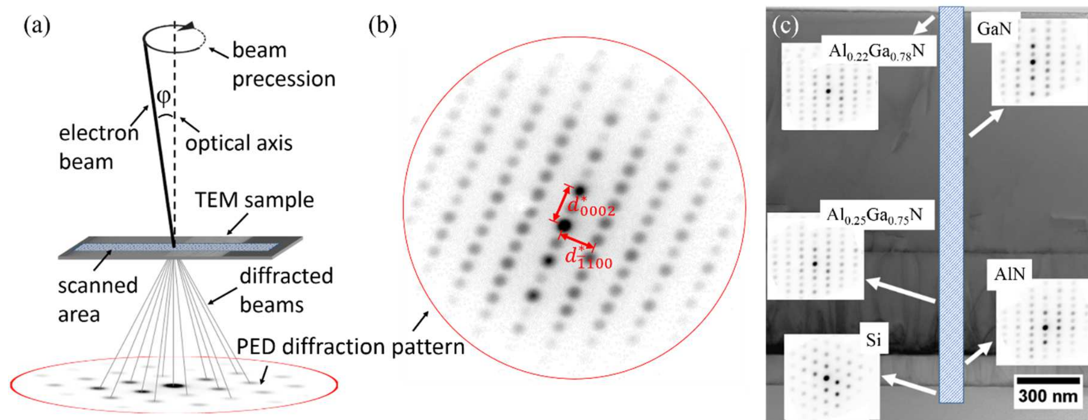

Figure 14: (a) Schematic of the precession electron diffraction measurement. (b) The diffraction pattern from GaN layer was recorded by PED, which was orientated along the $[11\bar{2}0]$ zone axis. Although not all forbidden reflections decay completely, the spot intensities are associated with the structure factor. (c) DPs of the individual sublayers were obtained by scanning the beam across the highlighted area.

The PED analysis was carried out on a Zeiss Libra 2000 FE TEM microscope, equipped with a NanoMegas DigiStar precession tool. Figure 14c shows a STEM image of the investigated heterostructure (Figure 4a). As highlighted, the electron beam was used to scan across the heterostructure to obtain DPs with a step size of 2 nm. Additionally, DPs were acquired from a freestanding lamella, which was used as unstrained reference [29].

The *a* and *c* lattice parameter variations across the heterostructure depth were determined, by analysing the spot positions of the individual DPs. Figure 15 displays the c_{exp}/a_{exp} ratio across the investigated heterostructure area. For reference purposes, strain-free c_0/a_0 values from literature are indicated in each sublayer. Tensile and compressive stresses cause lattice distortions, which shift the c_{exp}/a_{exp} ratios to lower and higher values, respectively. Hence, significant strain gradients were reveal within the individual sublayers. Depending on the used PED setup, a stain precision of $1\cdot10^{-4}$ can be achieved, which is an improvement of one order of magnitude in comparison with HRTEM measurements [49].

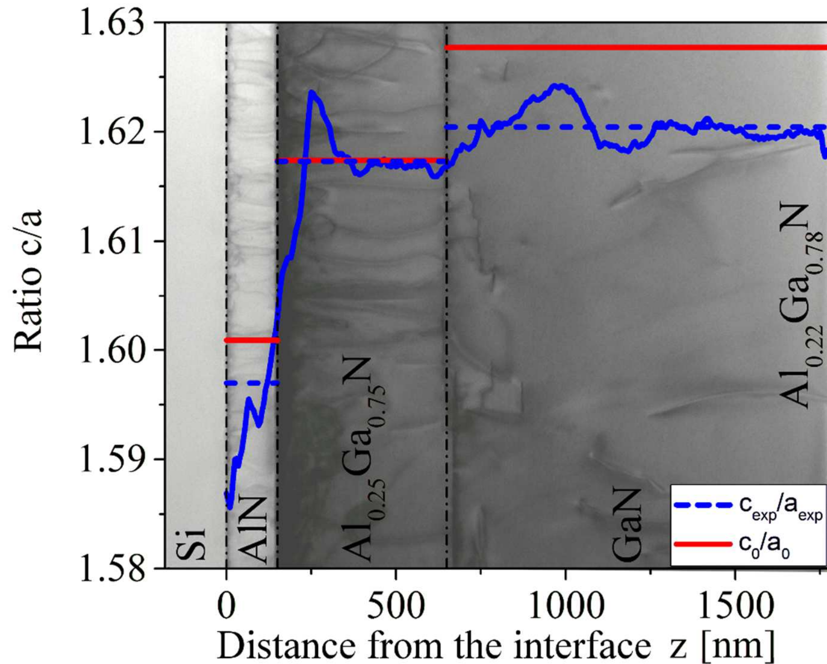

Figure 15: The *c*/*a* ratio evolution is plotted against the distance from the substrate for the heterostructure illustrated in Figure 4a.

3.2.3 Scanning Transmission Electron Microscopy (STEM)

STEM analyses were carried out in order to investigate the microstructure of different HEMT stacks. In this operation mode, the electron beam is focused into a spot and a sample is scanned across a certain region of interest. The signal is then collected by two different detectors, which are selective to electrons from different scattering angles. Hence, there can be distinguished between bright field (BF) and high angle annular dark field (HAADF) images, which cover low and large scattering angles, respectively. Depending on the settings (camera length), STEM images provide diffraction and/or Z-contrast. For dislocation imaging, the sample has to be tilted into "two-beam" conditions, where only two spots appear strong within the DP. Those spots correspond to the transmitted beam and to one particular set of lattice planes. All other lattice planes do not fulfil Bragg's condition and provide just faint diffraction. There exist various two-beam conditions, where planes with a particular reciprocal lattice vector $\vec{g}$ fulfil Bragg's condition [43].

However, strain fields around dislocations cause highly local lattice distortions, which modify the diffraction condition. As a result, the surrounded area is out of two-beam condition, giving rise to a detectable diffraction contrast. Consequently, dislocations appear as dark/bright lines in BF/HAADF images [43].

According to the following invisibility criterion, there exist certain conditions where dislocations with a particular Burgers vector $\vec{b}$ cannot be detected [51]:

$$\vec{g} \cdot \vec{b} = 0 \tag{7}$$

Here, $\vec{g}$ is the reciprocal lattice vector of strong diffracting planes (for details see *PED section*). In order to also display invisible dislocations, the sample has to be tilted to different two beam conditions.

As previously mentioned, there exist only three different kinds of threading dislocations in $Al_xGa_{1-x}N$ crystals (see *section 2.3*). Due to the invisibility criterion, the setting of proper two-beam conditions can either conceal screw (e.g. $\vec{g}$ = $[11\bar{2}0]$) or edge (e.g. $\vec{g}$ = $[0002]$) dislocation. This is a valuable tool, for quantitative dislocation analysis.

Figure 16 shows two STEM images of the heterostructure illustrated in Figure 4a. Both images depict the same sample position, however the sample was tilted to different two beam conditions: (a) $\vec{g} = [0002]$ where pure edge dislocations are invisible and (b) $\vec{g} = [\bar{1}101]$ where all dislocations are visible. Both images show, that the dislocation density decreases within each successive sublayer. Furthermore, the comparison of both images proves, that the edge dislocation density is significantly higher than the screw dislocation density.

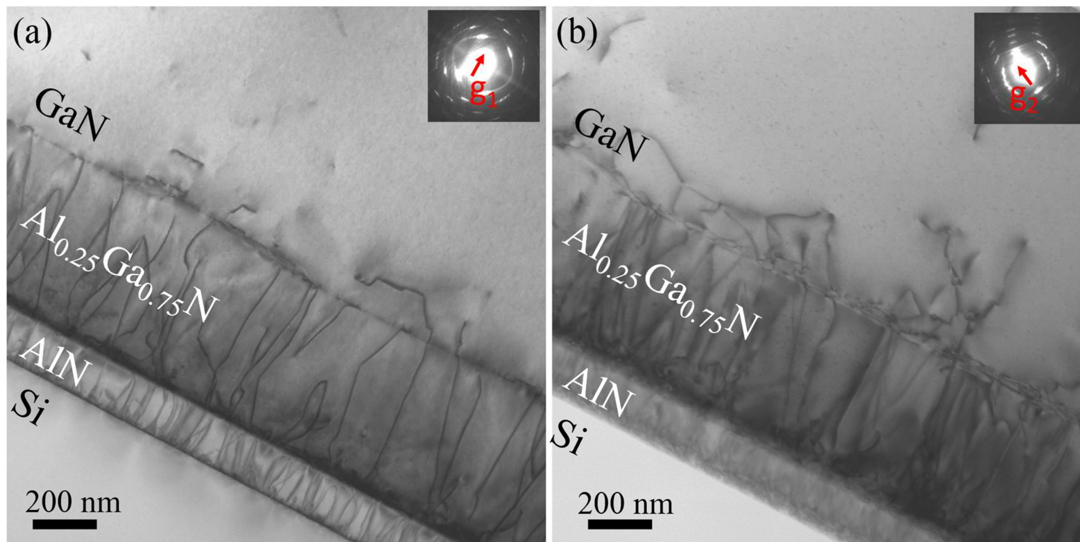

Figure 16: Both STEM images were recorded at the same sample positon. Different diffraction conditions (as indicated in the inset) were used, to visualise different kinds of dislocations.

Figure 17 shows three STEM images of the three samples depicted in Figure 4a-c. For all three structures, the dislocation density across the multilayer decreases after sublayer interfaces. A qualitative comparison of the three different samples shows, that SLS based transition layers (Figure 17c) cause a more rapid dislocation density decrease than the single $Al_xGa_{1-x}N$ layer (Figure 17a) and the stair case $Al_xGa_{1-x}N$ layer (Figure 17b) concept.

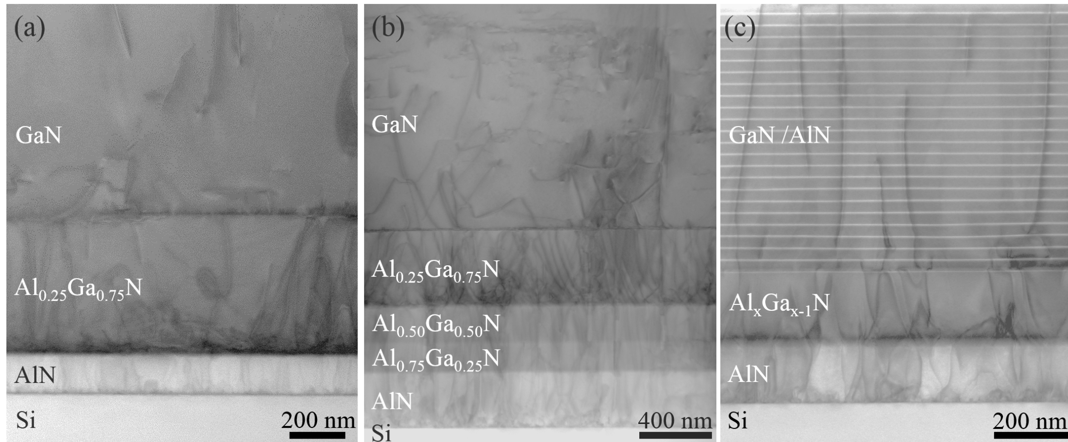

Figure 17: A STEM based comparison of the three samples depicted in Figure 4a-c.

3.3 X-ray Diffraction (XRD)

XRD is a well-established characterization method for structural analysis in the semiconductor industry. XRD is based on the interference of monochromatic X-rays after diffraction on a crystalline sample. In order to observe diffraction peaks corresponding to reflections from different crystallographic planes, the incident (ω) and diffraction (2θ) angles are varied by the rotation of the sample and/or the detector as well as the X-ray tube. The associated lattice spacings can be determined by Bragg's law. Hence, XRD measurements can be applied for the analyses of (i) the crystalline phase, (ii) the crystallite orientation distribution (texture), (iii) the material composition (iv) the size of coherently diffracting domains and (v) the average lattice strain, with a sensitivity of $1 \cdot 10^{-5}$ [52], [53]. Moram and Vickers have published a comprehensive article, which provides fundamental knowledge about X-ray diffraction on III-N semiconductors [54].

For the XRD investigations presented in this thesis mainly reciprocal space mapping (RSM) has been used for the characterization of sublayer strain states and the dislocation density variation across the heterostructure, depicted in Figure 4a. All XRD measurements were carried out on a Rigaku SmartLab 5 circle diffractometer in high resolution setup [55].

RSM is a high resolution X-ray diffraction technique, where the lattice strain and crystal quality can be determined based on two dimensional reciprocal space maps. These intensity

contour maps display the reciprocal lattice in the vicinity of a particular reciprocal lattice point (RLP). Figure 18 illustrates the relation between the real crystal lattice, the reciprocal space as well as the angles *ω* and *2θ* for a [0001] orientated GaN film. The scattering vector *q* is determined by the incident beam vector (k_0) and the diffracted beam vector (k_h), using $q = k_h - k_0$. By setting appropriate angles with respect to the crystal, the scattering vector can be directed to a particular RLP and diffraction occurs. In RSM the q vector is probed trough the reciprocal space by carrying out a series of *2θ-ω* line scans at successive *ω* values. The scanned angles (*2θ-ω*, *ω*) were converted into the *q* vector components (q_x and q_z) by following relationship [54]:

$$q_x = \frac{1}{\lambda}\{\cos\omega - \cos(2\theta - \omega)\} \tag{8}$$

$$q_z = \frac{1}{\lambda}\{\sin\omega + \sin(2\theta - \omega)\} \tag{9}$$

with λ as the X-ray wavelength. Consequently, the acquired map is orientated with respect to the real lattice, where q_x and q_z are parallel to in-plane and out-of-plane lattice directions. The reciprocal space maps were plotted in reciprocal lattice units (g_x and g_z) which have been obtained from the crystallographic units q_x and q_z by following equation [54]:

$$g_x = \frac{q_x}{2\pi} \tag{10}$$

$$g_z = \frac{q_z}{2\pi} \tag{11}$$

RSMs can be operated in various diffraction geometries, namely (i) symmetrical, (ii) asymmetrical, (iii) grazing incident – in plane scattering, as well as (iv) skew symmetric geometries [54], from which (i) – (iii) were used for the presented study [54] (see Figure 18).

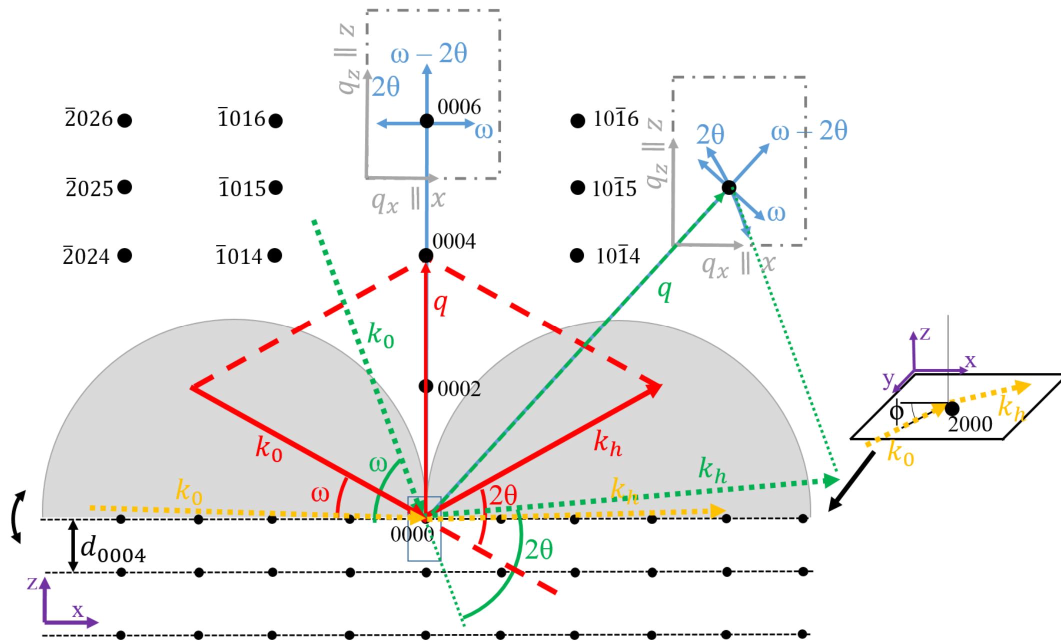

Figure 18: A schematic of the reciprocal space for a [0001] orientated GaN film. The incident beam vector (k_0) as well as the diffracted beam vector (k_h) are shown for symmetrical scans ($\omega = \theta$; red), asymmetrical ($\omega \neq \theta$; green) as well as gracing incident – in-plane scattering ($\omega < 1°$; $\theta < 1°$; yellow).

(i) In symmetrical scans, the angle between the sample surface and the incident beam vector (ω) is equal to the diffraction angle (θ). Hence, the scattering vector (q) is normal to the surface plane and only planes parallel to the surface can be probed. In the study presented in this thesis, the 0002, 0004 as well as 0006 sublayer reflections have been recorded by symmetrical RSM [28].

(ii) In Figure 18 the green lines illustrate the incident and diffracted beam vector of an asymmetrical scan ($\omega \neq \theta$). Consequently, the scattering vector is not confined to a particular direction and can be probed through the reciprocal space. Within the asymmetric mode the $10\bar{1}5$ and $11\bar{2}4$ reflections were collected. These reflections contain information on both, a and c lattice constant. However, the reciprocal space close to the surface is not accessible by asymmetric scans as either the incident or the diffracted beam is blocked by the sample. In Figure 18 these regions are highlighted in grey [56].

(iii) In order to record RLPs within the areas coloured in grey, grazing incident –in-plane scattering measurements were conducted (see Figure 18). Here very shallow incident and diffraction angles were used in order to reach in-plane reflections. Subsequently, the two-dimensional map was acquired by scanning the in-plane angle ϕ rather than ω, as illustrated in Figure 18. With this approach it was possible to record 1000 , 2000 and 3000 reflections of $[0001]$ oriented $Al_xGa_{1-x}N$ films.

However, crystal imperfections result in peak broadening and RLPs do not appear as sharp diffraction spots within the reciprocal space maps. The broadening is mainly a consequence of sample curvature, microstructural defects, limited diffraction domain size as well as instrumental broadening. Furthermore, strain causes lattice distortions, which moves the RLP position within the reciprocal space. For further details see references [53,54].

As reported in the article of *section B*, the sublayer strain as well as defect density were studied on basis of RLP positions and widths. Figure 19a-b plot the reciprocal space maps of the 0006 and $10\bar{1}5$ reflections, of the heterostructure shown in Figure 4a. As discussed in *section B* the lattice parameters *a* and *c* of the AlN, $Al_{0.25}Ga_{0.75}N$ and GaN sublayers were calculated on basis of the RLP positions within the measured reciprocal space maps. However within reciprocal space maps of Figure 19a-b the top $Al_{0.22}Ga_{0.78}N$ barrier layer was not resolved.

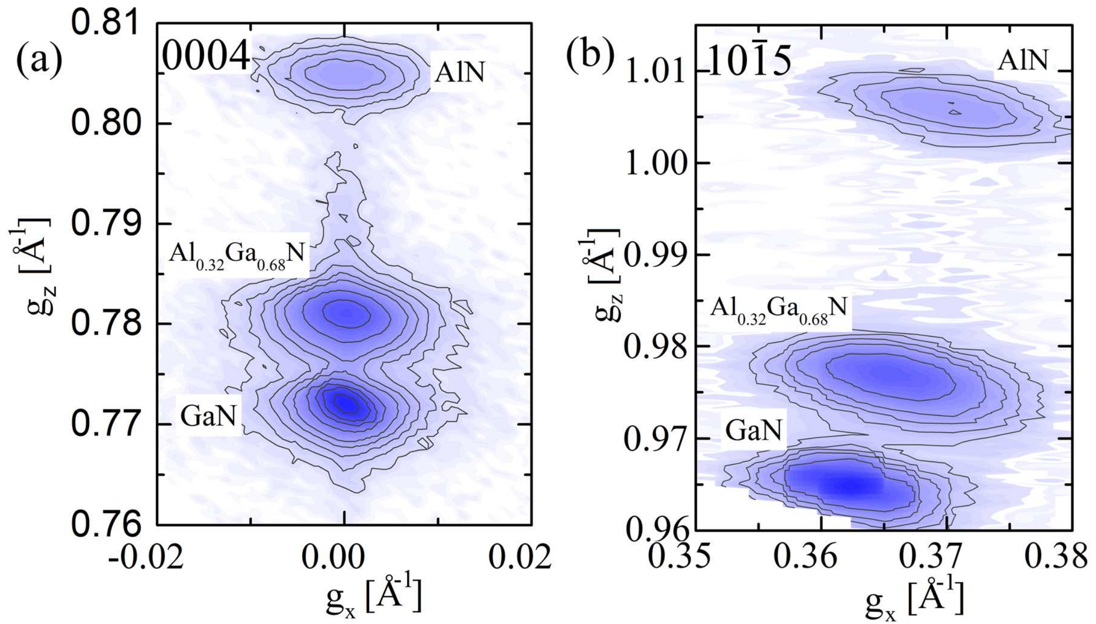

Figure 19: Symmetric (a) and asymmetric (b) reciprocal space maps of the HEMT structure depicted in Figure 4a. The individual AlN, $Al_{0.25}Ga_{0.75}N$ and GaN sublayers can be clearly distinguished.

Subsequently, the average sublayer strain was calculated by using Eq. (5-6), with the experimentally deduced lattice parameter and the strain-free reference values taken from the literature. As a final step, the sublayer lattice strain values were converted into in-plane lattice stress and plotted in Figure 20 by using following equation [28]:

$$\sigma_{xx} = \varepsilon_{xx} \cdot \left[(c_{11} + c_{12}) - 2\,\frac{c_{13}^2}{c_{33}} \right] \tag{12}$$

here c_{11}, c_{12}, c_{13} and c_{33} are the elastic constants of the individual sublayers.

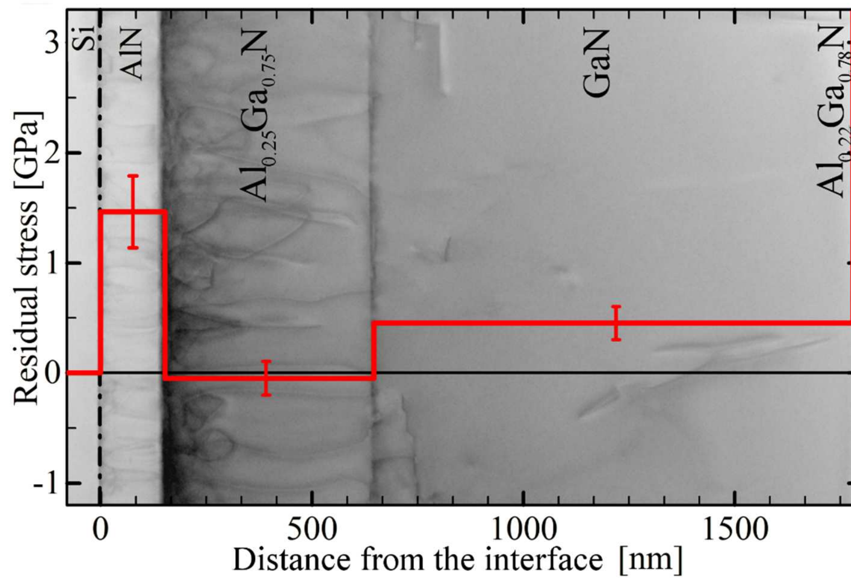

Figure 20 shows the average lattice stress within the AlN, $Al_{0.25}Ga_{0.75}N$, GaN and $Al_{0.22}Ga_{0.78}N$ sublayers. In the background, a STEM image shows the dislocation density variation across the investigated heterostructure.

The STEM image in Figure 20 exhibits rather inhomogeneous dislocation distribution across the heterostructure. In order to quantify the dislocation density within the individual sublayers the RLP broadening was analysed using Williamson-Hall plots (WH-plots). As described in *section B*, WH-plots use higher-order reflections to separate peak broadening caused by dislocations from domain size broadening [57]. In addition, the instrumental broadening was corrected by taking reference measurements on a high-quality Si wafer. Subsequently, several high order in-plane and out-of-plane sublayer reflections were recorded by RSM in gracing incidence – in-plane scattering and symmetrical geometry (see Figure 18). Similar to TEM investigations, in-plane and out-of-plane RLP widths are not affected by screw and edge dislocations, respectively. With this approach it has been found, that the dislocation density decreases with increasing distance from the substrate. Furthermore the results show, that the majority of dislocations have edge type character, which fits well with the previously described TEM analysis [28].

3.4 Wafer Curvature

Wafer curvature is a widely used approach to determine the residual stress of thin films deposited on flat substrates. Due to the low requirements in terms of sample preparation as well as the high accuracy, wafer curvature measurements have been well-established in industrial research for many years [58].

In general, the growth of a stressed film on an unstressed substrate/wafer will lead to sample curvature, as illustrated in Figure 21. The curvature (κ) value is calculated by following equation:

$$\kappa = \frac{1}{R} - \frac{1}{R_0} \tag{13}$$

here R and R_0 are sample curvatures of the deposited wafer and a flat reference, respectively. According to the nomenclature tensile/compressive film stress results in positive (concave)/negative (convex) sample curvature, respectively.

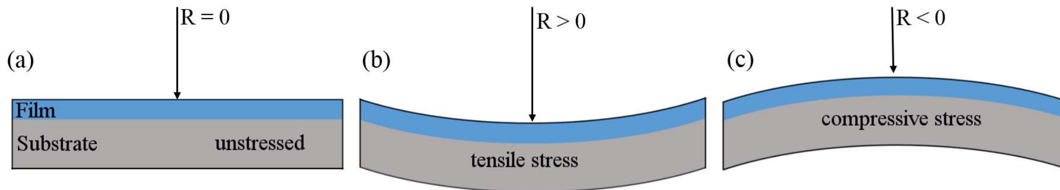

Figure 21: The impact of residual stress within the film on the sample curvature is illustrated. While unstrained films remain flat (a), compressive and tensile film stresses cause concave (negative) (b) and convex (positive) curvatures (c).

The basic relation between the film equi-biaxial stress $\sigma^{(f)}$ and the system curvature κ has been reported for the first time by Stoney in 1909 [59]:

$$\sigma^{(f)} = \frac{M_s \cdot h_s}{6 \cdot h_f} \cdot \kappa \tag{14}$$

Here h_f is the film thickness, M_s is the substrate biaxial modulus and h_s is the substrate thickness. The equation allows the calculation of film stress without the knowledge of any material properties of the film. However, the formula is only valid under the following assumptions: (i) both film and substrate must be homogeneous, isotropic and linear elastic; (ii) the film and the substrate must be the same radius R with $h_f \ll h_s \ll R$; (iii) the film stress state must be in-plane isotropic while shear and out-of-plane stresses are negligible [60].

Various methods have been established to detect the system curvature, such as simple microscopic observation, optical interference based techniques, X-ray diffraction (for single crystalline samples), as well as laser reflection approaches.

For the study presented in this thesis, a laser reflection setup as illustrated in Figure 22, has been used. In this configuration a single laser beam is split into an array of parallel beams. These parallel beams are then reflected from the sample surface and directed to a screen. The distance between the laser spots (*Δd*) is a direct measure for the sample curvature.

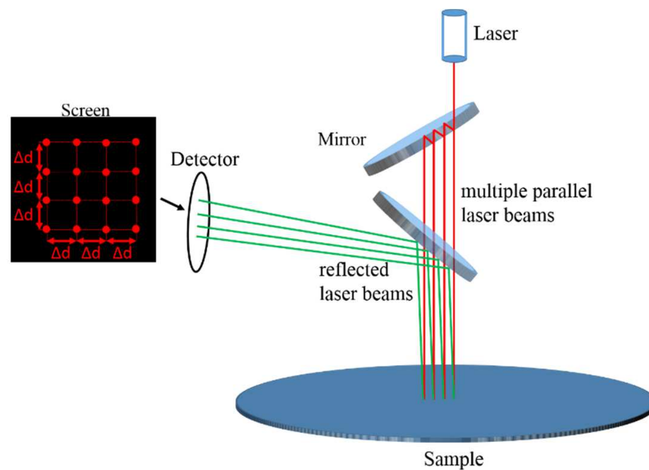

Figure 22: A schematic of a laser based setup for wafer curvature measurements.

In the semiconductor industry, built-in laser measurement units (see Figure 3) are used to monitor the wafer curvature during film growth [3]. Usually such *in-situ* wafer curvature

measurements are solely used for process control. However, Floro *et. al.* have introduced an approach, where the film stress gradient can be deduced from *in-situ* recorded curvature data [61]. For this, they modified the well-established Stoney formula to deduce incremental stress values from the slope of curvature charts. Although several reports about *in-situ* stress measurements have been published in the literature [60,62], there exists no comparative study, which verifies *in-situ* stress profiles with *ex-situ* depth resolved stress measurements.

Recently, there have been submitted an article, which addresses the potential of such comparative analysis (see *section C*). There, the wafer curvature was measured *in-situ* during the growth of the heterostructure, illustrated in Figure 4a. The obtained curvature raw data are plotted in Figure 23. The major process steps, which have been described in *section 2.2* are indicated within in that chart. The time intervals marked in grey correspond to ramping sections, where deposition parameters, such as temperature and precursor pressure were changed, in order to modify the conditions for subsequent sublayer growth.

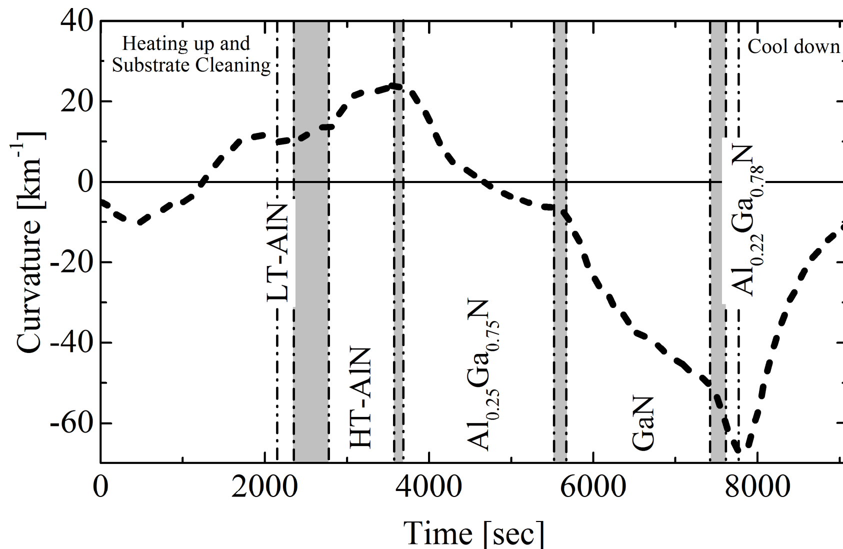

Figure 23: The *in-situ* recorded wafer curvature is plotted as a function of the process time. All significant process stages are indicated.

In order the deduce the stress profile simplifications had to be made: (i) no significant film growth occurs within the grey marked ramping periods; (ii) significant deposition parameter, such as precursor pressure and deposition temperature as well as the deposition rates remain constant during deposition periods; (iii) the differences in elastic properties between the sublayers can be neglected and the heterostructure was treated as a homogeneous film; (iv) very thin sublayers (LT-AlN, $Al_{0.22}Ga_{0.78}N$ barrier layer) which cannot be resolved have no significant impact on the overall stress state and can be neglected. In accordance with these assumptions the curvature is plotted as a function of the heterostructure thickness, as shown in Figure 24.

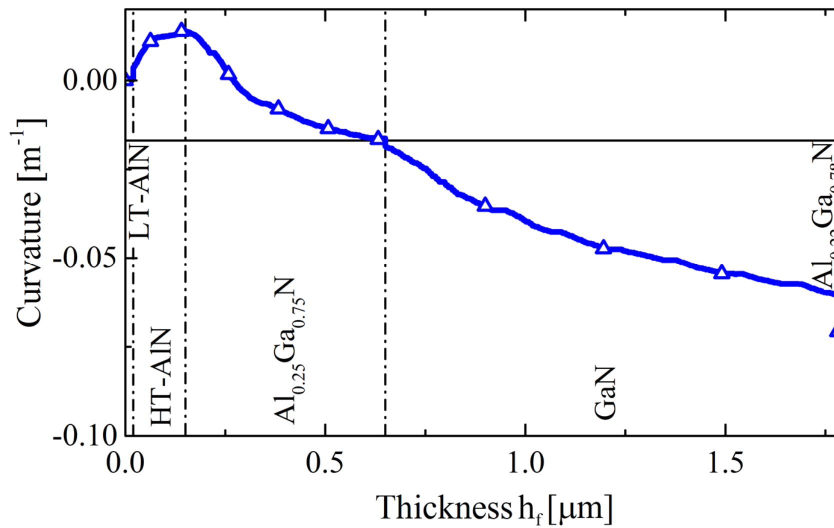

Figure 24: The wafer curvature is plotted as a function of the deposited film thickness.

Next, the average film stress $\sigma_M(h_f)$ was determined as a function of the film thickness (h_f). Subsequently, the product $\sigma_M(h_f) \cdot h_f$ was formed and derived with respect to the film thickness in order to deduce the *in-situ* stress profile. The thermal mismatch between the heterostructure and the Si substrate causes additional tensile stress, which is visible in the curvature change within the cooling stage. Hence a constant thermal stress value was added to the *in-situ* stress profile. Figure 25 shows the stress after cooling as a function of the distance to the substrate.

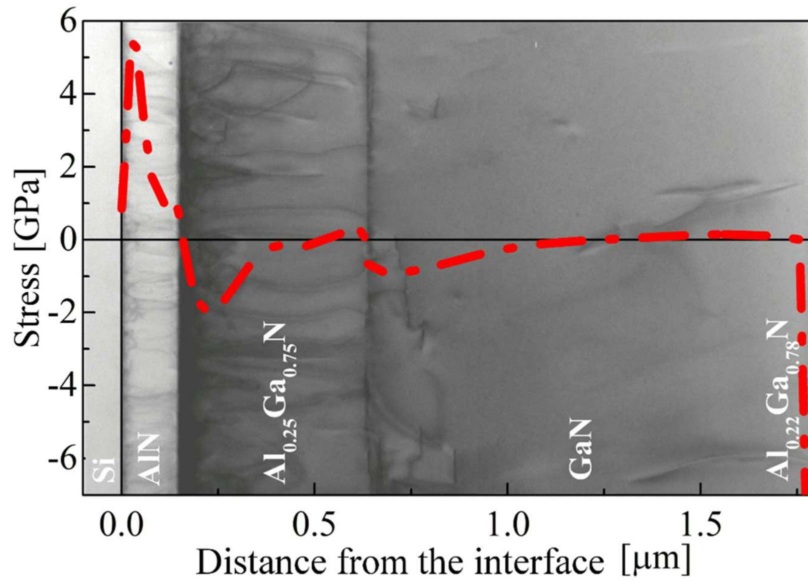

Figure 25: The residual stress profile of a HEMT heterostructure (Figure 4a) is plotted as a function of the distance from the substrate. In the background, a STEM image shows the dislocation density variation across the investigated heterostructure.

3.5 Raman Spectroscopy

Raman spectroscopy has become a well-established tool for the quantitative characterization of residual stress within semiconductor materials. In micro (μ-) Raman spectroscopy, which combines optical microscopy with Raman spectroscopy, the sample surface is probed by focused spot of polarised laser light. Within the investigated material, the photons get inelastically scattered by lattice vibrations (phonons) [63]. Since different materials/phases have unique phonon modes, the detection and spectral analysis of the scattered light (after polarization) serves as a fingerprint for the particular crystal structure. The spectrum of a relaxed HEMT structure (Figure 4a) was measured in $z(x, y)\bar{z}$ geometry as shown in Figure 26 [63]. In this mode, the direction of the incident and scattered light is parallel to the thin film normal (z-axis) and the polarisers in front of the incident and scattered beams are adjusted to be parallel to the x- and y-axes, respectively (see Figure 26b).

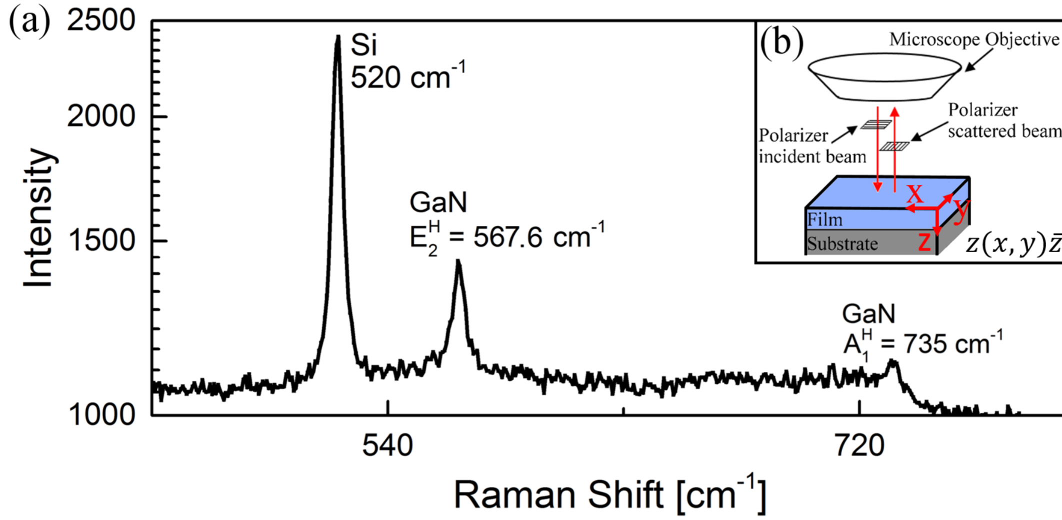

Figure 26: (a) A representativte Raman spectrum of an unstrained GaN sublayer of the HEMT structure, recorded in $z(x,y)\bar{z}$ geometry (b). Two characteristic GaN phonon peaks E_2^H and A_1^H peaks are visible at 567.6 cm^{-1} and 734 cm^{-1}.

The spectrum in Figure 26a shows three characteristic phonon peaks, from which the E_2^H (567.6 cm^{-1}) and A_1^H (734 cm^{-1}) as well as the peak at 520 cm^{-1} origin from the GaN and the Si substrate, respectively. Due to the small scattering volume of the AlN and $Al_{0.25}Ga_{0.75}N$ sublayers as well as the signal adsorption within the GaN sublayer, there are no peaks from these sublayers visible in the spectrum. The E_2^H and A_1^H peaks of unstrained AlN usually appear at 657.4 cm^{-1} and 890 cm^{-1} [63]. However, tensile/compressive stresses modify the individual phonon modes, resulting in a Raman peak shift towards lower/higher frequencies. Typically, in $Al_xGa_{1-x}N$ structures the residual stress is quantified on basis of the E_2^H peak position by using the following equations [64]:

$$\Delta\omega = K \cdot \sigma_{xx} \tag{15}$$

with K as the linear stress-shift coefficient and $\Delta\omega$ as the difference to the reference peak position. For more details about Raman spectroscopy on $Al_xGa_{1-x}N$ structures see reference [63,65].

In order to measure depth resolved stress gradients using Raman spectroscopy, we have introduce a new approach, namely incremental Raman spectroscopy. This approach requires a FIB/SEM device with an integrated Raman microscope. The presented study was carried out on a Tescan GAIA3 FIB/SEM workstation equipped with a Raman spectrometer. The principle is similar to FIB-DIC measurements, where a film is incrementally removed, in order to release the residual film stress in a step wise manner. However, incremental Raman spectroscopy quantifies the stress relaxation by spectral Raman analyses, rather than DIC from sample geometry deformations.

Since this concept is new and has not been applied before, a methodological study was performed on the heterostructure, illustrated in Figure 4a. Therefore, a pillar with square cross-section geometry (5×5 µm^2) was fabricated by using FIB milling (see Figure 27a). Subsequently the pillar faces were coated with gold, in order to ensure fast heat dissipation during Raman excitation and to prevent ion beam damage during subsequent FIB milling steps. Next, the heterostructure was incrementally removed in steps of ~100 nm. After each milling step Raman spectra were recorded by using an excitation wavelength of 532.4 nm in $z(x,y)\bar{z}$ geometry. The thickness of the removed film section (t_i) was measured using SEM cross-section imaging (Figure 27b).

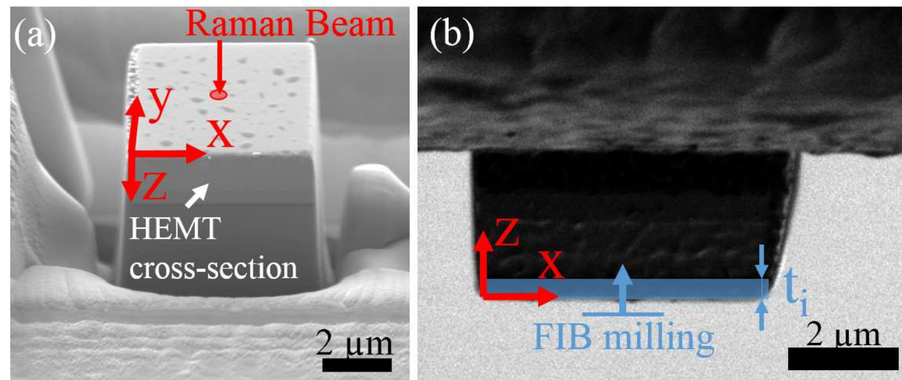

Figure 27: (a) SEM image of the initial pillar geometry. The milling and Raman direction were parallel to the sample normal (z-axis). (b) Slices, parallel to the x-y plane with a thickness of t_i were removed in a step wise manner.

The E_2^H phonon peak positions of the AlN, $Al_{0.25}Ga_{0.75}N$ and GaN sublayers were investigated after each milling step. The GaN like E_2^H phonon peak at 574 cm^{-1} was taken as the unstrained $Al_{0.25}Ga_{0.75}N$ reference position [63]. The stress values were quantified by the E_2^H peak shifts ($\Delta\omega$) with K values for AlN (K = 3.4 cm^{-1} GPa), $Al_{0.25}Ga_{0.75}N$ (K = 4.1 cm^{-1} GPa), GaN (K = 4.3 cm^{-1} GPa), taken from literature [66,67] (see Eq. 15).

Figure 28 shows SEM images of the pillar at particular milling steps, with their associated Raman spectrum in reversed order. The discrepancies between the unstrained and the measured Si positions were taken as offset values for the calibration of the recorded Raman spectra. Subsequently, the sublayer peak positions were corrected, according to the measured offset values. The corrected peak positions are a direct measure for the mean sublayer stress $\bar{\sigma}_i$ within the remaining thin film after the ith milling step. The sublayer stress gradients were deduced by considering the $\bar{\sigma}_i$ variations in reversed order: Hence i = 0 indicates the last milling step, where the entire heterostructure was removed and *i* increases for each previous milling step (see Figure 28a-d):

i = 0 (Figure 28a)*:* The recorded Raman spectrum displays solely the Si substrate.

i = 2 (Figure 28b): The AlN peak appears and reveals the average stress within the AlN layer at a heterostructure thickness of $t_{total,2}$, with $t_{total,i} = x_i - x_0$. The incremental stress σ_i within the removed segment *i* was calculated by using following formulas:

$$\sigma_i = \frac{\bar{\sigma}_i \cdot t_{total,i} - \sum_{j=m}^{i-1} t_j \cdot \sigma_j}{t_i} \tag{16}$$

$$t_i = t_{total,i} - t_{total,i-1} \tag{17}$$

The calculations were carried out for each layer separately, by considering only milling steps *i* within the AlN ($m = 0 < i \leq 2$), $Al_{0.25}Ga_{0.75}N$ ($m = 2 < i \leq 5$) and GaN ($m = 5 < i \leq 14$) sublayers.

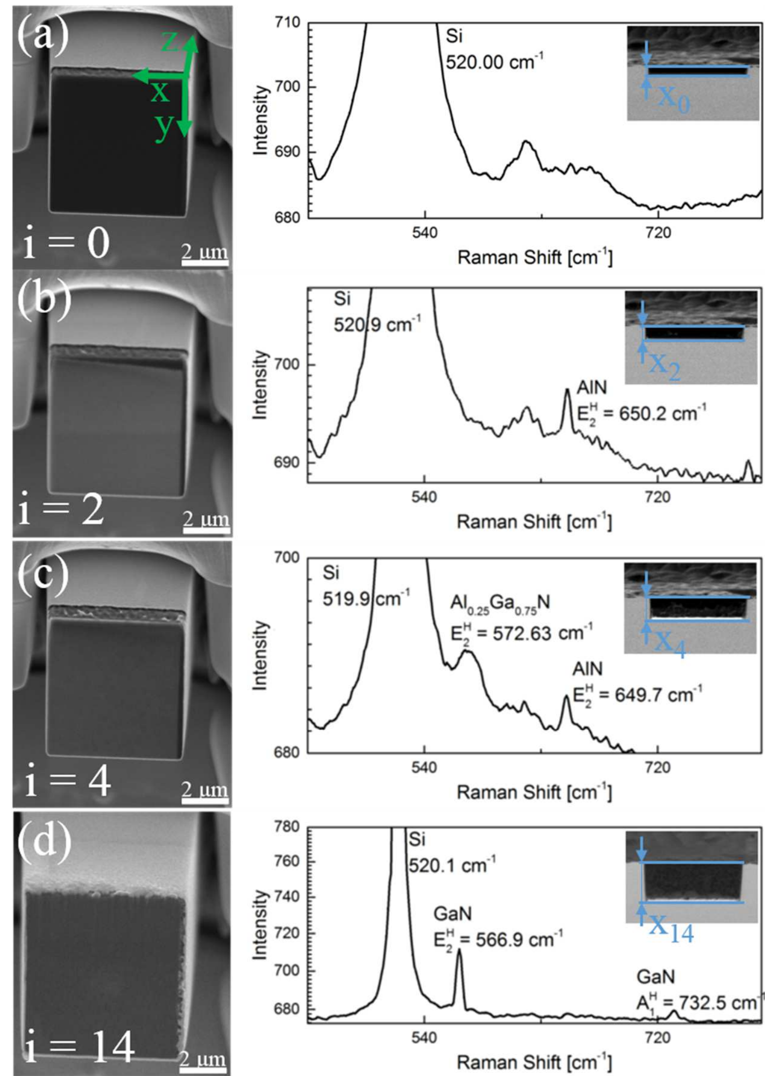

Figure 28 SEM images and the corresponding Raman spectra after the individual milling steps, in the reversed order. (a) The last milling step, where the entire heterostructure is removed, (b-d) previous milling steps, where the individual sublayer phonon peaks appear. The incremental milling steps were determined by pillar cross-section imaging (SEM insets).

Figure 29 shows the obtained stress gradient through the investigated heterostructure. The profile has the same trend as the stress data obtained by other experimental approaches.

However, this study represent a new experimental approach and differs from commonly used depth resolved Raman measurements [68]. The incremental Raman spectroscopy allows to record stress profiles in top view ($z(x, y)\bar{z}$ geometry) rather than cross-section view. In cross-section view the probed sample area determines the spatial resolution. Since the minimum spot size is in the range of 600 nm, the achievable spatial resolution is rather limited [52]. For the incremental Raman approach, however, the spatial resolution is independent of the beam spot size and solely determined by the FIB milling step size and the related ion beam damage.

Although the first incremental Raman spectroscopy results have been very promising, there are still some open questions, which have to be resolved. First, the impact of absorbed AlN and $Al_{0.25}Ga_{0.75}N$ signal on the GaN peak position is unclear. Secondly, the gold cover, which had acted as a heat sink had been degraded during FIB imaging. Subsequently, the heat dissipation properties change and phonon modes may have been affected by thermally induced lattice vibrations. Thirdly, different sample geometries and dimensions have to be tested in order to find a concept, which prevents stress relaxation and provides a large surface for rapid heat dissipation. Future studies will address these questions, in order to combine the great strain sensitivity of Raman Spectroscopy, of $1\cdot10^{-4}$ [69], with the spatial resolution of the incremental FIB milling approach.

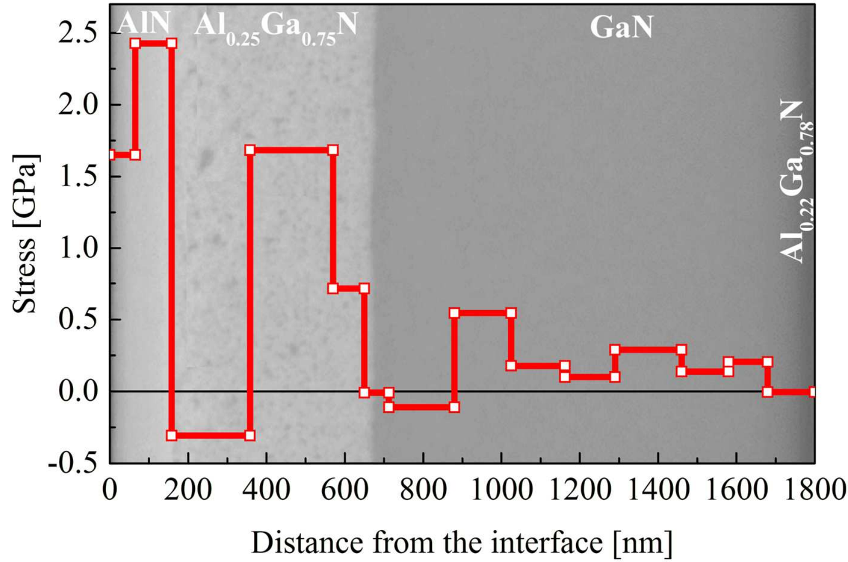

Figure 29: Stress profile obtained using incremental FIB/Raman approach. In the background, a SEM image shows the across the investigated heterostructure.

3.6 Advantages and disadvantages of the applied stress analyses

In the comparative study, all previously described stress measurement methods were performed on the same HEMT structure (Figure 4a). Hence, the acquired results were correlated with each other and subsequently the advantages and disadvantages of the individual approaches are discussed. Figure 30 shows the stress profiles, obtained by ion beam layer removal method (ILR), *in-situ* wafer curvature (WC), Raman spectroscopy (Raman), X-ray diffraction (XRD) as well as precession electron diffraction (PED). In order to compare the experimental c_{exp}/a_{exp} ratio profile from the PED analysis with the stress dependencies from other measurements, following equations were applied:

$$\varepsilon_{xx} = \frac{a_{exp} - a_0}{a_0} \qquad \rightarrow a_{exp} = \varepsilon_{xx} \cdot a_0 + a_0 \qquad (18)$$

$$\varepsilon_{zz} = \frac{c_{exp} - c_0}{c_0} \qquad \rightarrow c_{exp} = \varepsilon_{zz} \cdot c_0 + c_0 \qquad (19)$$

$$\varepsilon_{xx} = -\upsilon \cdot \varepsilon_{zz} \quad (20)$$

Here υ is the Poisson's ratio and the indices '*exp*' and '*0*' refer to the experimental and the strain-free reference values. By combining equations (18) with (19) and substituting ε_{zz} according to equation (20) the c_{exp}/a_{exp} was converted into in-plane strain values by:

$$\frac{a_{exp}}{c_{exp}} = \frac{c_0\,(-\nu \cdot \varepsilon_{xx}) + c_0}{a_0 \cdot\ \varepsilon_{xx} + a_0} \qquad \rightarrow \varepsilon_{xx} = \frac{c_0 - a_0 \cdot {}^{c_{exp}}/_{a_{exp}}}{a_0 \cdot {}^{c_{exp}}/_{a_{exp}} + c_0 \cdot \upsilon} \quad (21)$$

Subsequently, the plotted stress profile was calculated using Poisson's ratio values from literature (ν_{AlN}= 0.203; $\nu_{Al_{0.22}Ga_{0.78}N}$= 0.191; $\nu_{Al_{0.25}Ga_{0.75}N}$= 0.190; ν_{GaN}= 0.183) [70] and Eq. (12).

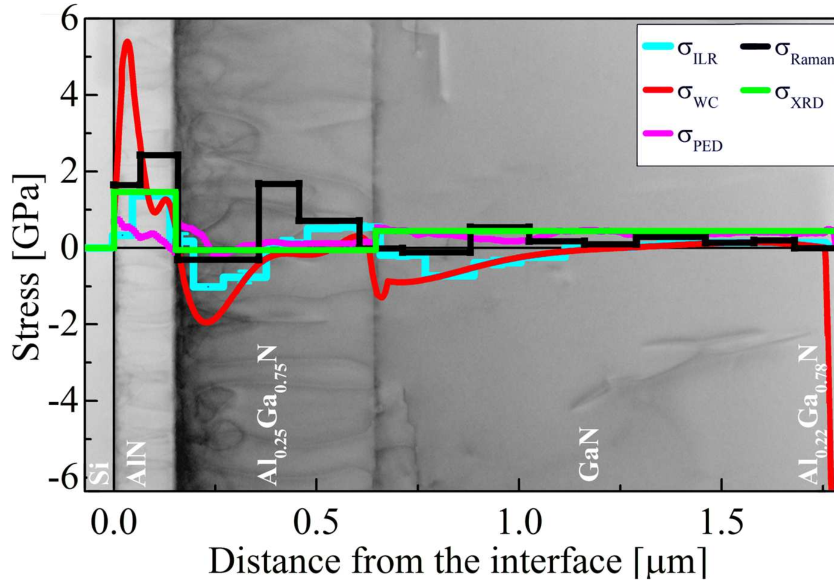

Figure 30 displays the stress profiles of all performed depth resolved stress measurements. In the background, a STEM image shows the dislocation density variation across the investigated heterostructure.

Generally, the results of the performed analyses are in good agreement. All depth resolved measurements exhibit a tensile stressed AlN sublayer as well as a compressive to tensile stress transition within the $Al_{0.25}Ga_{0.75}N$ and GaN sublayers. However, the 20 nm thick

$Al_{0.22}Ga_{0.78}N$ barrier is below the resolution limit for most of the applied techniques. Solely HRTEM and XRD approaches have provided decent information on the $Al_{0.22}Ga_{0.78}N$ barrier layer. Both studies have shown in-plane tensile stress, which is caused by pseudomorphic layer growth. The sublayer stress gradient evolution and influence of dislocations have been discussed in *section A, B* and *C* as well as in *section 2.2*.

Although the basic trends correlate very well, the stress magnitudes differ significantly. The high discrepancy between the AlN stress level obtained by *in-situ* wafer curvature analysis and the other measurements may originate from a relaxation mechanism during cooling down [21]. Although, the overall thermal stress contribution is considered as well, very local relaxation mechanism, as in the AlN sublayer, cannot be detected by *in-situ* wafer curvature analysis.

In contrast to that, the Raman stress profile deviates from the ILR results within the $Al_{0.25}Ga_{0.75}N$ sublayer. Here the tensile stress level is overestimated in comparison to other investigations. However, since there is a lack of an unstressed $Al_{0.25}Ga_{0.75}N$ reference spectrum the unstained E_2^H position was taken from literature [63]. An experimentally determined reference position as well as K value would significantly improve the accuracy of the $Al_{0.25}Ga_{0.75}N$ stress data. Furthermore smaller FIB milling steps would increase the spatial resolution of the stress profile.

PED analyses suffer from the collection of strain-free reference patterns. It is rather difficult to fabricate a suitable stress-free electron transparent lamella. Owing to the relief of residual stress, the lamella bends strongly and is misaligned in the strain-free reference region. In order to record reference DPs with the required zone axis orientation, the patterns have been acquired at a slightly strained section, which was less bent. As a consequence, the PED stress profile shows the same trend as the other measurements, however, the sublayer stress magnitudes are underestimated.

Table 3. and Table 4. list the major features, advantages and disadvantages of the methods applied. The most significant differences between the individual approaches are the complexity of sample preparation procedures, effort for data evaluation, stress resolution as well as required facilities.

Hence, the different techniques are favourable for different stages in the product life cycle of a HEMT device. For the development of multilayer designs and failure analysis, high resolution methods as ILR as well as PED are beneficial for residual stress analysis. However, these methods are relatively time consuming and not suitable for in-line stress characterization. For this purpose XRD based reciprocal space mapping and *in-situ* wafer curvature are the analytical tools used primarily by the semiconductor industry. Both of these techniques, provide a sufficient spatial resolution and can be run in a fully automatised manner.

Method	**Resolution limit**	**Required equipment**	**Stress gradient obtainable/ Strain accuracy**	**Effort**
FIB/DIC	10 nm	SEM/FIB	Yes / $1 \cdot 10^{-4}$ *	High
PED	2 nm	TEM with a built in precession tool	Yes / $1 \cdot 10^{-4}$	Very high
***In-Situ* Wafer Curvature**	~ 50 nm	Deposition reactor with built in laser curvature device	Yes / $6 \cdot 10^{-3}$ **	Medium
XRD *(Reciprocal space mapping)*	Sublayer thickness	X-ray diffractometer	No / $1 \cdot 10^{-5}$	Low
Incremental Raman Spectroscopy	~100 nm	FIB/SEM equipped with a Raman microscope	Yes / $1 \cdot 10^{-4}$	High

Table 3.: The most significant features of the performed depth resolved stress analyses. The strain accuracy values of PED [49], XRD [52], FIB/DIC [71] and Raman Spectroscopy [69] were taken from literature. * The strain accuracy for four-slot milling geometry analyses. ** For a 50 nm thick GaN film, by considering a resolution limit of ± 5 km^{-1} for the installed LAYTEC Epi TT system.

Method	Advantages	Disadvantage
ILR	+ Stress gradients with high spatial resolution + Independent from film crystal structure + No strain-free reference is required	– Very time consuming – Finite element simulation for accurate stress gradient required
PED	+ High spatial resolutions are achievable + Stress measurement can be combined with structural TEM analysis	– TEM with built in precession tool is required – Strain-free reference sample is required – Complex sample preparation procedure
***In-Situ* Wafer Curvature**	+ In-line stress evaluation + Every wafer can be monitored + No dedicated sample preparation is required + Quantitative stress profile	– The impact of thermal stress on stress profile is still under investigation – Simplifications were taken to evaluate curvature data – Lowest strain resolution
XRD *(Reciprocal space mapping)*	+ Barrier layer can be resolved + Additional information on defects and composition + Low requirements for sample preparation + Fully automatised	– Sublayer stress gradients cannot be resolved quantitatively – Only single crystalline samples
Incremental Raman Spectroscopy	+ Sublayer stress gradient are obtainable + No Stress simulation is required + High strain accuracy	– Methodological improvement is required – Only crystalline and Raman active samples – Low availability of FIB/SEM devices with built in Raman microscopes

Table 4.: An overview of the major advantages and disadvantages of the described characterization methods.

4

Bibliography

[1] A. Rockett, *The Materials Science of Semiconductors*, Springer US, New York, 2008.

[2] B. Zhang, Y. Liu, A review of GaN-based optoelectronic devices on silicon substrate, *Chinese Sci. Bull.* **59** (2014) 1251–1275. doi:10.1007/s11434-014-0169-x.

[3] D. Zhu, D.J. Wallis, C.J. Humphreys, Prospects of III-nitride optoelectronics grown on Si., *Rep. Prog. Phys.* **76** (2013) 106501. doi:10.1088/0034-4885/76/10/106501.

[4] I. Vurgaftman, J.R. Meyer, L.R. Ram-Mohan, Band parameters for III-V compound semiconductors and their alloys, *J. Appl. Phys.* **89** (2001) 5815–5875. doi:10.1063/1.1368156.

[5] R. Quay, *Gallium Nitride Electronics*, Springer, Heidelberg, 2008.

[6] M. Su, C. Chen, S. Rajan, Prospects for the application of GaN power devices in hybrid electric vehicle drive systems, *Semicond. Sci. Technol.* **28** (2013) 74012. doi:10.1088/0268-1242/28/7/074012.

[7] S. Li, C. Ouyang, First principles study of wurtzite and zinc blende GaN: a comparison of the electronic and optical properties, *Phys. Lett. A.* **336** (2005) 145–151. doi:10.1016/j.physleta.2005.01.009.

[8] A. Lidow, J. Strydom, M. de Rooij, D. Reusch, *GaN Transistors for Efficient Power Conversion,* John Wiley & Sons, Chichester, 2015.

[9] H. Morkoç, *Nitride Semiconductor Devices.* Vol 1, Wiley-VCH, Weinheim, 2008. doi:10.1002/9783527628438.

[10] T. Baltynov, *Innovative Approaches for AlGaN/GaN-based Technology*, University of Sheffield, 2016.

[11] M. Higashiwaki, T. Mimura, T. Matsui, AlGaN/GaN heterostructure field-effect transistors on 4H-SiC substrates with current-gain cutoff frequency of 190 GHz, *Appl. Phys. Express.* **1** (2008) 21103. doi:10.1143/APEX.1.021103.

[12] B.A. Danilchenko, N.A. Tripachko, A.E. Belyaev, S.A. Vitusevich, H. Hardtdegen, H. Lüth, High-field quasi-ballistic transport in AlGaN/GaN heterostructures, *Appl. Phys. Lett.* **104** (2014) 72105. doi:10.1063/1.4866281.

[13] H. Kamata, Y. Ishii, T. Mabuchi, K. Naoe, S. Ajimura, S. K., Single crystal growth of Aluminum Nitride, *Fujikura Tech. Rev.* (2009) 42–45.

[14] T.J. Flack, B.N. Pushpakaran, S.B. Bayne, GaN Technology for Power Electronic Applications: A Review, *J. Electron. Mater.* **45** (2016) 2673–2682. doi:10.1007/s11664-016-4435-3.

[15] S.K. O'Leary, B.E. Foutz, M.S. Shur, U.V. Bhapkar, L.F. Eastman, Monte Carlo simulation of electron transport in wurtzite aluminum nitride, *Solid State Commun.* **105** (1998) 621–626. doi:10.1016/S0038-1098(97)10207-1.

[16] R.S. Pengelly, S.M. Wood, J.W. Milligan, S.T. Sheppard, W.L. Pribble, A review of GaN on SiC high electron-mobility power transistors and MMICs, *IEEE Trans. Microw. Theory Tech.* **60** (2012) 1764–1783. doi:10.1109/TMTT.2012.2187535.

[17] H.P. Maruska, J.J. Tietjen, The preparation and properties of vapor-deposited single-crystal-line GaN, *Appl. Phys. Lett.* **15** (1969) 327–329. doi:10.1063/1.1652845.

[18] G. Li, W. Wang, W. Yang, Y. Lin, H. Wang, Z. Lin, S. Zhou, GaN-based light-emitting diodes on various substrates: a critical review, *Reports Prog. Phys.* **79** (2016) 56501. doi:10.1088/0034-4885/79/5/056501.

[19] L. Liu, J.H. Edgar, Substrates for gallium nitride epitaxy, *Mater. Sci. Eng. R.* **37** (2002) 61–127.

[20] H. Lenka, J. Meersschaut, P.K. Kandaswamy, H. Modarresi, H. Bender, A. Vantomme, W. Vandervorst, Dislocation density and tetragonal distortion of a GaN epilayer on Si(111): A comparative RBS/C and TEM study, *Nucl. Instruments Methods Phys. Res. Sect. B Beam Interact. with Mater. Atoms.* **331** (2014) 69–73. doi:10.1016/j.nimb.2014.02.014.

[21] H.F. Liu, S.B. Dolmanan, L. Zhang, S.J. Chua, D.Z. Chi, M. Heuken, S. Tripathy, Influence of stress on structural properties of AlGaN/GaN high electron mobility transistor layers grown on 150 mm diameter Si (111) substrate, *J. Appl. Phys.* **113** (2013) 23510. doi:10.1063/1.4774288.

[22] R. Datta, M.J. Kappers, M.E. Vickers, J.S. Barnard, C.J. Humphreys, Growth and characterisation of GaN with reduced dislocation density, *Superlattices Microstruct.* **36** (2004) 393–401. doi:10.1016/j.spmi.2004.09.003.

[23] U.W. Pohl, *Epitaxy of Semiconductors*, Springer, Heidelberg, 2010. doi:10.1007/978-3-642-32970-8.

[24] S. Chang, L. Lung Wei, T. Tung Luong, C. Chang, L. Chang, Threading dislocation reduction in three-dimensionally grown GaN islands on Si(111) substrate with AlN/AlGaN buffer layers, *J. Appl. Phys.* **122** (2017) 105306. doi:10.1063/1.5002079.

[25] S.K. Mathis, A.E. Romanov, L.F. Chen, G.E. Beltz, W. Pompe, J.S. Speck, Modeling of Threading Dislocation Reduction in Growing GaN Layers, *J. Cryst. Growth.* **231** (2001) 371–390. doi:10.1002/1521-396X(200005)179:1.

[26] E. V. Etzkorn, D.R. Clarke, Cracking of GaN films, *J. Appl. Phys.* **89** (2001) 1025–1034. doi:10.1063/1.1330243.

[27] W.D. Nix, B.M. Clemens, Crystallite coalescence: A mechanism for intrinsic tensile stresses in thin films, *J. Mater. Res.* **14** (1999) 3467–3473. doi:10.1557/JMR.1999.0468.

[28] M. Reisinger, M. Tomberger, J. Zechner, I. Daumiller, B. Sartory, W. Ecker, J. Keckes, R.T. Lechner, Resolving alternating stress gradients and dislocation densities across $Al_xGa_{1-x}N$ multilayer structures on Si(111), *Appl. Phys. Lett.* **111** (2017) 162103. doi:10.1063/1.4998694.

[29] M. Reisinger, J. Zalesak, R. Daniel, M. Tomberger, J.K. Weiss, A.D. Darbal, M. Petrenec, J. Zechner, I. Daumiller, W. Ecker, B. Sartory, J. Keckes, Cross-sectional stress distribution in $Al_xGa_{1-x}N$ heterostructure on Si(111) substrate characterized by ion beam layer removal method and precession electron diffraction, *Mater. Des.* **106** (2016) 476–481. doi:10.1016/j.matdes.2016.06.001.

[30] A.E. Romanov, J.S. Speck, Stress relaxation in mismatched layers due to threading dislocation inclination, *Appl. Phys. Lett.* **83** (2003) 2569–2571. doi:10.1063/1.1613360.

[31] D.M. Follstaedt, S.R. Lee, A.A. Allerman, J.A. Floro, Strain relaxation in AlGaN multilayer structures by inclined dislocations, *J. Appl. Phys.* **105** (2009) 83507. doi:10.1063/1.3087515.

[32] J.S. Speck, S.J. Rosner, The Role of Threading Dislocations in the Physical Properties of GaN and its Alloys, *Phys. B.* **231** (1999) 373–374. doi:10.1016/S0022-0248(01)01468-3.

[33] R.F. Davis, S. Einfeldt, E.A. Preble, A.M. Roskowski, Z.J. Reitmeier, P.Q. Miraglia, Gallium nitride and related materials: Challenges in materials processing, *Acta Mater.* **51** (2003) 5961–5979. doi:10.1016/j.actamat.2003.08.005.

[34] X. Xu, X. Liu, X. Han, H. Yuan, J. Wang, Y. Guo, H. Song, G. Zheng, H. Wei, S. Yang, Q. Zhu, Z. Wang, Dislocation scattering in $Al_xGa_{1-x}N$/GaN heterostructures, *Appl. Phys. Lett.* **93** (2008) 182111. doi:10.1063/1.3013836.

[35] A.E. Romanov, G.E. Beltz, P. Cantu, F. Wu, S. Keller, S.P. Denbaars, J.S. Speck, Cracking of III-nitride layers with strain gradients, *Appl. Phys. Lett.* **89** (2006) 161922. doi:10.1063/1.2352043.

[36] A.D. Bykhovski, B.L. Gelmont, M.S. Shur, Elastic strain relaxation and piezoeffect in GaN-AlN, GaN-AlGaN and GaN-InGaN superlattices, *J. Appl. Phys.* **81** (1997) 6332. doi:10.1063/1.364368.

[37] R. Schöngrundner, R. Treml, T. Antretter, D. Kozic, W. Ecker, D. Kiener, R. Brunner, Critical assessment of the determination of residual stress profiles in thin films by means of the ion beam layer removal method, *Thin Solid Films*. **564** (2014) 321–330. doi:10.1016/j.tsf.2014.06.003.

[38] M. Sebastiani, C. Eberl, E. Bemporad, G.M. Pharr, Depth-resolved residual stress analysis of thin coatings by a new FIB-DIC method, *Mater. Sci. Eng. A*. **528** (2011) 7901–7908. doi:10.1016/j.msea.2011.07.001.

[39] S. Massl, J. Keckes, R. Pippan, A new cantilever technique reveals spatial distributions of residual stresses in near-surface structures, *Scr. Mater.* **59** (2008) 503–506. doi:10.1016/j.scriptamat.2008.04.037.

[40] S. Massl, J. Keckes, R. Pippan, A direct method of determining complex depth profiles of residual stresses in thin films on a nanoscale, *Acta Mater.* **55** (2007) 4835–4844. doi:10.1016/j.actamat.2007.05.002.

[41] S. Massl, H. Köstenbauer, J. Keckes, R. Pippan, Stress measurement in thin films with the ion beam layer removal method: Influence of experimental errors and parameters, *Thin Solid Films*. **516** (2008) 8655–8662. doi:10.1016/j.tsf.2008.06.091.

[42] R. Hammer, J. Todt, J. Keckes, B. Sartory, G. Parteder, J. Kraft, S. Defregger, High resolution residual stress gradient characterization in W/TiN-stack on Si(100): Correlating in-plane stress and grain size distributions in W sublayer, *Mater. Des.* **132** (2017) 72–78. doi:10.1016/j.matdes.2017.06.052.

[43] D.B. Williams, C.B. Carter, *Transmission Electron Microscopy*, Springer US, New York, 2009. doi:10.1007/978-0-387-76501-3.

[44] A. Kadir, C.C. Huang, K.E.K. Lee, E.A. Fitzgerald, S.J. Chua, Determination of alloy composition and strain in multiple AlGaN buffer layers in GaN/Si system, *Appl. Phys. Lett.* **105** (2014) 232113. doi:10.1063/1.4904007.

[45] A. Béché, J.L. Rouvière, J.P. Barnes, D. Cooper, A. Beche - Strain measurement at the nanoscale Comparison between CBED, nano-beam electron diffraction, high resolution imaging and dark field electron holography, *Ultramicroscopy*. **131** (2013) 10–23. doi:10.1016/j.ultramic.2013.03.014

[46] M.J. Hÿtch, E. Snoeck, R. Kilaas, Quantitative measurement of displacement and strain fields from HREM micrographs, *Ultramicroscopy*. **74** (1998) 131–146. doi:10.1016/S0304-3991(98)00035-7.

[47] M.J. Hÿtch, F. Houdellier, Mapping stress and strain in nanostructures by high-resolution transmission electron microscopy, *Microelectron. Eng*. **84** (2007) 460-463. doi:10.1016/j.mee.2006.10.062.

[48] C.H. Tsai, S.R. Jian, J.Y. Juang, Berkovich nanoindentation and deformation mechanisms in GaN thin films, *Appl. Surf. Sci.* **254** (2008) 1997–2002. doi:10.1016/j.apsusc.2007.08.022.

[49] P.A. Midgley, A.S. Eggeman, Precession electron diffraction - A topical review, *IUCrJ*. **2** (2015) 126–136. doi:10.1107/S2052252514022283.

[50] J. Portillo, E.F. Rauch, S. Nicolopoulos, M. Gemmi, D. Bultreys, Precession Electron Diffraction Assisted Orientation Mapping in the Transmission Electron Microscope, *Mater. Sci. Forum.* **644** (2010) 1–7. doi:10.4028/www.scientific.net/MSF.644.1.

[51] P.J. Phillips, M.C. Brandes, M.J. Mills, M. de Graef, Diffraction contrast STEM of dislocations: Imaging and simulations, *Ultramicroscopy*. **111** (2011) 1483–1487. doi:10.1016/j.ultramic.2011.07.001.

[52] S. Di Fonzo, W. Jark, S. Lagomarsino, C. Glannini, L. De Caro, a Cedola, M. Müller, Non-destructive determination of strain 100-nanometre spatial resolution, *Nature*. **403** (2000) 638–640. doi:10.1038/35001035.

[53] U. Pietsch, V. Holy, T. Baumbach, *High Resolution X-ray Scattering*, 2nd ed., Springer, New York, 2004. doi:10.1007/978-1-4757-4050-9.

[54] M.A. Moram, M.E. Vickers, X-ray diffraction of III-nitrides, *Reports Prog. Phys.* **72** (2009) 36502. doi:10.1088/0034-4885/72/3/036502.

[55] T. Konya, X-ray thin-film measurement techniques III. High resolution X-ray diffractometry, Rigaku J. 25 (2009). available at http://chemport.cas.org/cgi-bin/sdcgi?APP=ftslink&action=reflink&origin=aip&version=1.0&coi=1%3ACAS%3A528%3ADC%252BD1MXhtlWlsbfL&md5=99b5a2e5096182c866ec53c15e811527.

[56] P.F. Fewster, Reciprocal space mapping, *Crit. Rev. Solid State Mater. Sci.* **22** (1997) 69–110. doi:10.1080/10408439708241259.

[57] T. Metzger, R. Höpler, E. Born, O. Ambacher, M. Stutzmann, R. Stömmer, M. Schuster, H. Göbel, S. Christiansen, M. Albrecht, H.P. Strunk, Defect structure of epitaxial GaN films determined by transmission electron microscopy and triple-axis X-ray diffractometry, *Philos. Mag. A*. **77** (1998) 1013–1025. doi:10.1080/01418619808221225.

[58] T. Islam, J. Zechner, M. Bernardoni, M. Nelhiebel, R. Pippan, A novel setup for wafer curvature measurement at very high heating rates, *Rev. Sci. Instrum.* **88** (2017) 24709. doi:10.1063/1.4975378.

[59] G.G. Stoney, The Tension of Metallic Films Deposited by Electrolysis, *Proc. R. Soc. London A*. **82** (1909) 172–175. doi:10.1098/rspa.1909.0021.

[60] A. Krost, A. Dadgar, F. Schulze, J. Bläsing, G. Strassburger, R. Clos, A. Diez, P. Veit, T. Hempel, J. Christen, In situ monitoring of the stress evolution in growing group-III-nitride layers, *J. Cryst. Growth.* **275** (2005) 209–216. doi:10.1016/j.jcrysgro.2004.10.090.

[61] J.A. Floro, E. Chason, S.R. Lee, R.D. Twesten, R.Q. Hwang, L.B. Freund, Real-time stress evolution during $Si_{1-x}Ge_{-x}$ Heteroepitaxy: Dislocations, islanding, and segregation, *J. Electron. Mater.* **26** (1997) 969–979. doi:10.1007/s11664-997-0233-2.

[62] Y. Cordier, N. Baron, F. Semond, J. Massies, M. Binetti, B. Henninger, M. Besendahl, T. Zettler, In situ measurements of wafer bending curvature during growth of group-III-nitride layers on silicon by molecular beam epitaxy, *J. Cryst. Growth.* **301**–302 (2007) 71–74. doi:10.1016/j.jcrysgro.2006.11.126.

[63] H. Harima, Properties of GaN and related compounds studied by means of Raman scattering, *J. Phys. Condens. Matter.* **14** (2002) R967–R993. doi:10.1088/0953-8984/14/38/201.

[64] M. Kuball, Raman spectroscopy of GaN, AlGaN and AlN for process and growth monitoring/control, *Surf. Interface Anal.* **31** (2001) 987–999. doi:10.1002/sia.1134.

[65] H. Grille, C. Schnittler, F. Bechstedt, Phonons in ternary group-III nitride alloys, *Phys. Rev. B.* **61** (2000) 6091–6105. doi:10.1103/PhysRevB.61.6091.

[66] S. Tripathy, V.K.X. Lin, S. Vicknesh, S.J. Chua, Micro-Raman probing of residual stress in freestanding GaN-based micromechanical structures fabricated by a dry release technique, *J. Appl. Phys.* **101** (2007) 63525. doi:10.1063/1.2713089.

[67] S. Tripathy, S.J. Chua, P. Chen, Z.L. Miao, Micro-Raman investigation of strain in GaN and $Al_xGa_{1-x}N$/GaN heterostructures grown on Si(111), *J. Appl. Phys.* **92** (2002) 3503–3510. doi:10.1063/1.1502921.

[68] R. Korbutowicz, M. Tlaczala, J. Kovac, G. Irmer, R. Srnanek, Cross-sectional and surface Raman mapping of thick GaN layers, *Cryst. Res. Technol.* **43** (2008) 1339-1344. doi:10.1002/crat.200800245.

[69] A. Béché, J.L. Rouvière, J.P. Barnes, D. Cooper, Dark field electron holography for strain measurement, *Ultramicroscopy*. **111** (2011) 227–238.

[70] H.-P. Lee, J. Perozek, L.D. Rosario, C. Bayram, Investigation of AlGaN/GaN high electron mobility transistor structures on 200-mm silicon (111) substrates employing different buffer layer configurations, *Sci. Rep.* **6** (2016) 37588. doi:10.1038/srep37588.

[71] M. Sebastiani, C. Eberl, E. Bemporad, A.M. Korsunsky, W.D. Nix, F. Carassiti, Focused ion beam four-slot milling for Poisson's ratio and residual stress evaluation at the micron scale, *Surf. Coatings Technol.* **251** (2014) 151–161. doi:10.1016/j.surfcoat.2014.04.019.

5

List of Appended Publications

5.1 Papers in Scientific Journals

Paper A

M. Reisinger, J. Zalesak, R. Daniel, M. Tomberger, J.K.Weiss, A.D. Darbal, M. Petrenec, J. Zechner, I. Daumiller, W. Ecker, B. Sartory, J. Keckes

Cross-sectional stress distribution in $Al_xGa_{1-x}N$ heterostructure on Si(111) substrate characterized by ion beam layer removal method and precession electron diffraction

Materials and Design 106 (2016) 476–481; https://doi.org/10.1016/j.matdes.2016.06.001

Paper B

M. Reisinger, M. Tomberger, J. Zechner, I. Daumiller, B. Sartory, W. Ecker, J. Keckes, R. T. Lechner

Resolving alternating stress gradients and dislocation densities across $Al_xGa_{1-x}N$ multilayer structures on Si(111)

Appl. Phys. Lett. 111, 162103 (2017); http://dx.doi.org/10.1063/1.4998694

Paper C

M. Reisinger, C. Ostermaier, M. Tomberger, J. Zechner, B. Sartory, W. Ecker, I. Daumiller, J. Keckes

Matching in-situ and ex-situ recorded stress gradients in an $Al_xGa_{1-x}N$ heterostructure: Complementary wafer curvature analyses in time and space

submitted manuscript

5.2 Contribution of the authors to the papers

Paper/ Article	Conception and planning	Experiments	Analyses and interpretation	Manuscript preparation
A	80	90	80	80
B	90	100	100	100
C	90	80	100	100

Table 5.: Contribution of the Autor to the appended publication in percent.

Cross-sectional stress distribution in $Al_xGa_{1-x}N$ heterostructure on Si(111) substrate characterized by ion beam layer removal method and precession electron diffraction

M. Reisinger [a], J. Zalesak [b], R. Daniel [b], M. Tomberger [c], J. K. Weiss [d], A. D. Darbal [d], M. Petrenec [e], J. Zechner [f], I. Daumiller [c], W. Ecker [g], B. Sartory [g] and J. Keckes [a,*]

[a] Department of Materials Physics, Montanuniversität Leoben, Leoben, Austria

[b] Department of Physical Metallurgy and Materials Testing, Montanuniversität Leoben, Leoben, Austria

[c] Infineon Technologies Austria AG, Villach, Austria

[d] AppFive LLC, Tempe, Arizona, USA

[e] TESCAN Brno s.r.o., Libušina tř. 1, Brno, Czech Republic

[f] KAI Kompetenzzentrum Automobil- u. Industrieelektronik GmbH, Villach, Austria

[g] Materials Center Leoben Forschung GmbH, Roseggerstraße 12, Leoben, Austria

Abstract

A residual stress depth gradient is characterized in a 1.8 µm thick $AlN/Al_{0.25}Ga_{0.75}N/GaN/Al_{0.22}Ga_{0.78}N$ heteroepitaxial structure grown using metallic-organic chemical vapour deposition on Si(111) substrate. The cross-sectional stress profile

is evaluated with a step of 100 nm using ion beam layer removal (ILR) method based (i) on a sequential focused ion beam milling of a microcantilever, (ii) on an evaluation of a cantilever bending after every milling step and (iii) on a stress profile recalculation using finite element simulation. The profile shows tensile stress of ~1.5 GPa in AlN nucleation layer, stress changing from compressive to tensile in $Al_{0.25}Ga_{0.75}N$ and GaN sublayers and relatively small stresses below 100 MPa in the top $Al_{0.22}Ga_{0.78}N$ sublayer. The stress profile is qualitatively correlated with the results from precession electron diffraction which indicates approximately the same stress behaviour. The cross-sectional stress magnitude and variation are interpreted by the mismatches of lattice constants and coefficients of thermal expansion as well as by growth mode changes during $Al_{0.25}Ga_{0.75}N$ and GaN sublayer formation. The approach demonstrates the possibility to resolve nanoscale variation of residual stresses in heteroepitaxial structures using ILR method.

A.1 Introduction

GaN and related semiconductors possess extensive technological potential because of their remarkable optical and electrical properties utilized especially in high-power electronic and optical devices [1]. Due to the availability of relatively low costs and large size Si substrates, there has been a significant effort to grow GaN thin films on Si by metallic-organic-chemical-vapour-deposition (MOCVD) [2, 3]. There is however (i) a large lattice mismatch of ~17% and (ii) a large mismatch of coefficients of thermal expansion (CTEs) of ~−56% between Si and GaN [4, 5]. For this reason, several production quality issues like (i) insufficient GaN crystal quality, (ii) wafer bow, (iii) film brittleness and cracking and (iv) inhomogeneous film properties across the wafer had to be minimized [2, 6, 7].Most of those issues can be directly or indirectly related to stresses formed in the film during the MOCVD growth and during cooling down after the process [8, 9]. Therefore, the characterization, the understanding and the optimization of the stress state represent fundamental topics in the development of high crystal quality GaN films on heteroepitaxial substrates.

A.1 Introduction

In order to manage stresses in GaN thin films, an AlN nucleation layer and $Al_xGa_{1-x}N$ transition layers have been applied primarily (i) to minimize the wafer-bow and (ii) to produce crack-free $Al_xGa_{1-x}N$ films on Si [10, 11]. By changing the thickness, the morphology and the stoichiometry of the layers, it has been possible to tune the stress state in GaN effectively. Especially the growth of an AlN nucleation layer on Si(111) substrates represented a significant achievement in the stress management and in the improvement of GaN crystal quality [11, 12].

In majority of the cases, stress characterization in GaN films has been performed using X-ray diffraction (XRD), Raman spectroscopy and wafer-bow measurements [7, 11, 13]. Usually volume-averaged stresses were determined for individual sublayers or even for the complete heterostructures by analyzing (i) complete heterostructures or (ii) individual sub-layers in stepwise deposited heterostructures.

In order to effectively control stresses in $Al_xGa_{1-x}N$ heterostructures, there is a need to avoid especially tensile and compressive stress concentrations within the structures, which are favourable for crack initiation and subsequent propagation [14, 15]. In order to identify heterostructure regions with such critical stress states, a detailed cross-sectional stress characterization over the as-deposited structures at sub-micron scale is necessary.

The aim of this contribution is to characterize a residual stress profile in a representative $Al_xGa_{1-x}N$ heterostructure on Si(111) using focused ion beam (FIB) based ion beam layer removal (ILR) method. This relatively new experimental technique, first proposed in 2007, has been already applied to polycrystalline, single crystalline as well as amorphous thin films [16 – 20]. Also methodological aspects and related errors have been discussed extensively. The stress characterization is performed by analyzing the curvature of FIB machined micro-cantilevers which consist of the thin film and a certain portion of a substrate. The film is incrementally thinned by FIB and the stress state in the remaining film region is subsequently determined from the actual cantilever deflection. Since the deflection of the cantilever is recorded after each FIB milling step, the calculation of the internal stress profile across the film thickness with the spatial resolution of the milling steps is straightforward. The approach can be complimented with a finite-element (FE) simulation, considering anisotropic film and substrate elastic properties [19]. One very

important prerequisite to use the ILR method is the negligible plastic deformation within film and substrate during the whole FIB milling process. In this work, the ILR method is used for the first time to quantify stress gradients in an epitaxial heterostructures consisting of a sequence of single crystalline sublayers. Complementary precession electron diffraction [21 – 24] is used to verify the results from ILR method qualitatively.

A.2 Experiment

The $AlN/Al_{0.25}Ga_{0.75}N/GaN/Al_{0.22}Ga_{0.78}N$ heterostructure with a thickness of 1.8 µm was grown on a 6 inch Si wafer with (111) orientation using an Aixtron G5 planetary MOCVD reactor. Trimethylaluminum (TMA), trimethylgallium (TMG) and ammonia (NH_3) were used as precursors for aluminium, gallium and nitrogen, respectively. The carrier gas was hydrogen (H_2). Figure A.1. shows the heterostructure cross-sectional morphology with thicknesses and compositions of the individual sublayers.

A.2 Experiment

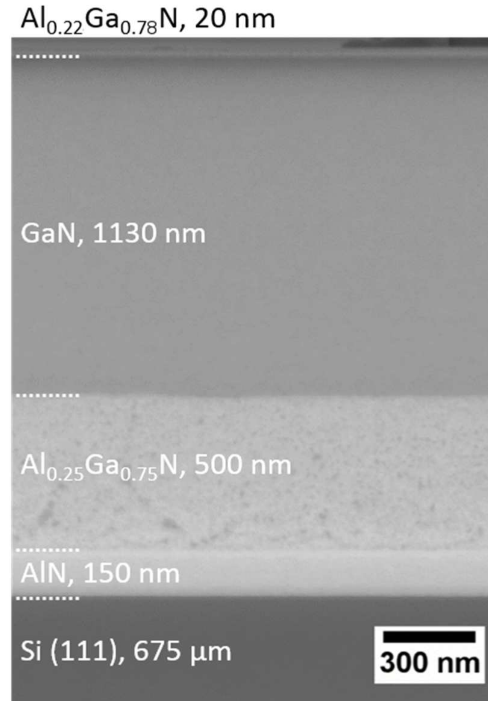

Figure A.1.: A scanning electron microscopy micrograph from the heterostructure on Si(111) substrate with thicknesses of the individual sublayers.

A Rigaku SmartLab 5 circle diffractometer equipped with a CuKα radiation, a parabolic multilayer mirror and a Ge(400) 2-bounce monochromator in the primary beam was used for an XRD analysis. A symmetric diffraction scan was used to obtain basic structural data from the heterostructure.

A plate with an area of 1×1 cm^2 was cut out from the wafer using a diamond wire saw. Subsequently, one edge of the plate was polished with an ion-polisher Hitachi E-3500 to remove the deformation layer produced by the saw cutting process. In this step, low energy Ar ions were used to remove the material which was not covered by a mask. In the vicinity of the pre-treated edge, a microcantilever with the dimensions of $110.9 \times 5.9 \times 3.4$ µm^3 (Figure A.2a) was fabricated using a Zeiss Auriga workstation, which combines a gallium operated focussed ion beam (FIB) and a high resolution scanning electron microscope (SEM).

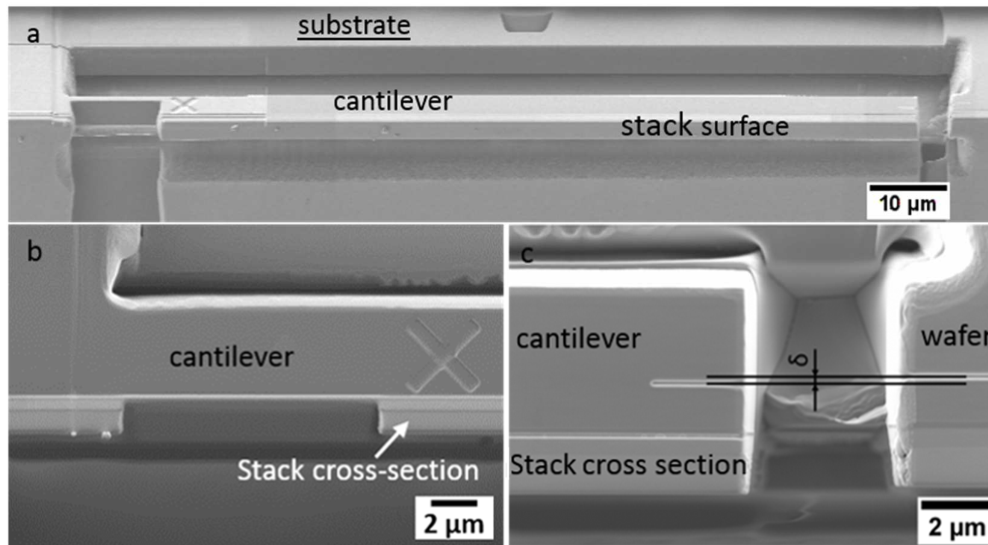

Figure A.2.: A scanning electron micrograph of a FIB machined microcantilever (a). A detailed view of the microcantilever with the region, which was incrementally milled in steps of 100 nm using FIB (b). The mutual positions of two markers milled into the microcantilever and into the wafer (c) were used to quantify the microcantilever deflection δ caused by the stress state in the remaining heterostructure region (b).

After the microcantilever was fabricated, it possessed a curvature caused by the presence of the residual stress state in the heterostructure. This curvature was quantified by the measurement of a deflection δ between the microcantilever and the remaining wafer (Figure A.2c). As a next step, heterostructure sections in the cantilever region from Figure A.2b were removed incrementally in steps of 100 nm using FIB. The gradual FIB milling was performed with a relatively low ion current of 50 pA and high voltage of 30 kV. After every milling step, the remaining thickness of the structure (Figure A.2b) and the deflection (Figure A.2c) were measured by SEM with accuracy better than ~14 nm. As supplementary material, Videos 1 and 2 are provided which were collected during the cantilever machining and show the stepwise material removal and the changes in the cantilever deflection δ.

A.2 Experiment

In order to determine the residual stress distribution *σ(z)* from the measured microcantilever deflections as a function of the heterostructure depth *z*, a three dimensional finite element model (FEM) using a commercial software package Abaqus was developed and used in a least square optimization procedure. In order to minimize the influence of the boundary conditions at the root of the cantilever, the geometrical model was not only reduced to the microcantilever itself but included also a block of the base structure of three times the width, about two times the height and about one third the length of the microcantilever. The boundary conditions fixed the displacement perpendicular to the limit faces of this block to zero. The cross-sectional heteroepitaxial structure morphology from Figure A.1. was considered. The elastic properties of the individual sublayers and Si from Table A.1. were used. The elastic behaviour of $Al_{0.25}Ga_{0.75}N$, $Al_{0.22}Ga_{0.78}N$ and GaN was set to be identical, which is, with respect to the small difference in the elastic constants of GaN and AlN, a reasonable assumption. The finite element mesh consisted of 84,180 s-order hexagonal brick elements with reduced integration (C3D8R). For performance reasons, the chosen maximum aspect ratio of 15 was rather high, but mesh sensitivity studies showed no negative effect onto the results. The residual stress distribution across the structure was determined using an iterative optimization until calculated deflections matched the experimental data. In the present case, a gradient-based Levenberg-Marquardt algorithm [25, 26] was used. The residual stress re-calculation procedure is described in detail in Refs. [19, 27].

Elastic constant	GaN	AlN	Si
C_{11}	390	410	165
C_{12}	145	149	64
C_{13}	106	99	
C_{33}	398	389	
C_{44}	105	125	80

Table A.1.: Single crystal elastic constants in GPa used in the FE model [28, 29, 30].

Based on the error analysis discussed in previous studies, residual stress magnitudes across the heteroepitaxial structure were determined using ILR method with an error smaller than ~15%.

In order to qualitatively verify the cross-sectional stress distributions in the heteroepitaxial structure determined using ILR, position-resolved precession electron diffraction (PED) patterns were acquired from a cross section of the layer stack. PED has been developed recently as a means to very precisely measure small amounts of elastic strain, and when combined with a field emission gun transmission electron microscope (TEM), the spatial resolution can approach 1 nm [21, 22]. For this purpose, two cross-sectional TEM lamellae with a thickness of ~100 nm were fabricated using a Tescan GAIA3 FIB workstation from the heterostructure. In order to protect the layer structure from ion damage, a platinum line was deposited on the surface before the FIB milling. The lamellae were prepared using standard preparation steps with a last cleaning step of low energy (5 kV) to reduce the ion beam damage. In one lamella denoted further as L1, the heterostructure was free standing, disconnected from the substrate, in order to remove the stress induced by the Si substrate. In the second lamella denoted further as L2, the heterostructure was firmly connected to the substrate and therefore it was supposed that the uniaxial stress component induced by the substrate along the lamella interface, the stress of the first order, was still preserved. PED patterns were acquired using a Zeiss Libra 200 FE TEM operating at 200 kV and equipped with a NanoMEGAS DigiStar precession device controlled by Topspin Strain Measurement software. For this investigation the TEM was set to STEM mode with a camera length of 180 mm and the precession angle was set to 1.02°. The condenser lens setting with a condenser aperture of 5 µm enabled a quasi-parallel nanobeam with a convergent angle of 1 mrad and a probe size of 1.5 nm. For the strain mapping the lamella L2 was scanned over a predefined area and the diffraction patterns were recorded by using an external ultrafast CCD camera mounted in front of the TEM screen. The spatial resolution was limited by the step size which was set to 2 nm for the series scans. The unstrained reference patterns were acquired from the relaxed surface region of the lamella L2. For a comparison, unstrained patterns were collected also form

the (unstrained) lamella L1 providing very similar results as the calibration patterns obtained from the lamella L2.

The PED patterns were analysed with the Topspin Strain Measurement software to determine the variation in the lattice parameter at each depth in the heterostructure [21]. The data were used to evaluate the variation in the ratio between lattice parameters *c* and *a* of the hexagonal sublayers within the heterostructure. The experimentally obtained ratio depth profile $c(z)/a(z)$ was then compared with tabulated values c_o/a_o of unstressed lattice parameters of the respective materials from the literature.

A.3 Results

In Figure A.3., XRD pattern obtained from the heteroepitaxial structure is presented. Besides the substrate (111) reflection, there are (0002) reflections from $Al_xGa_{1-x}N$ sublayers visible. The diffraction data document the growth of the hexagonal sublayers with (0001) crystallographic planes approximately parallel to the substrate (111) plane. Unfortunately, a diffraction signal from the top 20 nm thick $Al_{0.22}Ga_{0.78}N$ sublayer (Figure A.1.) is in Figure A.3. not visible.

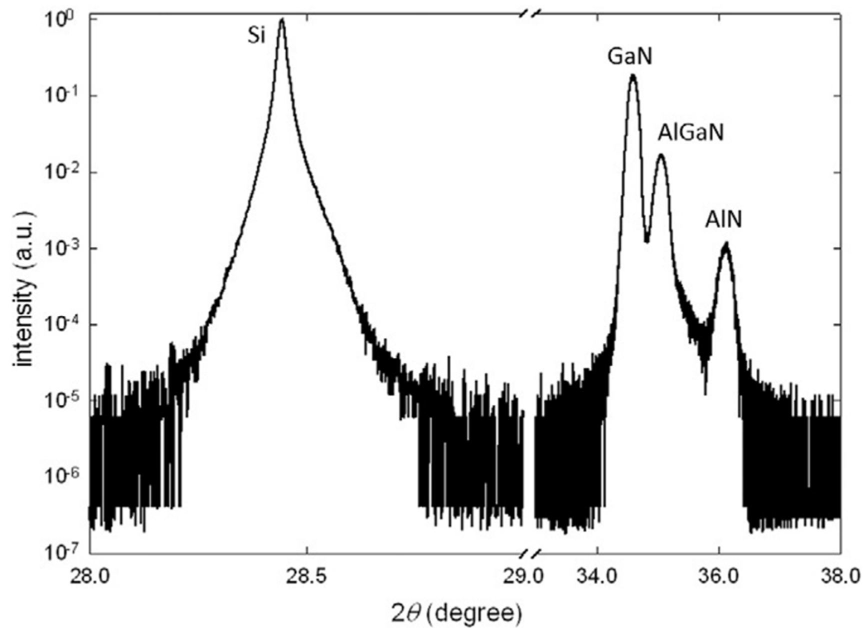

Figure A.3.: XRD pattern collected from the heteroepitaxial structure with 111 peak of Si and 0002 peaks of GaN, $Al_{0.25}Ga_{0.75}N$ and AlN detected at 2θ positions of 28.443, 35.057, 35.599 and 36.1185 with FWHMs of 0.025, 0.159, 0.219 and 0.214, respectively.

In Figure A.4., cantilever deflections δ after the individual milling steps are presented as a function of the remaining heterostructure thickness (Figure A.2b). The complex δ dependence can be at this stage qualitatively interpreted by a presence of a non-linear residual stress distribution within the film. The two deflection maxima in $Al_{0.25}Ga_{0.75}N$ and GaN at ~250 and ~800 nm in Figure A.4. document the presence of pronounced stress changes as a function of film depth $\partial\sigma(z)/\partial z$ in these sublayers.

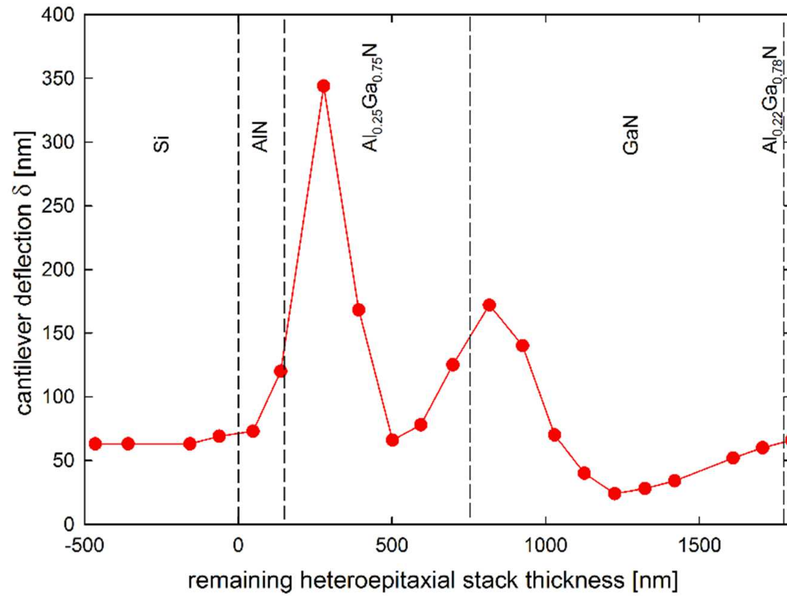

Figure A.4.: The measured deflection δ of the free standing microcantilever determined during the incremental FIB milling experiments (Figure A.2.) as a function of the remaining heterostructure thickness indicates a nonlinear variation of the stress state. The nonzero cantilever deflection at ~$\delta(0)$ corresponds to the stress free state in the film.

The deflection data from Figure A.4. were used to calculate the residual stress distribution within the structure using the FEM algorithm. In Figure A.5., the evaluated cross-sectional stress distribution in the heterostructure is presented. The stress profile $\sigma(z)$ documents a relatively high tensile stress of ~1.5 GPa in the interface AlN sublayer which changes to high compressive stress state of ~1 GPa in $Al_{0.25}Ga_{0.75}N$. Interestingly, residual stresses change from compressive to tensile in both $Al_{0.25}Ga_{0.75}N$ and GaN sublayers. At the heterostructure surface the stress practically vanishes. A comparison of the data from Figures A.4. and A.5. documents that the two pronounced peaks in $\delta(z)$ in Figure A.4. correspond to abrupt stress changes at interfaces between AlN/$Al_{0.25}Ga_{0.75}N$ and $Al_{0.25}Ga_{0.75}N$/GaN. Also the valley between the two peaks in Figure A.4. corresponds to the compressive-to-tensile stress transition within $Al_{0.25}Ga_{0.75}N$ sublayer.

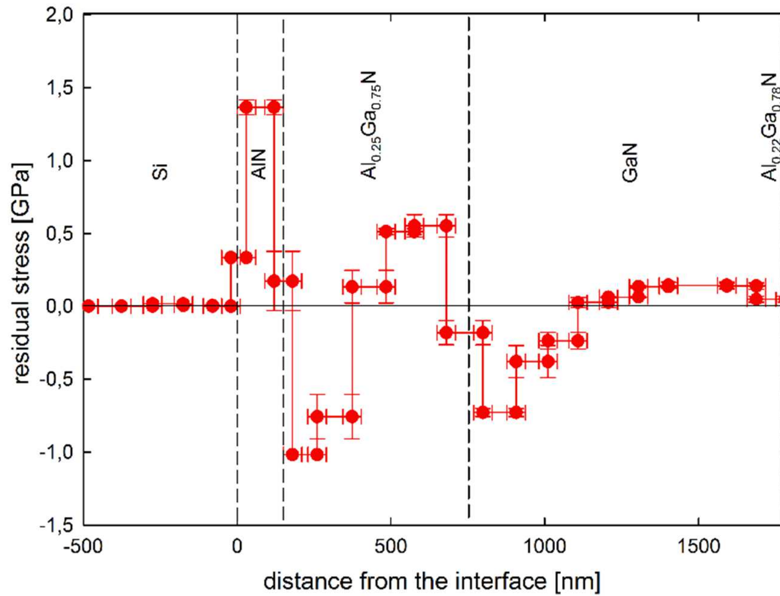

Figure A.5.: Cross-sectional stress distribution of residual stresses in $Al_xGa_{1-x}N$ heterostructure on Si(111) evaluated using FEM documents a presence of relatively high tensile and compressive stress concentrations. The stepwise form of the stress profile originates from the applied FIB milling depth steps of ~100 nm (Figure A.2b).

As already mentioned, position-resolved precession electron diffraction was used to evaluate $c(z)/a(z)$ as a function of the heterostructure depth. The data presented in Figure A.6. are compared with the literature values of GaN and AlN unstressed lattice parameter ratios c_o/a_o [31]. For $Al_xGa_{1-x}N$ sublayers, the ratios were calculated using Vegard's law. In the case of uniaxial stressed TEM lamella, tensile and compressive stresses would induce elastic crystal lattice deformation with $c(z)/a(z)$ ratios smaller and larger than the values of c_o/a_o.

In Figure A.7., a cross-sectional TEM micrograph of the heterostructure is shown. The micrograph shows a relatively high concentration of structural defects in the interface AlN sublayer as well as in the $Al_{0.25}Ga_{0.75}N$ and GaN sublayers next to AlN and $Al_{0.25}Ga_{0.75}N$ sublayers, respectively. The gradients of the defect density across the $Al_{0.25}Ga_{0.75}N$ and GaN sublayers indicate a continuous improvement of their crystallographic quality and were used to interpret the stress data from Figure A.5.

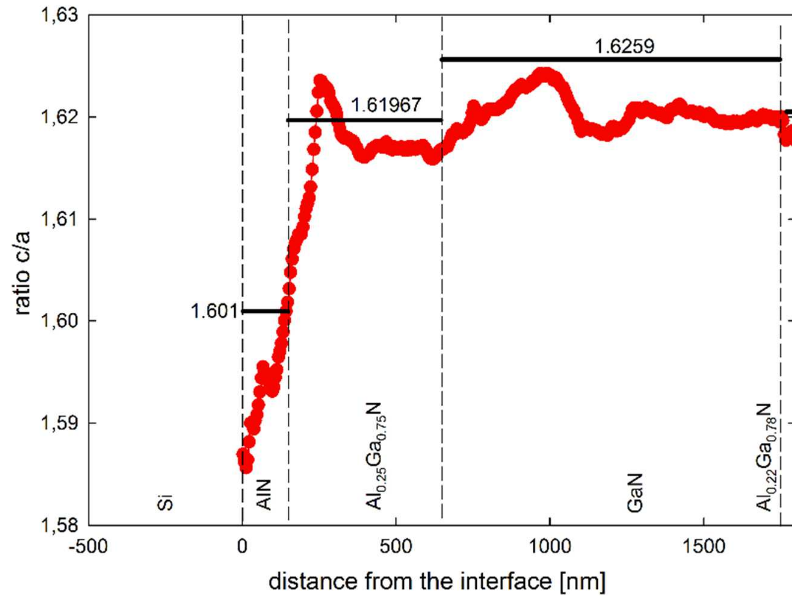

Figure A.6.: Cross-sectional dependence of the lattice parameter ratio *c(z)/a(z)* determined using PED. Bold vertical lines represents magnitudes of unstressed lattice parameter ratios c_o/a_o of the individual sublayer materials [31]. Experimental points lying above and below those lines are expected to represent heterostructure regions under compression and tension, respectively.

A.4 Discussion

Residual stress profile from Figure A.5. obtained using the ILR method was qualitatively confirmed by the PED experiment. High tensile stress within the AlN sublayer shown in Figure A.5., which decreases towards the AlN/$Al_{0.25}Ga_{0.75}N$ interface, is in reasonable agreement with the *c(z)/a(z)* values from Figure A.6. Also the stress dependence in the $Al_{0.25}Ga_{0.75}N$ sublayer with a compressive-to-tensile stress transition (Figure A.5.) correlates relatively well with the *c(z)/a(z)* behaviour from Figure A.6., where also a stress reversal was observed. The ILR results for the GaN sublayer from Figure A.5. indicate a presence of compressive stress, which decreases towards the surface, becomes tensile and then practically vanishes. This behaviour was unfortunately not fully confirmed by the *c(z)/a(z)* dependence in Figure A.6.,where the stress state remained always tensile within

GaN. This discrepancy could be interpreted e.g. by the used incorrect c_o/a_o ratio in Figure A.6. and/or by a very probable partial stress relaxation in the surface region of the TEM lamella. In general, however, the results from Figure A.6. confirm, at least qualitatively, the stress-depth dependence obtained using the ILR method.

XRD data from Figure A.3. were used to evaluate the out-of-plane lattice spacing c of 0.49697 and 0.51152 nm for AlN and GaN sublayers, respectively. The experimental values appear smaller than the literature values of the AlN and GaN lattice parameters c of 0.4982 and 0.5186 nm from Ref. [32]. Therefore the XRD results from Figure A.3. indicate the presence of tensile stresses in the nitride sublayers, in agreement with the PED data from Figure A.6. Similarly, also the tensile stresses evaluated using the ILR method in the AlN sublayer (Figure A.5.) are qualitatively in agreement with the XRD results from Figure A.3. The oscillatory stress profile with the near zero sum of the stresses in the GaN sublayer (Figure A.5.), however, disagrees with the XRD data (Figure A.3.). Possible explanations could be an uncertainty in the stress magnitude of the GaN sublayer surface region determined using the ILR method (Figure A.5.) and/or a stronger contribution of the tensely-stressed GaN sublayer near-surface region (cf. Figure A.5.) to the XRD signal in Figure A.3.

A.4 Discussion

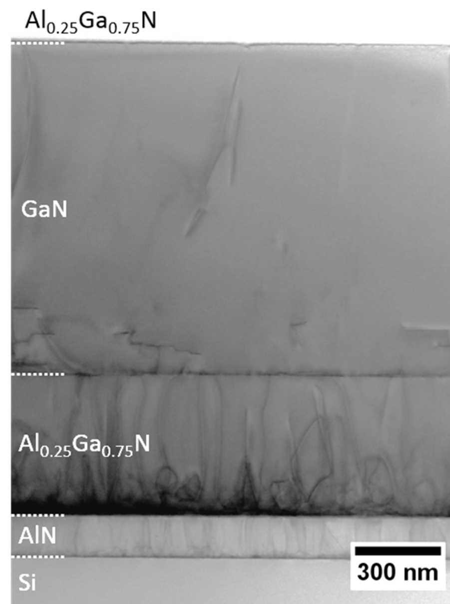

Figure A.7.: Cross-sectional TEM lamella from the heterostructure indicates a relatively high density of structural defects in the AlN sublayer as well as gradients of the defect density in the $Al_{0.25}Ga_{0.75}N$ and GaN sublayers.

The data from Figure 6.A. indicate a very complex stress profile within the heteroepitaxial structure. The AlN interface layer (Figure A.1.) is standardly used to improve the crystalline quality and to reduce tensile stresses in subsequent $Al_xGa_{1-x}N$ sublayers [11, 12, 33]. The high tensile stress up to 1.5 GPa observed in this sublayer can be interpreted as being caused by a large lattice and CTEs mismatches between AlN and Si [3, 4]. The layer can obviously accommodate very large tensile stresses. This ability can be interpreted by the presence of nanometer-sized crystalline domains within AlN sublayer (Figure A.7.). According to Blasing et al. [11], the AlN layer deteriorates the coherence between subsequent layers and the underlying substrate, which subsequently results in lower stresses and better crystallographic quality of subsequent sublayers. The presence of relative high compressive stresses in $Al_{0.25}Ga_{0.75}N$ and GaN sublayers at the interfaces to AlN and $Al_{0.25}Ga_{0.75}N$ can be interpreted by the smaller lattice constants of AlN and $Al_{0.25}Ga_{0.75}N$ with respect to the subsequent sublayers, respectively. The stress transition

from compressive to tensile within the $Al_{0.25}Ga_{0.75}N$ and GaN sublayers can be explained by changes in the growth modes from the nucleation, three-dimensional growth and subsequent lateral overgrowth to coalescence [34, 35, 36]. This is in agreement with the changes in the defect density gradients across the $Al_{0.25}Ga_{0.75}N$ and GaN sublayers visible in Figure A.7. Finally, in the top $Al_{0.22}Ga_{0.78}N$ sublayer, the tensile stress is relatively low (Figure A.5.), resulting in nearly equilibrium physical properties without the stress influence.

The stress profile from Figure A.6. can also be discussed from the point of view mechanical stability of the structure. The tensile stress concentrations are obviously very unfavourable for the fracture toughness of the heterostructure. The cracks can be initiated especially at the interface between the AlN sublayer and Si substrate and propagate along the interface to release the tensile stress. Though the tensile stress magnitudes in the $Al_{0.25}Ga_{0.75}N$ and GaN sublayers are significantly smaller than the tensile stress state in AlN, the actual tensile strength of the $Al_{0.25}Ga_{0.75}N$ and GaN ceramic sublayers is expected to be significantly smaller than that of AlN with nanometer-sized crystalline domains (Figure A.7.). Therefore also tensile stresses in $Al_{0.25}Ga_{0.75}N$ and GaN sublayers can represent a serious reliability issue.

A.5 Conclusion

The ILR method was used to determine the cross-sectional residual stress profile across the $AlN/Al_{0.25}Ga_{0.75}N/GaN/Al_{0.22}Ga_{0.78}N$ heterostructure on Si(111). A FEM was used to quantify the actual stress depth profile by using the microcantilever deflection data obtained during sequential FIB heterostructure milling. The results indicate very complex stress dependence with a large tensile stress of 1.5 GPa in the AlN sublayer, compressive-to-tensile stress transition within the $Al_{0.25}Ga_{0.75}N$ and GaN sublayers and relative low tensile stress below 100 MPa in the top $Al_{0.22}Ga_{0.78}N$ sublayer. The stresses were correlated with the lattice and CTE mismatches as well as with the variation of the sublayer growth modes. Complementary, precession TEM was used to determine the cross-sectional variation of

the lattice parameters *c(z)*/*a(z)*, which qualitatively confirms the stress-depth variation determined by the ILR method.

Supplementary data to this article can be found online at: http://dx.doi.org/10.1016/j.matdes.2016.06.001.

Acknowledgment

This work was jointly funded by the Austrian Research Promotion Agency (FFG Grant No. 854247) and the Carinthian Economic Promotion Fund (KWF Grant No. KWF-1521/28101/40388). The stress characterization of the heterostructure has received research funding from the European Union, within the large collaborative project ISTRESS, Grant Agreement No. 604646. Financial support by the Austrian Federal Government (in particular from the Bundesministerium für Verkehr, Innovation und Technologie and Bundesministerium für Wissenschaft, Forschung und Wirtschaft) represented by Österreichische Forschungs-förderungsgesellschaft mbH and the Styrian and the Tyrolean Provincial Government, represented by Steirische Wirtschaftsförderungsgesellschaft mbH and Standortagentur Tirol, within the framework of the COMET Funding Programme is gratefully acknowledged.

References

[1] W.A. Hadi, M.S. Shur, S.K. O'Leary, Steady-state and transient electron transport within the wide energy gap compound semiconductors gallium nitride and zinc oxide: an updated and critical review, *J. Mater. Sci. Mater. Electron.* **25** (2014) 4675–4713, http://dx.doi.org/10.1007/s10854-014-2226-2.

[2] B. Leung, J. Han, Q. Sun, Strain relaxation and dislocation reduction in AlGaN stepgraded buffer for crack-free GaN on Si(111), *Phys. Status Solidi* **11** (2014) 437–441, http://dx.doi.org/10.1002/pssc.201300690.

[3] A. Dadgar, J. Bläsing, A. Diez, A. Alam, M. Heuken, A. Krost, Metalorganic chemical vapor phase epitaxy of crack-free GaN on Si(111) exceeding 1 µm in thickness, *Jpn. J. Appl. Phys.* **39** (2000) L1183–L1185, http://dx.doi.org/10.1143/JJAP.39.L1183.

[4] J.A. del Alamo, J. Joh, GaN HEMT reliability, *Microelectron. Reliab.* **49** (2009) 1200–1206.

[5] F. Scholz, Semipolar GaN grown on foreign substrates: a review, *Semicond. Sci. Technol.* **27** (2012) 024002.

[6] D.G. Zhao, S.J. Xu, M.H. Xie, S.Y. Tong, H. Yang, Stress and its effect on optical properties of GaN epilayers grown on Si(111), 6H-SiC(0001), and c-plane sapphire, *Appl. Phys. Lett.* **83** (2003) 677–679.

[7] B. Zhang, Y. Liu, A review of GaN-based optoelectronic devices on silicon substrate, *Chin. Sci. Bull.* **59** (2014) 1251–1275.

[8] E. Feltin, B. Beaumont,M. Laügt, P. deMierry, P. Vennéguès, H. Lahrèche, et al., Stress control in GaN grown on silicon (111) by metalorganic vapor phase epitaxy, *Appl. Phys. Lett.* **79** (2001) 3230, http://dx.doi.org/10.1063/1.1415043.

[9] A. Dadgar, M. Poschenrieder, J. Bläsing, K. Fehse, A. Diez, A. Krost, Thick, crack-free blue light-emitting diodes on Si(111) using low-temperature AlN interlayers and in situ Si_xN_y masking, *Appl. Phys. Lett.* **80** (2002) 3670–3672.

[10] A. Watanabe, T. Takeuchi, K. Hirosawa, H. Amano, K. Hiramatsu, I. Akasaki, The growth of single crystalline GaN on a Si substrate using AIN as an intermediate layer, *J. Cryst. Growth* **128** (1993) 391–396.

[11] J. Bläsing, A. Reiher, A. Dadgar, A. Diez, A. Krost, The origin of stress reduction by low-temperature AlN interlayers, *Appl. Phys. Lett.* **81** (2002) 2722–2724.

[12] A. Krost, A. Dadgar, J. Bläsing, A. Diez, T. Hempel, S. Petzold, et al., Evolution of stress in GaN heteroepitaxy on AIN/Si(111): from hydrostatic compressive to biaxial tensile, *Appl. Phys. Lett.* **85** (2004) 3441–3443.

[13] S. Tripathy, S.J. Chua, P. Chen, Z.L. Miao, Micro-Raman investigation of strain in GaN and $Al_xGa_{1-x}N$/GaN heterostructures grown on Si(111), *J. Appl. Phys.* **92** (2002) 3503–3510.

[14] M.Wei, X.Wang, X. Pan, H. Xiao, C.Wang, C. Yang, et al., Effect of high temperature AlGaN buffer thickness on GaN Epilayer grown on Si(111) substrates, *J. Mater. Sci. Mater. Electron.* **22** (2011) 1028–1032.

[15] G. Meneghesso, G. Verzellesi, F. Danesin, F. Rampazzo, F. Zanon, A. Tazzoli, et al., Reliability of GaN high-electron-mobility transistors: state of the art and perspectives, *IEEE Trans. Device Mater. Reliab.* **8** (2008) 332–343.

[16] S.Massl, J. Keckes, R. Pippan, A directmethod of determining complex depth profiles of residual stresses in thin films on a nanoscale, *Acta Mater.* **55** (2007) 4835–4844, http://dx.doi.org/10.1016/j.actamat.2007.05.002.

[17] S. Massl, J. Keckes, R. Pippan, A newcantilever technique reveals spatial distributions of residual stresses in near-surface structures, *Scr. Mater.* **59** (2008) 503–506.

[18] S.Massl, H. Köstenbauer, J. Keckes, R. Pippan, Stressmeasurement in thin films with the ion beam layer removal method: influence of experimental errors and parameters, *Thin Solid Films* **516** (2008) 8655–8662.

[19] R. Schöngrundner, R. Treml, T. Antretter, D. Kozic,W. Ecker, D. Kiener, et al., Critica assessment of the determination of residual stress profiles in thin films by means of the ion beam layer removal method, *Thin Solid Films* **564** (2014) 321–330.

[20] R. Treml, D. Kozic, J. Zechner, X. Maeder, B. Sartory, H.-P. Gänser, et al., High resolution determination of local residual stress gradients in single- and multilayer thin film systems, *Acta Mater.* **103** (2016) 616–623, http://dx.doi.org/10.1016/j.actamat.2015.10.044.

[21] A.D. Darbal, R.D. Narayan, C. Vartuli, G. Lian, R. Graham, F. Shaapur, et al., Automated high precision strain measurement using nanobeam diffraction coupled with precession, *Microsc. Microanal.* **19** (2013) 702–703, http://dx.doi.org/10.1017/S1431927613005503.

[22] A.D. Darbal, R.D. Narayan, C. Vartuli, T. Aoki, J. Mardinly, S. Nicolopoulos, et al., Applications of automated high resolution strain mapping in TEM on the study of strain distribution in MOSFETs, *Microsc. Microanal.* **20** (2014) 1066–1067, http://dx.doi.org/10.1017/S1431927614007053.

[23] J.K. Weiss, A.D. Darbal, R.D. Narayan, S.T. Kim, S. Nicolopoulos, System and process for measuring strain in materials at high spatial resolution, *US patent* **US9274070 B2**, 2016 March 1.

[24] D. Cooper, N. Bernier, J.-L. Rouvière, Combining 2 nm spatial resolution and 0.02% precision for deformation mapping of semiconductor specimens in a transmission electron microscope by precession electron diffraction, *Nano Lett.* **15** (2015) 5289–5294, http://dx.doi.org/10.1021/acs.nanolett.5b01614.

[25] K. Levenberg, A method for the solution of certain problems in least squares, *Quart. Appl. Math.* (1944), pp. 164–168.

[26] D.W. Marquardt, An algorithm for least-squares estimation of nonlinear parameters, *J. Soc. Ind. Appl. Math.* **11** (1963) 431–441.

[27] L. Margulies, G.Winther, H.F. Poulsen, In situ measurement of grain rotation during deformation of polycrystals, *Science* **291** (2001) 2392–2394, http://dx.doi.org/10.1126/science.1057956.

[28] A. Polian, M. Grimsditch, I. Grzegory, Elastic constants of gallium nitride, *J. Appl. Phys.* **79** (1996) 3343–3344.

[29] J.J.Wortman, R.A. Evans, Young'smodulus, shear modulus, and poisson's ratio in silicon and germanium, *J. Appl. Phys.* **36** (1965) 153–156.

[30] A.F.Wright, Elastic properties of zinc-blende and wurtzite AlN, GaN, and InN, *J. Appl. Phys.* **82** (1997) 2833, http://dx.doi.org/10.1063/1.366114.

[31] Y. Fu, Z. Li, W.T. Ng, J.K.O. Sin, Integrated Power Devices and TCAD Simulation, *CRC Press*, (2014).

[32] S. Pearton (Ed.), *GaN and ZnO-Based Materials and Devices*, Springer, Berlin Heidelberg, Berlin, Heidelberg, (2012) http://dx.doi.org/10.1007/978-3-642-23521-4.

[33] S. Raghavan, J.M. Redwing, Growth stresses and cracking in GaN films on (111) Si grown by metal-organic chemical-vapor deposition. I. AlN buffer layers, *J. Appl. Phys*. **98** (2005).

[34] H. Amano, I. Akasaki, K. Hiramatsu, N. Koide, N. Sawaki, Effects of the buffer layer in metalorganic vapour phase epitaxy of GaN on sapphire substrate, *Thin Solid Films* **163** (1988) 415–420.

[35] S. Figge, T. Böttcher, S. Einfeldt, D. Hommel, In situ and ex situ evaluation of the film coalescence for GaN growth on GaN nucleation layers, *J. Cryst. Growth* **221** (2000) 262–266, http://dx.doi.org/10.1016/S0022-0248(00)00696-5.

[36] T. Szymański, M.Wośko, B. Paszkiewicz, R. Paszkiewicz,M. Drzik, Stress engineering in GaN structures grown on Si(111) substrates by SiN masking layer application, *J. Vac. Sci. Technol. A Vacuum, Surfaces, Film* **33** (2015) 041506, http://dx.doi.org/10.1116/1.4921581.

Resolving alternating stress gradients and dislocation densities across $Al_xGa_{1-x}N$ multi-layer structures on Si(111)

M. Reisinger [a], M. Tomberger [b], J. Zechner [c], I. Daumiller [b], B. Sartory [e], W. Ecker [e], J. Keckes [a], R.T. Lechner [d]

[a] Department of Materials Physics, Montanuniversitaet Leoben, Franz Josef-Straße 18, 8700 Leoben, Austria

[b] Infineon Technologies Austria AG, Siemensstraße 2, 9500 Villach, Austria

[c] KAI Kompetenzzentrum Automobil- u. Industrieelektronik GmbH, Europastraße 8, 9524 Villach, Austria

[d] Institute of Physics, Montanuniversität Leoben, Montanuniversitaet Leoben, Franz Josef-Straße 18, 8700 Leoben, Austria

[e] Materials Center Leoben Forschung GmbH, Roseggerstraße 12, 8700 Leoben, Austria

Abstract

Gradients of residual stresses and crystal qualities across a 2 µm thick AlN/$Al_{0.32}Ga_{0.68}N$/GaN/$Al_{0.17}Ga_{0.83}N$ multilayer stack deposited on Si(111) were evaluated by combining following techniques: High-resolution X-ray diffraction (XRD), scanning transmission electron microscopy (STEM), high resolution transmission electron microscopy (HR-TEM) and ion beam layer removal method (ILR) with 100 nm depth resolution. ILR reveals the alternating stress profiles, which are related to sublayer dislocation-density gradients. The laboratory XRD confirms the derived mean stress

values, the presence of stress gradients within the sublayers and decreasing average sublayer threading dislocations-densities across the heterostructure. Additionally, the decreasing dislocation-densities within the individual sublayers are visualized by STEM. The documented stepwise improved crystal quality enables the formation of a highly tensile stressed 20 nm thick $Al_{0.17}Ga_{0.83}N$ top barrier-layer resulting in a pseudomorphic $GaN/Al_{0.17}Ga_{0.83}N$ interface.

B.1 Introduction

In the last decades, there has been an intensive research to grow high quality GaN and related semiconductors on Si substrates. The remarkable electrical and optical properties of GaN related materials give them a great potential for the application in optoelectronic and high power-high frequency devices, such as LEDs and high-electron-mobility-transistors (HEMT).[1] However the main obstacles for the utilization of Si as a substrate material are the large mismatches in lattice constants (~17%) and in the coefficients-of-thermal-expansion (CTEs) between GaN and Si (~56%).[2]

Therefore, dedicated sublayer systems based on AlN and $Al_xGa_{1-x}N$ have been used to counterbalance the strain caused by the thermal and lattice mismatch between GaN and Si. Generally, such a HEMT structure consists of a nucleation layer, a transition layer, a GaN buffer layer and a barrier-layer on the top. Within a few monolayer narrow active region at the buffer-barrier interface the two-dimensional electron gas channel (2DEG) is generated, which is crucial for many electronical applications.[3]

Hence, the overall crystal quality as well as the residual strain evaluation are important prerequisites for the development of suitable $Al_xGa_{1-x}N$ heterostructures. As a consequence various characterization techniques have been adapted to assess these parameters: (i) X-ray diffraction (XRD)[4,5], (ii) Raman spectroscopy[5–7], (iii) focus-ion-beam combined with digital-image-correlation (FIB-DIC)[8,9], (iv) wafer bow[10,11] and (v) transmission electron microscopy (TEM).[12,13]

In semiconductor industry high-resolution X-ray diffraction (XRD) and reciprocal space mapping (RSM) are well established methods for the evaluation of residual strain and

crystal quality. The analysis of the RSMs allows to gain structural information on the individual sublayers, like lattice spacing and hence strain/stress values, as well as dislocation-densities.[4,14]

Since the laboratory XRD and RSM characterization of semiconductor heterostructures is carried out usually in reflection geometry, it is not trivial to evaluate the strain and microstructural gradients within the individual sublayers. The diffracted signal provides usually average information across the depth of individual sublayers.

In our previous work, we have revealed residual stress gradients across an $Al_xGa_{1-x}N$ heterostructure with 100 nm depth resolution by using the ion beam layer removal method (ILR), whereby stress values were determined by analyzing deflections of FIB machined cantilevers (*cf.* Ref. 8). The aim of the present work is (i) to quantitatively and qualitatively compare results from XRD, ILR and TEM methods, which were used to analyze gradients of strains and dislocation-densities within individual sublayers of the same heterostructure as well as (ii) to discuss limitations of the individual techniques.

B.2 Experiments

The studied heterostructures, which consist of a Si(111) substrate, a 150 nm AlN nucleation layer, a 500 nm $Al_{0.32}Ga_{0.68}N$ transition layer, a 1.13 µm GaN buffer layer, and a 20 nm thin $Al_{0.17}Ga_{0.83}N$ top barrier-layer was grown by using a metal-organic-chemical-vapor-deposition (MOCVD) process (*cf.* Figure B.1.).[8] Due to process-related temperature and reactor pressure variations on lateral different wafer locations, the composition of the $Al_xGa_{1-x}N$ layer may alter form center to edge in the range of $\Delta x = 0.02$.[15] The exact $Al_xGa_{1-x}N$ layer compositions of the investigated samples were characterized via XRD. $Al_xGa_{1-x}N$ heterostructure grows on the Si substrate with (001) $Al_xGa_{1-x}N$ ∥ (111) Si and (110) $Al_xGa_{1-x}N$ ∥ $(\bar{1}10)$ Si. In total we have prepared and analyzed four samples (denoted as A-D), which are based on the described heterostructure.[8] While sample A only consists of the AlN nucleation layer, each subsequent sample consists of one additional layer until the entire heterostructure stack is completed in sample D (*cf.* Figure B.1.).

The XRD was carried out using a Rigaku SmartLab 5 circle diffractometer in high resolution setup.[16] In order to distinguish between composition and strain gradients, RSMs were collected around the symmetric (002), (004) and (006) reciprocal-lattice-points (RLP) as well as around the asymmetric (114) and (105) RLPs in coplanar geometry. In non-coplanar geometry the (100), (200) and (300) reflections were recorded using grazing incidence diffraction (GID) with a constant incident and diffraction angles of 0.5°.[4,17] Due to the low incident angle, the penetration depth of the AlN and GaN layer is limited to ~688 nm and ~207 nm, respectively[17]. Hence, the in-plane AlN, $Al_{0.32}Ga_{0.68}N$ and GaN reflections were recorded from topmost-layers of samples A, B and C, respectively.

Figure B.1. displays the symmetric $Al_xGa_{1-x}N$ (002) RSM of the sample D with all four sublayers. All reciprocal-lattice-points (RLP) are marked with green stars and correspond to the labelled AlN, $Al_{0.32}Ga_{0.68}N$, GaN sublayers and the Si substrate. Consequently the 20 nm thick $Al_{0.17}Ga_{0.83}N$ barrier-layer is the only sublayer, which signal is not visible in this RSM. Owing to the small diffraction volume of the $Al_{0.17}Ga_{0.83}N$ barrier-layer and the small distance to the $Al_{0.32}Ga_{0.68}N$ RLP, the rather weak RLP is covered by the strong $Al_{0.32}Ga_{0.68}N$ reflection. In the symmetric RSM, the $Al_{0.32}Ga_{0.68}N$ and GaN RLP shapes are affected by an out-of-plane lattice-spacing variation, which causes peak broadening parallel to q_z, the out-of-plane scattering vector.

B.3 Results and Discussion

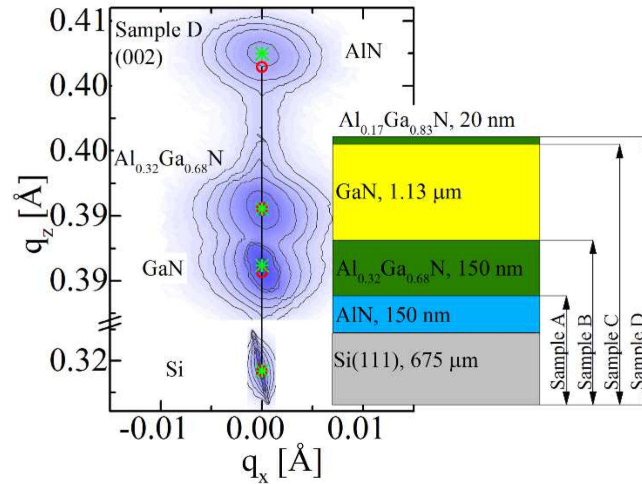

Figure B.1.: RSM collected around $Al_xGa_{1-x}N$ (002) and Si (111) reflections of sample D, where q_x and q_z correspond to the in-plane and out-of-plane scattering vector, respectively. The scale break on the q_z-axis should be noted. The inset shows schematically the entire heterostructure.

In order to evaluate the origin of the lattice-spacing variations, asymmetric $Al_xGa_{1-x}N$ (114) RSMs from samples C and D were recorded (see Figures B.2a-b). The reflections originate from the AlN, $Al_{0.32}Ga_{0.68}N$ and GaN sublayers. In Figure B.2b an additional maximum close to the $Al_{0.32}Ga_{0.68}N$ reflection is visible. Since this maximum is not present in sample C, this peak can be attributed to the 20 nm thick $Al_{0.17}Ga_{0.83}N$ barrier-layer. The peak position was determined by the horizontal and vertical intensity-line-profiles parallel to the q_x and q_z-axis, corresponding to the in-plane and out-of-plane scattering vectors (see Figures. B.2c-d).

The sublayer lattice constants a_{exp} and c_{exp} were evaluated from the q_x and q_z-values of the peak positions in the RSMs using equation B-S1. according to Ref.18. Subsequently, a_{exp} and c_{exp} were used to calculate the sublayer strain values via equations B-S2 and B-S3 using the unstrained reference lattice constants a_0 and c_0 (see “supplementary material”). The AlN and GaN references were taken from literature[4], whereas the $Al_xGa_{1-x}N$ values

were determined using Vegard's law.[5] In order to visualize strain in the RSMs, the unstrained reference values of the AlN (a_0 = 3.112 Å, c_0 = 4.981 Å), $Al_{0.32}Ga_{0.68}N$ (a_0 = 3.162 Å, c_0 = 5.120 Å), GaN (a_0 = 3.186 Å, c_0 = 5.186 Å) and $Al_{0.17}Ga_{0.83}N$ (a_0 = 3.173 Å, c_0 = 5.151 Å) sublayers were converted into the reciprocal space coordinates (q_x, q_z) and indicated with red circles.[4] These coordinates form the composition line, which is the strain free basis within the asymmetric RSM (Figure B.2.), and all RLPs to the left and to the right of the line are shifted by in-plane tensile and compressive strains, respectively. Subsequently the mean in-plane strain of the individual sublayers were converted into in-plane stress (σ_{xx}), by $\sigma_{xx} = \varepsilon_{xx}\ ((c_{11} + c_{12}) - 2\ c_{13}^2/c_{33})$, where c_{11}, c_{12}, c_{13} and c_{33} are the elastic constants of the $Al_xGa_{1-x}N$ sublayer, which are linearly interpolated by using data from GaN and AlN.[19,20]

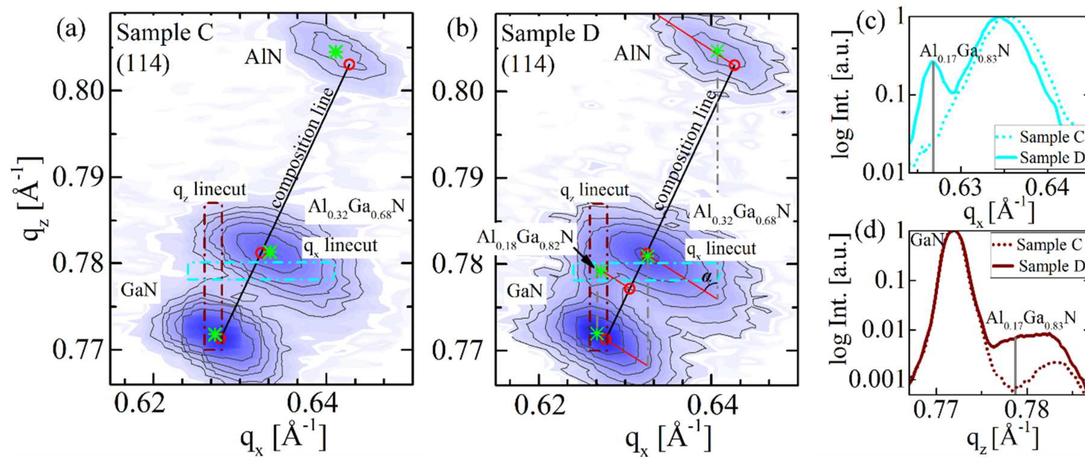

Figure B.2.: RSMs for $Al_xGa_{1-x}N$ (114) reflections of samples C (a) and D (b), where q_x and q_z correspond to the in-plane and out-of-plane scattering vectors, respectively. The (114) RLPs positions (green stars) and the theoretical deduced unstrained reference positions (red circles) from the individual sublayers are marked in every RSM. Additionally the relaxation lines (red lines) are displayed in (b). The integration area of the horizontal (q_x) and vertical (q_z) line cuts are marked with bright blue and brown rectangles, respectively. The normalized logarithmic intensity profile of the horizontal (c) and vertical (d) line scans reveal the position of the (114) reflection of the 20 nm thick $Al_{0.17}Ga_{0.83}N$ barrier-layer.

The red lines in Figure B.2b show the relaxation lines, which were determined according to the relationships provided in the supplementary material (Eq. B-S4. – B-S6.). The RLP position on the relaxation line is described via the relaxation parameter γ, which quantifies the strain induced relaxation according to equation B-S7. given in the supplementary material. Generally the relaxation lines are confined by the in-plane spacing of the previous layers (grey line), which represents the fully strained situation (γ = 1) and the strain free reference on the composition line (γ = 0) (Figure B.2b). The relaxation parameters of the AlN (γ = 0.012), $Al_{0.32}Ga_{0.68}N$ (γ = 0.09), GaN (γ = -0.08) and $Al_{0.17}Ga_{0.83}N$ (γ = 0.98) layers are the basis for the later discussion about the strain gradient evolution within the heterostructure.

The crystal quality evolution across the heterostructure was characterized by analyzing the dislocation-density. In $Al_xGa_{1-x}N$ structures, there exist mainly three types of threading dislocations (TDs), which have a common dislocation line direction $\langle 001 \rangle$ and diverse Burgers vectors *b*: edge dislocations with b = 1/3 $\langle 110 \rangle$; screw dislocations with b = $\langle 001 \rangle$; Mixed dislocations with b = $\langle 113 \rangle$.[21] Due to the distinguished Burgers vectors the crystal is differently distorted, where screw and edge TD causes crystal twist and tilt, respectively. Hence the impact of screw and edge TDs on the RLP width was separated by the collection of the in-plane (*h*00) and the out-of-plane (00*l*) reflections, which are only sensitive for crystal twist and tilt, respectively.[22] Since mixed dislocations contribute to both, the crystal tilt and twist, the total number of dislocations is usually overestimated.

The influence of instrumental broadening and the sample curvature were subtracted from the sublayer reflections by subtracting the width of different (hhh) and $(h\bar{h}0)$ reflections of the nearly perfect Si substrate. The additional correlation length broadening can be graphically separated from the pure dislocation broadening by using a Williamson-Hall-Plot (WH-Plot)[19] (for details see supplementary material).

The edge and screw TD-densities (N_E and N_S) as well as the determined lattice parameters (a_{exp}, c_{exp}), the in-plane strain and stress values (ε_{xx}, σ_{xx}) and the relaxation parameters (γ) of the individual sublayers within sample D are listed in Table B.1. The in-plane strain and stress values were deduced on basis of the lattice parameters, which

have been determined by averaging the experimental lattice parameters of all single asymmetric and symmetric RLPs.

	a_{exp} (Å)	c_{exp} (Å)	ε_{xx} (-)	σ_{xx} (GPa)	γ (-)	N_E (cm^{-2})	N_S (cm^{-2})
AlN	3.121	4.971	$2.89\text{x}10^{-3}$	1.465	0.012	$1.16\text{x}10^{11}$	$1.25\text{x}10^{10}$
$Al_{0.32}Ga_{0.68}N$	3.162	5.121	$-1.01\text{x}10^{-4}$	-0.049	0.09	$5.10\text{x}10^{10}$	$3.30\text{x}10^{9}$
GaN	3.189	5.182	$1.26\text{x}10^{-3}$	0.451	-0.08	$4.83\text{x}10^{10}$	$7.55\text{x}10^{8}$
$Al_{0.17}Ga_{0.83}N$	3.188	5.135	$1.03\text{x}10^{-3}$	2.830	0.98	-	-

Table B.1.: A comparison of the experimentally deduced sublayer lattice parameters (a_{exp}, c_{exp}), in-plane strain (ε_{xx}), in-plane stress (σ_{xx}), relaxation parameter (γ) and the edge and screw TD-densities (N_E, N_S). The listed lattice parameters a_{exp} and c_{exp} of the AlN, $Al_{0.32}Ga_{0.68}N$ and GaN layers are the average of the sublayer lattice parameter values determined by the evaluation of the (114), (105), (002), (004), (006), (100), (200), (300) RLPs, with standard deviations of 0.003 Å (a_{exp}) and 0.002 Å (c_{exp}).

In epitaxial structures residual strain is mainly caused by the lattice (epitaxial strain) and thermal mismatch (thermal strain). It is well known that epitaxial strain relaxation only occurs in structures, which exceed the critical thickness.[23] The critical thickness is usually in the range of a few nanometers. Holec *et al.* have calculated a critical thickness of 10 nm for edge dislocations in $Al_{0.17}Ga_{0.83}N$ deposited on GaN.[24] Consequently, a highly strained 20 nm $Al_{0.17}Ga_{0.83}N$ barrier-layer and a rather coherent GaN/$Al_{0.17}Ga_{0.83}N$ interface can be assumed.

Heinke *et. al.* have also considered the impact of thermal strain on the RLP positions within the RSMs.[25] Based on thermal mismatch, the heterostructure contracts more than the Si substrate and therefore tensile strain is generated within the entire heterostructure during cooling from the deposition-temperature to room-temperature. Hence the negative GaN relaxation parameter (γ = - 0.08) can be explained by thermal strain effects. Since the coefficients-of-thermal-expansion (CTEs) of $Al_xGa_{1-x}N$ structures decreases with the

increasing Ga content, the thermal mismatch between the individual sublayers determines the final strain state close to the interface at room-temperature. Consequently an inhomogeneous strain profile within the $Al_{0.32}Ga_{0.68}N$ layer is created by the introduction of compressive and tensile strain at the AlN and GaN interface regions, respectively.

Several reports have shown that TD based relaxation processes can also lead to inhomogeneous strain distribution within $Al_xGa_{1-x}N$ layers.[26–28] Romanov and Speck created a model, where the inclination of edge TDs is the main driving force for the evolution of strain gradients.[29]

Such strain gradients cannot be easily determined by using RSMs. However, in this study we have used the RLP asymmetries along the relaxation line as qualitative indicator for the presence of strain gradients.[30] The strain profiles across $Al_{0.32}Ga_{0.68}N$ and GaN sublayers consists of three main sections: (i) the initial compressive strain (initiated by larger lattice parameter of the subsequent sublayer), (ii) the tensile strain generation (decrease of compressive stress due to inclined dislocations), and (iii) the steady strain state. Such gradients would give rise to asymmetric peaks, where the less steep shoulder belongs to section (ii) and the steep peak shoulder to section (iii).

In order to evaluate the peak symmetry we introduce the asymmetry factor (A_f), which is the ratio of the left and the right peak width (A and B) at 10% of the full peak height, as shown in Figures B-S.2b-d (see “supplementary material” for details). Here $A_f > 1$ indicates a tailing peak and $A_f = 1$ a symmetric peak.[31] Consequently a value of 1 is related to a layer without strain gradient and values deviating from 1 indicate the presence of strain gradients. Based on the determined A_f values, the AlN layer ($A_f = 0.97$) has a rather homogeneous (or very dominant) tensile strain distribution, whereas significant strain gradients were revealed within the $Al_{0.32}Ga_{0.68}N$ and GaN sublayers ($A_f = 1.13$, $A_f = 1.12$).

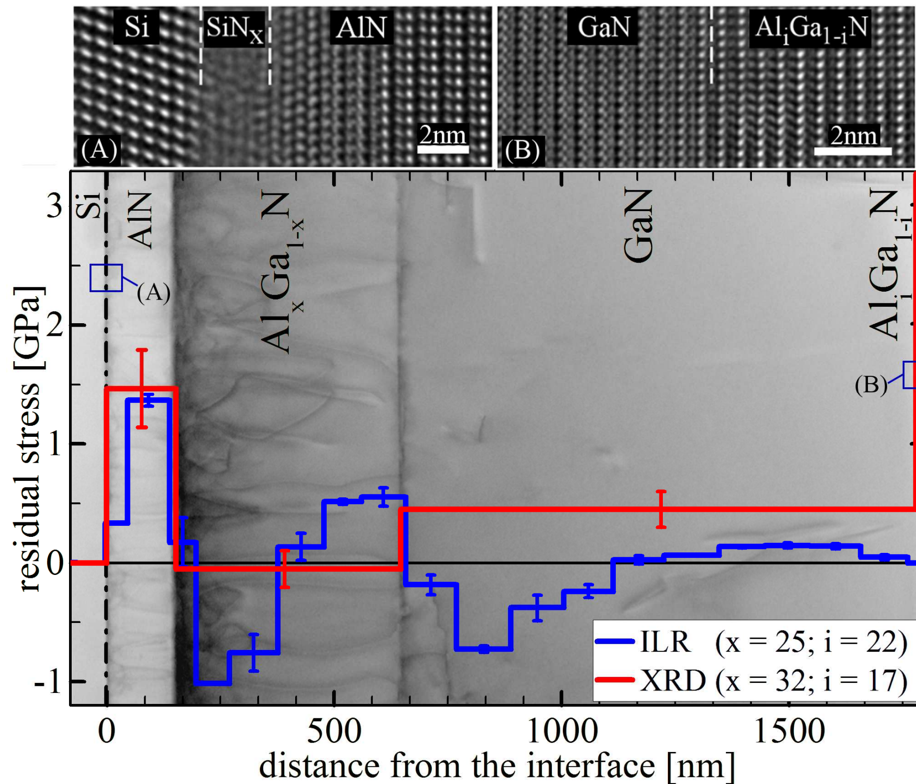

Figure B.3.: A comparison of average sublayer stresses (obtained using XRD) and individual sublayer stress gradients (evaluated using ILR) of two very similar HEMT structures, which vary in their composition of the $Al_xGa_{1-x}N$ transition and the $Al_iGa_{1-i}N$ barrier-layer. The ILR data were obtained with a spatial resolution of 100 nm. However, due to sample misalignment data points next to interfaces with steep stress transitions represent average stress values from interface region of both sublayers and underestimate the absolute stress value. The stress data correlate well with the microstructural features of the STEM cross-section image in the background. Filtered HRTEM images show the Si/AlN (inset A) and GaN/$Al_iGa_{1-i}N$ (inset B) interfaces of the heterostructure.

Finally we discuss the evolution of the individual sublayer strain gradients by comparing the data from the XRD analysis with the ILR stress profile and the microstructural cross-sectional STEM analysis all presented in Figure. B.3. Due to minor sample misalignment, data points next to interfaces with steep stress gradients (Si/AlN; AlN/$Al_xGa_{1-x}N$;

$Al_xGa_{1-x}N$/GaN) underestimate the absolute stress value (for details see supplementary material). The Z-contrast in the STEM image corresponds to the different sublayer material, whereas dark lines within the individual sublayer indicate regions with higher TD-densities. Consequently, contrast variations as a function of the distance from the interface display decreasing TD-density gradients within the sublayers along the growth direction. HRTEM images of the Si/AlN (Figure B.3. inset A) and the GaN/$Al_iGa_{1-i}N$ (Figure B.3. inset B) were used to show the interface coherence.

As listed in Table B.1., the AlN layer has a mean tensile stress of 1.465 GPa, which originates primarily from the large mismatch between AlN and Si. The HRTEM image in Figure B.3. reveals a 2 nm thick SiN_x layer at the Si/AlN interface. As reported in literature, this intermediate layer does not prohibit the epitaxial AlN growth [1]. The homogenous TD-density in the STEM image indicates, however, that the AlN layer is largely relaxed with respect to its initial in -plane Si lattice constant. This is reflected by the calculated relaxation parameter of $\gamma = 0.012$ (see Table B.1.). Based on the homogeneous dislocation distribution and the lack of TD inclination visible in the STEM image of Figure B.3., dislocation triggered strain gradients can be neglected, which are verified by the asymmetry parameter of $A_f = 0.97$ derived from the XRD peak profile analysis.

The subsequent $Al_{0.32}Ga_{0.68}N$ layer is expected to possess a larger lattice spacing than the previous AlN layer. Consequently the layer initially grows under compressive stress. Due to the inclination of edge TD, tensile stress is generated and causes a transition from compressive to tensile stress at a distance of 370 nm to the substrate revealed by ILR and a change in the TEM contrast, which corresponds to dislocation annihilation (see Figure B.3.). Consequently the tensile strain generation stops and the remaining layer grows under a steady stress level. Thus the mean residual stress value of the whole layer is close to zero as remarkably confirmed by RSM analysis (Figure B.3.). The strain gradient, however, is clearly revealed by a peak asymmetry A_f value of 1.13.

A similar strain evolution can be seen in the GaN layer. Since the GaN layer is thicker than the $Al_{0.32}Ga_{0.68}N$ layer, the rather steady tensile stress section above 1150 nm from the interface is dominant and a mean stress value of 0.451 GPa was measured via XRD (see Table B.1. and Figure B.3.). The single stress values from ILR averaged over the whole

layer thickness results, however, in values close to -0.077 GPa. This discrepancy can be explained by composition differences in the 500 nm thick $Al_xGa_{1-x}N$ transition layer of the ILR (x = 0.25) and XRD (x = 0.32) sample. Consequently the initial compressive stress in GaN layer of the XRD sample is higher, which results in a steeper gradient and thus a higher steady tensile stress state.[32]

Based on the only 20 nm thickness and the high relaxation parameter $\gamma = 0.98$, a nearly fully strained, pseudomorphic $Al_{0.17}Ga_{0.83}N$ barrier-layer is revealed by analyzing the XRD-RSMs (see Figures B.2b-c). This result in in good agreement with the HRTEM study (Figure B.3.), which shows a coherent GaN/$Al_{0.17}Ga_{0.83}N$ interface. However the thin barrier-layer is below the 100 nm resolution limit of the presented ILR study.

This nearly perfect epitaxial barrier-layer is achieved by a successive improvement of the sublayer crystal quality through all layers as shown in the TD-density study. The comparison of Table B.1. shows, that although the edge TD-density does not change much between the $Al_{0.32}Ga_{0.68}N$ and GaN sublayer, the number of screw TD decreases significantly within the GaN layer. However the total number of edge TD is underestimated, due to the limited penetration depth in GID and the lower TD-density on the sublayer top.

The TD-density of the 20 nm thick barrier-layer cannot be determined quantitatively by using WH-plots. Nevertheless the comparison of the peak widths (see Figures B.2c-d) gives a qualitative information on the TD-density. Since the $Al_{0.17}Ga_{0.83}N$ peak is 15% narrower than the GaN peak a reduced TD-density can be concluded.

B.4 Conclusion

To summarize, in the presented study we have performed the characterization of an $Al_xGa_{1-x}N$ heterostructure via XRD combined with ILR and TEM analyses. Despite the weak diffraction intensity of the 20 nm $Al_{0.17}Ga_{0.83}N$ barrier-layer, a pseudomorphic GaN/$Al_{0.17}Ga_{0.83}N$ interface and the crystal quality of the crucial last few GaN monolayers were revealed. The sublayer stress gradients and the mean stress values of the ILR and the XRD analyses match qualitatively and quantitatively well with the TEM structure

characterization. Remarkably, the results show that laboratory XRD tends to underestimate pronounced local stress concentrations, which can be however resolved by the ILR approach. The 100 nm resolution of the ILR study reveals the stress evolution *within* single layers, which is not possible with lab XRD systems alone. Generally the described combination of these three techniques can be applied to many other semiconductor multilayer systems.

Acknowledgment

This work was jointly funded by the Austrian Research Promotion Agency (FFG, Project No. 854247) and the Carinthian Economic Promotion Fund (KWF, contract KWF-1521/28101/40388). Financial support by the Austrian Federal Government (in particular from the Bundesministerium für Verkehr, Innovation und Technologie and Bundes-ministerium für Wissenschaft, Forschung und Wirtschaft) represented by Österreichische Forschungs-förderungsgesellschaft mbH and the Styrian and the Tyrolean Provincial Government, represented by Steirische Wirtschaftsförderungsgesellschaft mbH and Standortagentur Tirol, within the framework of the COMET Funding Programme is gratefully acknowledged.

References

[1] D. Zhu, D.J. Wallis, and C.J. Humphreys, *Rep. Prog. Phys.* **76**, 106501 (2013).

[2] S.H. Jang and C.R. Lee, *J. Cryst. Growth* **253**, 64 (2003).

[3] H.F. Liu, S.B. Dolmanan, L. Zhang, S.J. Chua, D.Z. Chi, M. Heuken, and S. Tripathy, *J. Appl. Phys.* **113**, 023510 (2013).

[4] M.A. Moram and M.E. Vickers, *Reports Prog. Phys.* **72**, 36502 (2009).

[5] H.-P. Lee, J. Perozek, L.D. Rosario, and C. Bayram, *Sci. Rep.* **6**, 37588 (2016).

[6] S. Tripathy, V.K.X. Lin, S. Vicknesh, and S.J. Chua, *J. Appl. Phys.* **101**, 063525 (2007).

[7] M. Jamil, J.R. Grandusky, V. Jindal, F. Shahedipour-Sandvik, S. Guha, and M. Arif, *Appl. Phys. Lett.* **87**, 17 082103 (2005).

[8] M. Reisinger, J. Zalesak, R. Daniel, M. Tomberger, J.K. Weiss, A.D. Darbal, M. Petrenec, J. Zechner, I. Daumiller, W. Ecker, B. Sartory, and J. Keckes, *Mater. Des.* **106**, 476 (2016).

[9] R. Treml, D. Kozic, J. Zechner, X. Maeder, B. Sartory, H.P. Gänser, R. Schöngrundner, J. Michler, R. Brunner, and D. Kiener, *Acta Mater.* **103**, 616 (2016).

[10] Y. Cordier, N. Baron, F. Semond, J. Massies, M. Binetti, B. Henninger, M. Besendahl, and T. Zettler, *J. Cryst. Growth* **301–302**, 71 (2007).

[11] F. Brunner, A. Knauer, T. Schenk, M. Weyers, and J.T. Zettler, *J. Cryst. Growth* **310**, 2432 (2008).

[12] Y.Y. Wang, D. Cooper, J. Rouviere, C.E. Murray, N. Bernier, and J. Bruley*, Appl. Phys. Lett.* **106**, 042104 (2015).

[13] M.J. Hÿtch and F. Houdellier, *Microelectron. Eng.* **84**, 460 (2007).

[14] P.F. Fewster*, Crit. Rev. Solid State Mater. Sci*. **22**, 69 (1997).

[15] W. Zhu, S. Park, Y. Okumura, A. Leto, and G. Pezzotti, *J. Appl. Phys.* **112**, 053522 (2012).

[16] T. Konya, Rigaku J. **25**, 1 (2009). available at http://chemport.cas.org/cgi-bin/sdcgi?APP=ftslink&action=reflink&origin=aip&version=1.0&coi=1%3ACAS%3A528%3ADC%252BD1MXhtlWlsbfL&md5=99b5a2e509618 2c866ec53c15e811527.

[17] U. Pietsch, V. Holy, and T. Baumbach, *High Resolution X-Ray Scattering* (Springer, New York, 2004).

[18] A. Kadir, C.C. Huang, K.E.K. Lee, E.A. Fitzgerald, and S.J. Chua, *Appl. Phys. Lett.* **105**, 232113 (2014).

[19] A. Polian, M. Grimsditch, and I. Grzegory, *J. Appl. Phys.* **79**, 3343 (1996).

[20] A.F. Wright, *J. Appl. Phys.* **82**, 2833 (1997).

[21] T. Metzger, R. Höpler, E. Born, O. Ambacher, M. Stutzmann, R. Stömmer, M. Schuster, H. Göbel, S. Christiansen, M. Albrecht, and H.P. Strunk, *Philos. Mag. A.* **77**, 1013 (1998).

[22] S. Lazarev, S. Bauer, K. Forghani, M. Barchuk, F. Scholz, and T. Baumbach, *J. Cryst. Growth* **370**, 51 (2013).

[23] S.R. Lee, D.D. Koleske, K.C. Cross, J.A. Floro, K.E. Waldrip, A.T. Wise, and S. Mahajan, *Appl. Phys. Lett.* **85**, 6164 (2004).

[24] D. Holec, Y. Zhang, D.V.S. Rao, M.J. Kappers, C. McAleese, and C.J. Humphreys, *J. Appl. Phys.* **104**, 123514 (2008).

[25] H. Heinke, S. Einfeldt, B. Kuhn-Heinrich, G. Plahl, M.O. Moller, and G. Landwehr, *J. Phys. D. Appl. Phys.* **28**, A104 (1995).

[26] S. Raghavan, I.C. Manning, X. Weng, and J.M. Redwing, *J. Cryst. Growth* **359**, 35 (2012).

[27] D.M. Follstaedt, S.R. Lee, A.A. Allerman, and J.A. Floro, *J. Appl. Phys*. **105**, 083507 (2009).

[28] J.D. Acord, I.C. Manning, X. Weng, D.W. Snyder, and J.M. Redwing, *Appl. Phys. Lett.* **93**, 111910 (2008).

[29] A.E. Romanov and J.S. Speck, *Appl. Phys. Lett.* **83**, 2569 (2003).

[30] R.F. Davis, S. Einfeldt, E.A. Preble, A.M. Roskowski, Z.J. Reitmeier, and P.Q. Miraglia, *Acta Mater.* **51**, 5961 (2003).

[31] L.R. Snyder, J.J. Kirkland, and J.L. Glajch, *Practical HPLC Method Development* (John Wiley & Sons, New York, 1997).

[32] P. Cantu, F. Wu, P. Waltereit, S. Keller, A.E. Romanov, S.P. DenBaars, and J.S. Speck, *J. Appl. Phys*. **97**, 103534 (2005).

B.5 Supplementary Material

Lattice constant and strain determination

The sublayer lattice constants *a* and *c* were deduced from the q_x-q_z values of the peak positions in the RSMs using equation B-S1 according to Ref.1,

$$q_{hkl} = \frac{1}{d_{hkl}} = \sqrt{\frac{4\,(h^2+k^2+hl)}{3a^2} + \frac{l^2}{c^2}} \qquad \text{(B-S1)}$$

where q_{hkl} and d_{hkl} are the reciprocal space vector and the corresponding interplanar spacing of the lattice plane *(hkl)*. The reciprocal vector q_{hkl} was separated into an in-plane q_x ($l = 0$) and an out-of-plane q_z ($h = 0$, $k = 0$) component.[1]

The sublayer in-plane and out-of-plane strain values (ε_{xx}, ε_{zz}) were calculated applying equations (B-S2) (B-S3),

$$\varepsilon_{xx} = \frac{a_{exp} - a_0}{a_0} \quad \text{(B-S2)}, \qquad \rightarrow \varepsilon_{zz} = \frac{c_{exp} - c_0}{c_0} \quad \text{(B-S3)}$$

where the subscripts *"0"* and *"exp"* refer to the unstrained and measured lattice parameter values.[2] The unstrained AlN and GaN reference values were taken from literature, whereas the references of the $Al_xGa_{1-x}N$ layers were determined by using Vegard's law and the lattice parameters of the composition components AlN and GaN.[2]

Relaxation parameter from lattice parameter

Pereira *et. al.* have used following relationships (B-S4 – B-S6) in order to determine the relaxation line for [001] orientated hexagonal structures:[3]

$$\varepsilon_{zz} = -D(x)\varepsilon_{xx} \quad \text{(B-S4)}, \qquad D(x) = 2\frac{c_{13}(x)}{c_{33}(x)} \quad \text{(B-S5)}$$

$$\alpha\,(x) = arctan\left(\frac{1}{D(x)} \cdot \frac{c}{a}\sqrt{\frac{4}{3}\frac{(h^2+hk+l^2)}{l^2}} \cdot \frac{4\,(h^2+k^2)}{l\sqrt{4/3(h^2+hk+l^2)}}\right) \quad \text{(B-S6)}$$

with c_{13} *(x)*, c_{33} *(x)* as the elastic constants of the strained $Al_xGa_{1-x}N$ sublayer, $\varepsilon_{xx}/\varepsilon_{zz}$ as the in-plane/out-of-plane strain values and α as the angle between the reciprocal surface normal vector (shown in Figure B.1b).

The relaxation parameter γ, which quantifies the strain caused relaxation, was calculated by equation B-S7:[4]

$$\frac{a_{exp}(L_2) - a_0(L_1)}{a_0(L_1)} = \frac{a_0(L_2) - a_0(L_1)}{a_0(L_1)}(1-\gamma) \quad \text{(B-S7)}$$

Here L_2 stands for the strained epitaxial layer, which grows above the substrate layer L_1.

Threading Dislocations densities from Williams-Hall plots

The dislocation broadening and correlation length broadening can be graphically separated by using a Williamson-Hall-Plot (WH-Plot), where $\beta\ (\sin\Theta)/\lambda$ was plotted against $(\sin\Theta)/\lambda$ for the different scattering orders of the in-plane and out-of-plane sublayer reflections (see Figure B-S1.). Here β is the reflection full width half maxima in direction of the incident angle obtained by Gaussian peak fitting, 2Θ is the diffraction angle and λ is the X-ray wavelength. Based on the fact that the dislocation induced broadening increases with increasing scattering order, whereas the correlation length broadening is independent of the scattering order, the slopes of the linear fitted (*h*00) and (00*l*) data points give the crystal twist angle (α_Φ) and tilt angle (α_Ω).[5] The tilt and twist values of the AlN (α_Φ = 0.0221°, α_Ω = 0.0116°), $Al_{0.32}Ga_{0.68}N$ (α_Φ = 0.0149°, α_Ω = 0.00613°) and GaN (α_Φ = 0.0146°, α_Ω = 0.00297°) sublayers were used in order to calculate the edge and screw TDs (N_E and N_S) via equations (B-S8) and (B-S9):[6]

$$N_E = \frac{\alpha_\Phi^2}{4.35\ b_E^2} \quad \text{(B-S8)}, \qquad N_S = \frac{\alpha_\Omega^2}{4.35\ b_S^2} \quad \text{(B-S9)}$$

with b_E and b_S as the Burgers vector lengths of the edge and screw typed TDs.

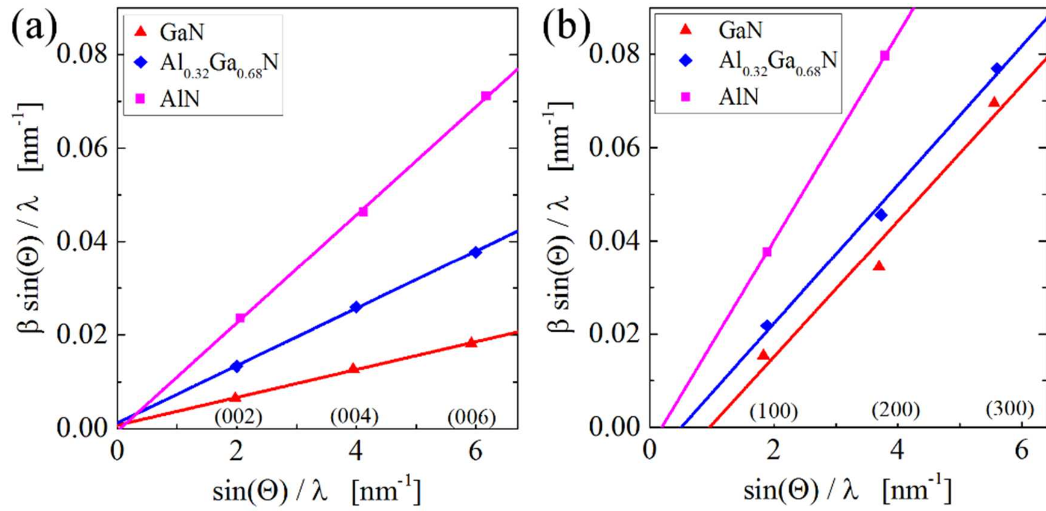

Figure B-S1.: The Williamson-Hall-Plots for the (*h*00) (a) and (00*l*) (b) reflections of the AlN, $Al_{0.32}Ga_{0.68}N$ and GaN sublayer are shown. Due to the little scattering volume, the $Al_{0.17}Ga_{0.83}N$ layer reflections are too weak for the Williamson-Hall-Plot analysis.

Quantification of Peak Asymmetry

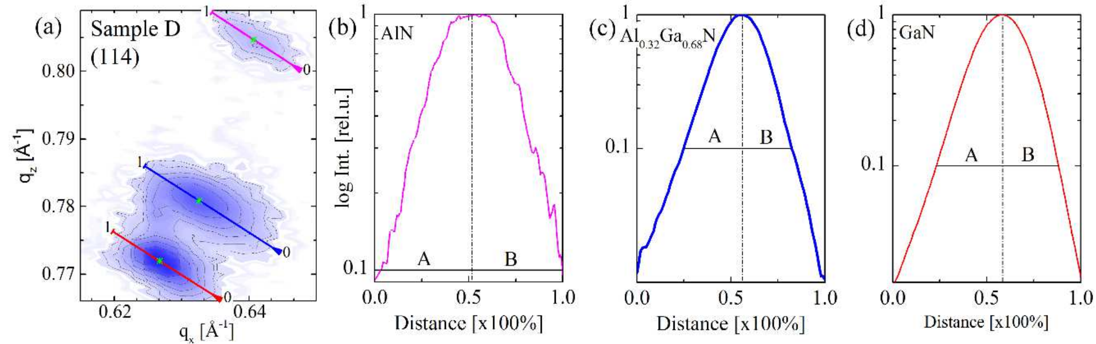

Figure B-S2.: (a) The positions and the origins of the RLP line cuts for the AlN, $Al_{0.32}Ga_{0.68}N$ and GaN sublayers are shown. The normalized intensity distribution is plotted against the normalized line cut length for the AlN (b), $Al_{0.32}Ga_{0.68}N$ (c) and GaN (d) peak. Lengths *A* and *B* represent the left and the right peak width at 0.1 height.

	A (-)	***B*** (-)	***A_f*** (-)
AlN	0.382	0.397	0.97
$Al_{0.32}Ga_{0.68}N$	0.233	0.207	1.13
GaN	0.281	0.252	1.12

Table B-S1: The *A*, *B* and A_f values of the AlN, $Al_{0.32}Ga_{0.68}N$ and GaN sublayer are listed. A_f is the asymmetry factor which is given by the ratio between *A* and *B*.

ILR Misalignment

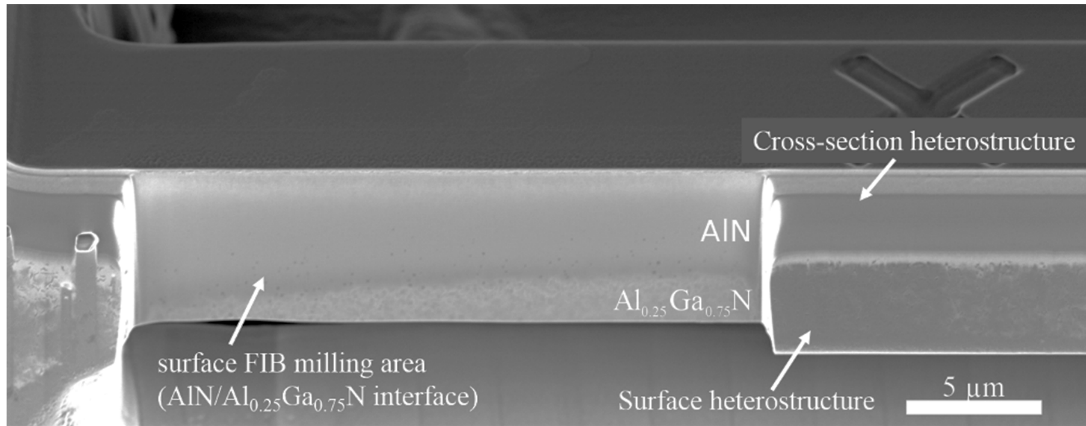

Figure B-S3.: SEM image of the FIB milling area of the ILR cantilever. Due to minor misalignment of the ILR cantilever with respect to the gallium beam direction, the cutting surface is slightly tilted with respect to the interface. Consequently the $Al_{0.25}Ga_{0.75}N$ layer is partially removed and the ILR data point next to the AlN/$Al_{0.25}Ga_{0.75}N$ interface represents average information of both sublayers.

References

[1] A. Kadir, C.C. Huang, K.E.K. Lee, E.A. Fitzgerald, and S.J. Chua, *Appl. Phys. Lett.* **105**, 232113 (2014).

[2] H.-P. Lee, J. Perozek, L.D. Rosario, and C. Bayram, *Sci. Rep*. **6**, 37588 (2016).

[3] S. Pereira, M.R. Correia, E. Pereira, K.P. O'Donnell, E. Alves, A.D. Sequeira, N. Franco, I.M. Watson, and C.J. Deatcher, *Appl. Phys. Lett.* **80**, 3913 (2002).

[4] H. Heinke, S. Einfeldt, B. Kuhn-Heinrich, G. Plahl, M.O. Moller, and G. Landwehr, *J. Phys. D. Appl. Phys*. **28**, A104 (1995).

[5] T. Metzger, R. Höpler, E. Born, O. Ambacher, M. Stutzmann, R. Stömmer, M. Schuster, H. Göbel, S. Christiansen, M. Albrecht, and H.P. Strunk, Philos. *Mag. A.* **77**, 1013 (1998).

[6] C. Dunn and E. Kogh, *Acta Metall.* **5**, 548 (1957).

Matching *in-situ* and *ex-situ* recorded stress gradients in an $Al_xGa_{1-x}N$ heterostructure: Complementary wafer curvature analyses in time and space

M. Reisinger [a], C. Ostermaier [b], M. Tomberger [b], J. Zechner [c], B. Sartory [d], W. Ecker [d], I. Daumiller [b], J. Keckes [a]

[a] Department of Materials Physics, Montanuniversitaet Leoben, Franz Josef-Straße 18, 8700 Leoben, Austria

[b] Infineon Technologies Austria AG, Siemensstraße 2, 9500 Villach, Austria

[c] KAI Kompetenzzentrum Automobil- u. Industrieelektronik GmbH, Europastraße 8, 9524 Villach, Austria

[d] Materials Center Leoben Forschung GmbH, Roseggerstraße 12, 8700 Leoben, Austria

Abstract

In-situ wafer curvature measurements and *ex-situ* ion-beam layer removal method are used to evaluate residual stress depth profiles in a 1.8 µm thick $Al_xGa_{1-x}N$ heterostructure on Si(111) by evaluating substrate surface curvatures and deflections of stepwise ion-beam milled micro-cantilevers, respectively. Both approaches reveal oscillatory stress depth gradients which correlate excellent in their depth alternations. Differences are found locally in the magnitudes of the stress concentrations, especially in the regions with relatively large stresses, inhomogeneous microstructures and at relatively small thicknesses. The

discrepancies are interpreted by local stress relaxations in the growing heterostructure, like dislocation formation and overgrowth by differently stressed regions.

C.1 Introduction

The knowledge of residual stress depth gradients in thin films is of great importance in all stages of their synthesis and applications. The gradients influence decisively mechanical and structural integrity of the films as well as the lifetime and functional parameters of the components [1]. There are numerous experimental techniques to assess the stress gradients *ex-situ* after film deposition, like X-ray diffraction, Raman spectroscopy, transmission electron microscopy and recently introduced ion beam layer removal (ILR) approach [2,3]. ILR is based on a stepwise focused ion beam (FIB) thinning of micro-cantilevers, which consist of a thin film and a certain portion of a substrate. The stress depth gradient is obtained using finite-element (FE) simulation considering the cantilever deflection changes after the ion milling steps as well as the film and substrate elastic constants. Remarkable features of ILR are (i) the need for the use of a monocrystalline substrate of known mechanical properties, which does not undergo plastic deformation during the FIB milling, and (ii) the fact that the characterization is performed *ex-situ* after the film deposition in scanning electron microscope (SEM). ILR studies were reported for polycrystalline, epitaxial as well as amorphous as-deposited thin films [4,5].

In-situ characterization of stress development during thin films deposition represents a complementary approach, which is based on *in-situ* monitoring of wafer curvature (WC) performed usually using optical or capacitance approaches [6]. WC allows assessing “direct” real time stress evolution as a function of time and the actual thin film thickness, whereby the stress magnitudes are evaluated using Stoney’s equation and/or quasi-analytically. WC was applied to study fundamental processes in growing thin films like nucleation, island coalescence, the influence of sublayer sequences and surface diffusion [7–9]. WC cannot be used to resolve directly stress gradient changes occurring in already grown film and/or during cooling from deposition to room temperature [10]. Nevertheless among others, WC was extensively used to monitor strain and indirectly also

microstructural developments during the growth of group-III-nitride heterostructures, especially GaN, on silicon [11]. Here, the large lattice mismatch of ~17% and the large mismatch of coefficients of thermal expansion (CTEs) of ~−56% between Si and GaN result in a generation of pronounced stress gradients, which may result in serious reliability issues [12].

It is obvious that a comparison of *in-situ* and *ex-situ* recorded residual stress profiles obtained using WC and ILR methods, respectively, possesses not only a methodological potential to verify the two approaches but could also open a way to analyze stress gradient evolution, which occurs at during film growth at high temperatures and while cooling from deposition to room temperature, *e.g.* as a result of various diffusion-driven processes, sublayer overgrowth and plastic deformation.

In this manuscript, a residual stress gradient in a 1.8 μm thick $Al_xGa_{1-x}N$ heteroepitaxial structure is evaluated *in-situ* using WC during metallic-organic chemical vapor deposition on Si(111) substrate as well as *ex-situ* after the deposition using ILR. The aim is to compare both stress profiles, discuss the discrepancies as well as further potential for the application of both complementary approaches.

C.2 Experiment

The investigated $Al_xGa_{1-x}N$ multilayer structure was grown in an Aixtron G5 planetary reactor by using trimethylaluminum (TMA), trimethylgallium (TMG) and ammonia (NH_3) as precursors for aluminum, gallium and nitrogen, respectively. After the reactor heating followed by the annealing and simultaneous degreasing of the Si substrate, a ~ 30 nm thick low temperature (LT)-AlN nucleation layer was grown at 993°C. Subsequently the temperature was increased to 1100°C and a ~120 nm thick high temperature (HT)-AlN layer was deposited. The following ~500 nm thick $Al_{0.25}Ga_{0.75}N$ transition layer was grown at 1086°C. At the beginning of the ~1130 nm GaN buffer layer small temperature fluctuations levels off at 1100°C in order to enable a steady layer growth. After the deposition of the final ~20 nm thick $Al_{0.22}Ga_{0.78}N$ barrier layer at 1083°C, the reactor was cooled down to the room temperature. During the entire deposition process an integrated

LAYTEC Epi TT system recorded the actual wafer bow as well as the surface temperature at the center of the wafer (Figure C.1.).

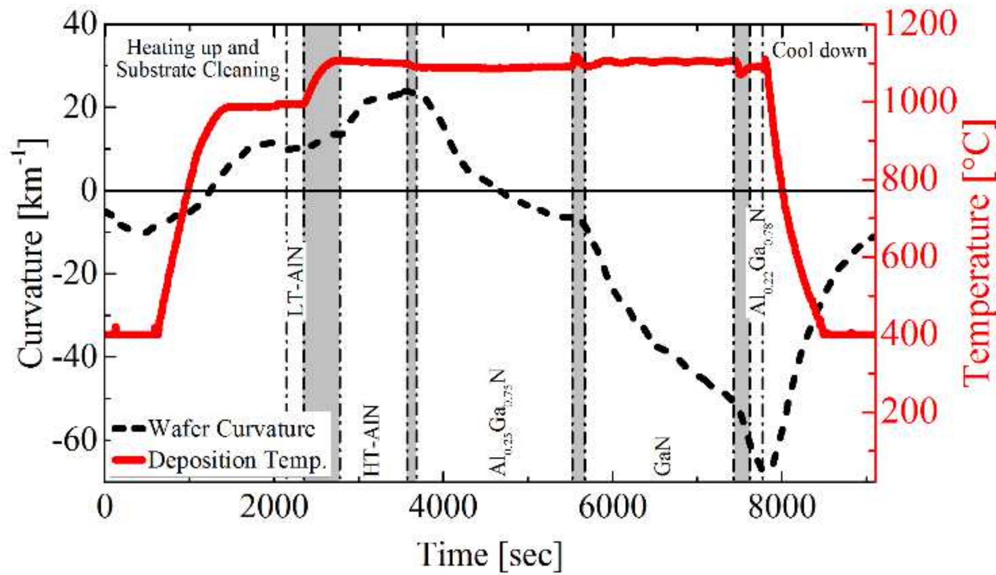

Figure C.1.: *In-situ* recorded wafer curvature (dashed line) and temperature (solid line) data collected during the sample deposition. The grey regions indicate time intervals of changing growth parameters like precursors, composition as well as reactor pressure and temperature.

Complementary, the stress gradient in the as-deposited AlN/$Al_{0.25}Ga_{0.75}N$/ GaN/$Al_{0.22}Ga_{0.78}N$ heterostructure was characterized using ILR *ex-situ*. The sample was taken from the same wafer position at which the WC data were collected (Figure C.1.). The entire measurement was carried out in a Zeiss Auriga workstation, which combines a gallium operating FIB and a high resolution SEM. Figure C.2a shows the free standing micro-cantilever, which consists of the Si substrate and the $Al_xGa_{1-x}N$ heterostructure, after performing the ILR analysis. In this perspective overview image the top face shows the heterostructure cross-section and the front face belongs to the heterostructure surface. Owing to the residual stress within the heterostructure, the micro-cantilever is bent. During the ILR experiment, the cantilever was gradually thinned in steps of ~100 nm in section A (Figure C.2.) and the cantilever deflection was evaluated after every milling step by comparing the mutual positions of two reference markers in section B (Figure C.2.). At

every milling step, the recorded cantilever deflection corresponds to the curvature of the section A, which depends on the “remaining” residual stress gradient in the heterostructure and the heterostructure thickness. Figures C.2b-c show the initial cantilever cross-section and the corresponding deflection (δ_1), whereas SEM images in Figures C.2d-e show sections A and B after the sixteen milling steps and the cantilever deflection δ_2. In order to avoid any significant sample beam damage, the FIB workstation was operated at a high voltage of 30 kV and relative low ion current of 50 pA during the entire experiment. Finally, the residual stress gradient $\sigma_{\mathrm{ILR}}(z)$ as a function of the distance z to the Si substrate in the as-deposited heterostructure was evaluated from the recorded cantilever deflections and the remaining film thickness data by using a three dimensional finite element model (FEM).

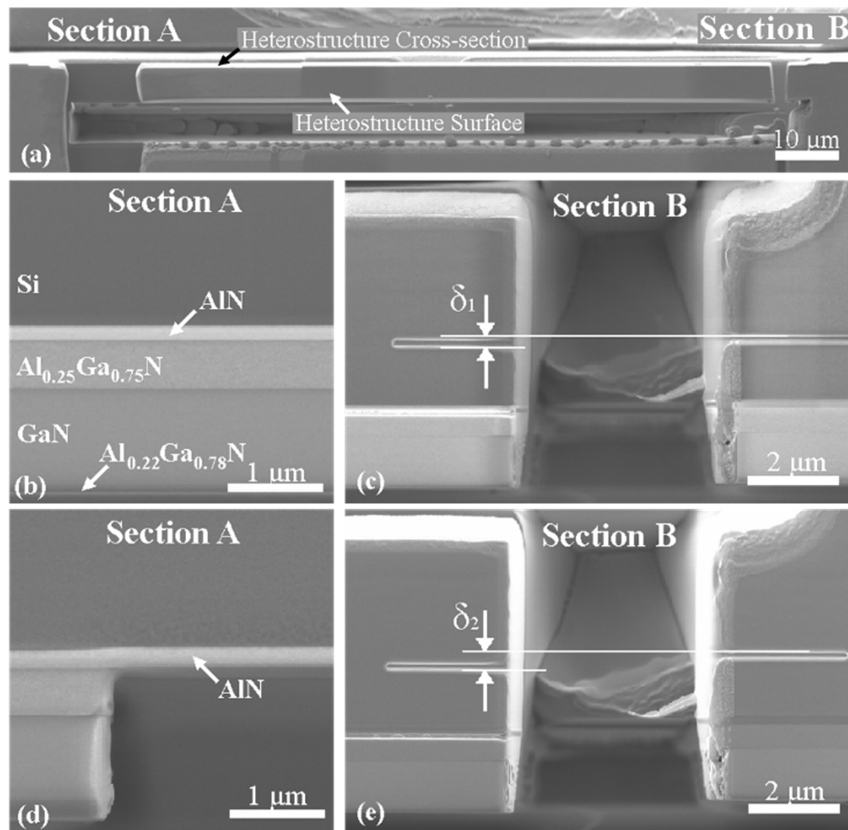

Figure C.2.: (a) SEM micrographs from the FIB machined cantilever consisting of the $Al_xGa_{1-x}N$ stack and Si substrate. The cantilever is thinned in steps of 100 nm in the section A and the cantilever deflections are recorded by monitoring the mutual positions of the two markers in the section B. The correlation of the remaining stack thickness and the deflection δ are used to evaluate stress profile in the stack. The cross-sectional views of Sections A and B show the remaining heterostructure and the cantilever deflection at the beginning (b-c) and after sixteen milling steps (d-e).

C.3 Results and Discussion

Figure C.1 displays the *in-situ* measured wafer curvature (κ) and the actual deposition temperature (T_D) data as a function of process time (t). In this chart all important process stages are indicated, whereby the grey highlighted regions correspond to the applied changes in the deposition parameters, like the reactor temperature and the partial pressures

of the precursors, which were changed between the individual sublayer growth periods. Consequently, the curvature changes within these ramping periods are mainly triggered by process adjustments rather than residual stress changes. The blue curve in Figure C.3. correlates the recorded wafer curvature κ to the actual film thickness h_f, which has been calculated under the assumption of a steady sublayer growth rate. At the beginning of the film growth (at $t \cong 2094$ sec) the recorded curvature κ was nonzero and therefore the recorded value of ~13.5 km^{-1} was considered as an offset and subtracted from the entire $\kappa(h_f)$ dependence used for the further evaluation of stresses. Additionally it was assumed that no significant film growth and changes in the heterostructure thickness occurred within the grey highlighted ramping periods.

The magnitudes and the slopes of the $\kappa(h_f)$ dependence in Figure C.3. provide important indications on the stress nature and the stress development in the growing heterostructure. Whereby positive and negative $\kappa(h_f)$ magnitudes indicate the presence of overall tensile and compressive stresses in the growing heterostructure, respectively, positive and negative slopes $\partial\kappa(h_\mathrm{f})/\partial h_\mathrm{f}$ correspond to the generation of tensile and compressive stresses at the actual stages of the heterostructure evolution, respectively [13].

Consequently at every process time t, the *in-situ* recorded curvature data $\kappa(t)$ (Figure C.1) were used to evaluate the actual average residual stresses $\langle\sigma(h_\mathrm{f})\rangle$ as a function of the actual film thickness h_f using the Stoney's equation as follows [6].

$$\langle\sigma(h_\mathrm{f})\rangle = \frac{1}{h_\mathrm{f}(t)} \frac{M_s h_s^2}{6} \kappa(t) \qquad \text{(C.1)}$$

where M_s represents the substrate in-plane biaxial modulus of 229 GPa and h_s is the substrate thickness of 675 µm.

In case there are no significant changes in the residual stress gradient $\sigma_\mathrm{WC}(z)$ in the growing film during the deposition, the average residual stress values $\langle\sigma(h_\mathrm{f})\rangle$ at the actual film thickness h_f can be expressed as follows [6]:

$$\langle \sigma(h_{\mathrm{f}}) \rangle = \frac{1}{h_{\mathrm{f}}} \int_{0}^{h_{\mathrm{f}}} \sigma_{\mathrm{WC}}(z)\ dz \tag{C.2}$$

On basis of Eq. C.2. the residual stress gradient $\sigma_{\mathrm{WC}}(z)$ was obtained by evaluating $\partial(\langle \sigma(h_{\mathrm{f}}) \rangle \cdot h_{\mathrm{f}}) / \partial h_{\mathrm{f}}$. Hence, the stress-thickness parameter $\langle \sigma(h_{\mathrm{f}}) \rangle \cdot h_{\mathrm{f}}$ was determined from the recorded curvature data and plotted in Figure C.3.

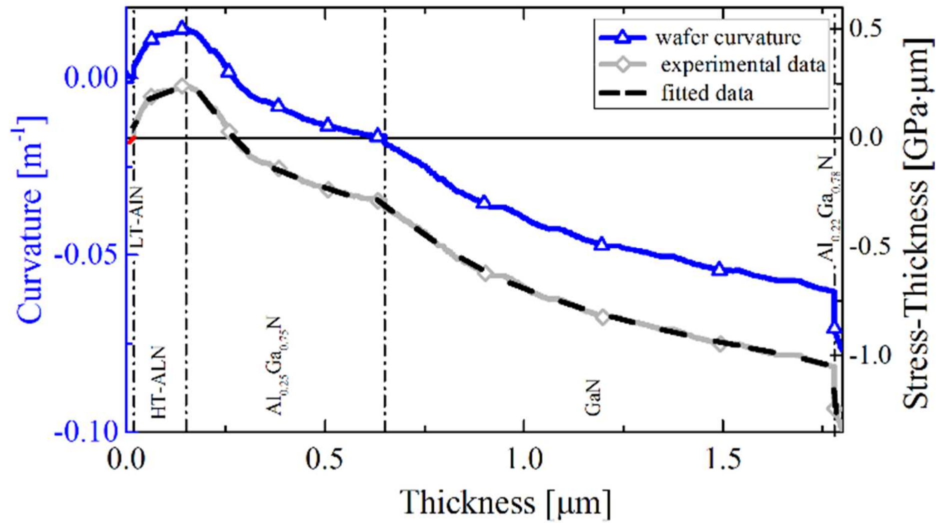

Figure C.3.: Stress-thickness and wafer curvature are plotted against the actual film thickness during the growth of the heterostructure on Si(111). The stress-thickness curve is fitted with fifth ordered polynomial function within each sublayer section.

The experimentally determined $\langle \sigma(h_{\mathrm{f}}) \rangle \cdot h_{\mathrm{f}}$ curve was fitted analytically using a fifth-order polynomial function in stepwise manner between the individual ramps. Subsequently the individual polynomial functions were then derived in order to obtain $\sigma_{\mathrm{WC}}(z)$ dependencies (Eq. C.2.) for the particular film depth regions. The residual stress gradient at room temperature $\sigma_{\mathrm{WC,RT}}(z)$ was determined by considering the curvature change during the cooling down to room temperature (Figure C.1.). Therefore the overall average heterostructure thermal stress change ($\Delta\sigma_{\mathrm{WC}} = 0.52$ GPa) was calculated via Stoney

equation and added to the residual stress gradient $\sigma_{\mathrm{WC}}(z)$ obtained via Eq. C.2. In Figure C.4., the evaluated residual stress dependencies $\sigma_{\mathrm{WC}}(z)$ and $\sigma_{\mathrm{WC,RT}}(z)$ are presented.

Complementary to the WC analysis, ILR characterization of the heterostructure was performed as discussed above and in Ref. [3]. In Figure C.4., the experimental residual stress profile obtained using ILR approach, $\sigma_{\mathrm{ILR}}(z)$ is presented together with the $\sigma_{\mathrm{WC}}(z)$ and $\sigma_{\mathrm{WC,RT}}(z)$ profiles as well as STEM micrograph of the heterostructure. Both $\sigma_{\mathrm{ILR}}(z)$ and $\sigma_{\mathrm{WC,RT}}(z)$ show very similar oscillatory residual stress profiles which differ in their magnitudes. Remarkably, with the increasing film thickness, the agreement between both profiles improves. The difference between $\sigma_{\mathrm{ILR}}(z)$ and $\sigma_{\mathrm{WC,RT}}(z)$ dependencies can be interpreted as a result of a residual stress relaxation in the growing heterostructure, especially in the near-interface region. Alternatively, another origin of this discrepancy can be the fact that the recorded experimental data of the wafer curvature $\kappa(h_{\mathrm{f}})$ in the case of WC method and/or the cantilever deflection δ and/or the remaining cantilever thickness in the case of ILR method suffer from accuracy. It can be supposed that especially $\kappa(h_{\mathrm{f}})$ and $\langle\sigma(h_{\mathrm{f}})\rangle$ dependencies (Figure C.3.) are influenced by experimental errors and contribute to the observed mismatch of the residual stresses in Figure C.4.

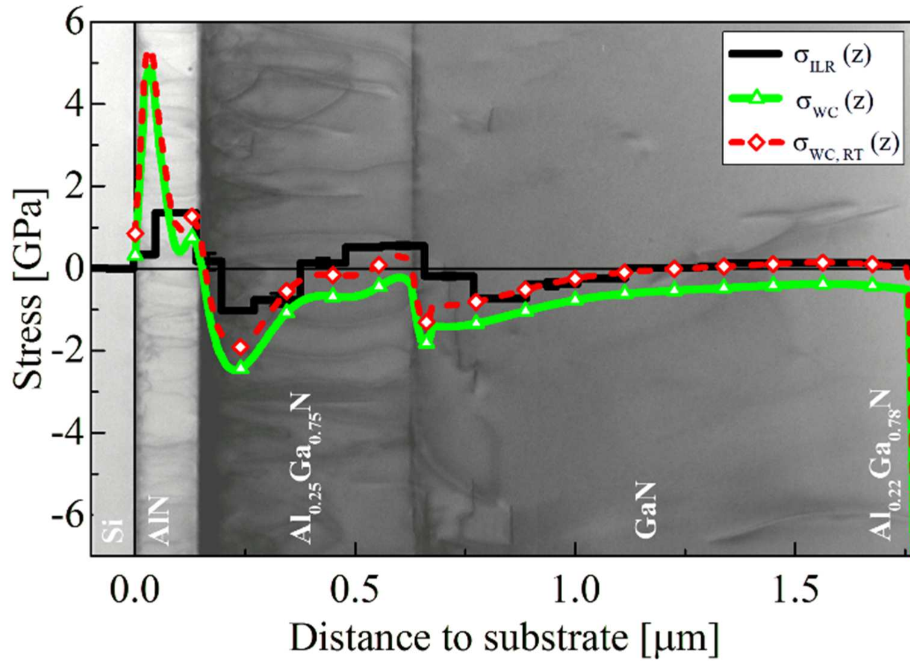

Figure C.5.: $\sigma_{\mathrm{WC}}(z)$, $\sigma_{\mathrm{WC,\,RT}}(z)$ and $\sigma_{\mathrm{ILR}}(z)$ dependencies evaluated using *in-situ* wafer curvature approach during the film deposition and *ex-situ* after the deposition using ion beam layer removal method are superimposed on a STEM micrograph. The discrepancies between both profiles indicate a presence of stress relaxation in the growing heterostructure and/or limited accuracy of the approaches.

In the ~150 nm thick AlN sublayer, WC and ILR approaches indicate the presence of high tensile stress concentrations of ~5.2 and ~1.5 GPa, respectively. These high tensile stresses are formed as result of the island coalescence during the AlN formation as well as lattice- and CTE-mismatches between AlN and Si [14]. The STEM micrograph shows a high dislocation and/or a grain boundary densities within the AlN sublayer, which rises from (i) tilt and twist misorientation of neighbouring AlN islands during the coalescence and (ii) relaxation mechanism during cooling down from the deposition to room temperature [15,16]. The mismatch between the *in-situ* and *ex-situ* recorded stress gradients $\sigma_{\mathrm{WC}}(z)$ and $\sigma_{\mathrm{WC,RT}}(z)$ can be explained by a stress relaxation in AlN sublayer during the further

heterostructure growth (after the formation of AlN sublayer was completed) and/or the cooling down process resulting in the formation of tensile thermal stresses.

In the 500 nm thick $Al_{0.25}Ga_{0.75}N$ sublayer, both approaches indicate a transition from compressive to tensile stress states. The presence of relatively high compressive stresses of a few GPa in $Al_{0.25}Ga_{0.75}N$ can be interpreted by the larger lattice parameter of this sublayer compared to AlN resulting in the specific lattice mismatch. The transition from compressive to tensile stresses can be explained by changes in the growth modes from the nucleation, three-dimensional growth and subsequent lateral overgrowth to coalescence, which is accompanied by a dislocation and/or grain boundary density decrease across the $Al_{0.25}Ga_{0.75}N$ sublayer. $\sigma_{WC,RT}(z)$ compared to $\sigma_{ILR}(z)$ exhibits approximately two times higher compressive stress concentration value of ~-2 compared to ~-1 GPa. Also in this case, the mismatch can be interpreted by the film reconstruction after the $Al_{0.25}Ga_{0.75}N$ sublayer was completed. Similar as in the case of the AlN sublayer, the high density of misfit dislocations and/or grain boundaries in the interface region of $Al_{0.25}Ga_{0.75}N$ sublayer may have contributed to the stress relaxation during the further heterostructure formation. Interestingly, the observed larger tensile stress maximum of ~0.5 GPa ($\sigma_{ILR}(z)$) compared to ~0.15 GPa ($\sigma_{WC,RT}(z)$), at the distance of ~600 nm from the substrate, indicates a tensile stress increase in $Al_{0.25}Ga_{0.75}N$ after the GaN overgrowth, which can be interpreted by (i) thermal mismatch between GaN and $Al_{0.25}Ga_{0.75}N$ during cooling and/or (ii) the presence of high compressive growth stress within the GaN sublayer interface to $Al_{0.25}Ga_{0.75}N$.

In GaN sublayer of ~1130 nm in thickness, both very similar wavy residual stress dependencies $\sigma_{WC,RT}(z)$ and $\sigma_{ILR}(z)$ exhibit a stress change from compressive to tensile, which origin can be interpreted in a similar way as in the case of $Al_{0.25}Ga_{0.75}N$ sublayer. The agreement between $\sigma_{WC,RT}(z)$ and $\sigma_{ILR}(z)$ for the stress values of 200MPa at the film thicknesses in the range of ~1250-1750 nm can be interpreted as a quantitative verification of the approaches. The agreement between $\sigma_{WC,RT}(z)$ and $\sigma_{ILR}(z)$ dependencies observed in GaN sublayer suggests indirectly that there is no significant stress relaxation, due to the

relatively small stress concentrations, resulting in a very good agreement between ILR and WC data (Figure C.4.).

The comparison of the $\sigma_{\mathrm{WC,RT}}(z)$ and $\sigma_{\mathrm{ILR}}(z)$ dependencies (Figure C.4.) documents that WC approach can be used to reconstruct the actual stress concentrations in growing thin films with the excellent depth resolution as a consequence of continuously recorded $\langle\sigma(h_{\mathrm{f}})\rangle$ data. In the case of ILR approach, however, the depth resolution is very limited by the applied FIB milling step and method laboriousness. Currently, the FIB milling steps down to ~10 nm were recorded [17]. ILR possess however an important advantage to evaluate stress gradients very locally at various lateral places of coated wafers. On the other hand, WC approach provides the in-line measurement of stress values averaged over relatively large wafer regions of mm or even cm.

C.4 Conclusion

In summary, *ex-situ* ILR and *in-situ* WC were used to evaluate residual stress profiles in a 1.8 µm thick $Al_xGa_{1-x}N$ heterostructure on Si(111) by analyzing deflections of stepwise FIB milled micro-cantilevers and wafer surface curvatures of the growing heterostructure, respectively. Both approaches reveal oscillatory stress depth dependencies, which depth-dependent alternations agree well but which defer in the local magnitudes of the stress concentrations. The latter are interpreted primarily by local stress relaxations in the growing heterostructure, like dislocation and grain boundary formation as well as overgrowth by differently stress regions. The agreement between both approaches is observed especially in regions with relatively small stress magnitudes and homogeneous microstructures and at relatively large thin film thicknesses. Finally, it can be expected that the novel approach will be used to understand stress relaxation phenomena in complex thin films and coatings.

Acknowledgment

This work was jointly funded by the Austrian Research Promotion Agency (FFG, Project No. 854247) and the Carinthian Economic Promotion Fund (KWF, Contract No. KWF-

1521/28101/40388). Financial support by the Austrian Federal Government (in particular from the Bundesministerium f€ur Verkehr, Innovation und Technologie and Bundesministerium für Wissenschaft, Forschung und Wirtschaft) represented by Österreichische Forschungs-förderungsgesellschaft mbH and the Styrian and the Tyrolean Provincial Government, represented by Steirische Wirtschaftsförderungsgesellschaft mbH and Standortagentur Tirol, within the framework of the COMET Funding Programme is gratefully acknowledged.

References

[1] E. Suhir, *J. Appl. Phys.* **110** (2011) 074505.

[2] M. Sebastiani, T. Sui, A.M. Korsunsky, *Mater. Des.* **118** (2017) 204–206.

[3] M. Reisinger, J. Zalesak, R. Daniel, M. Tomberger, J.K. Weiss, A.D. Darbal, M. Petrenec, J. Zechner, I. Daumiller, W. Ecker, B. Sartory, J. Keckes, *Mater. Des*. **106** (2016) 476–481.

[4] S. Massl, J. Keckes, R. Pippan, *Acta Mater.* **55** (2007) 4835–4844.

[5] R. Schöngrundner, R. Treml, T. Antretter, D. Kozic, W. Ecker, D. Kiener, R. Brunner, *Thin Solid Films.* **564** (2014) 321–330.

[6] J.A. Floro, E. Chason, S.R. Lee, R.D. Twesten, R.Q. Hwang, L.B. Freund, *J. Electron. Mater.* **26** (1997) 969–979.

[7] A. Krost, A. Dadgar, F. Schulze, J. Bläsing, G. Strassburger, R. Clos, A. Diez, P. Veit, T. Hempel, J. Christen, *J. Cryst. Growth.* **275** (2005) 209–216.

[8] D.S. Zolotukhin, D. V. Nechaev, S. V. Ivanov, V.N. Zhmerik, *Tech. Phys. Lett.* **43** (2017) 262–266.

[9] Y. Cordier, N. Baron, F. Semond, J. Massies, M. Binetti, B. Henninger, M. Besendahl, T. Zettler, *J. Cryst. Growth.* **301–302** (2007) 71–74.

[10] H.F. Liu, S.B. Dolmanan, L. Zhang, S.J. Chua, D.Z. Chi, M. Heuken, S. Tripathy, *J. Appl. Phys.* **113** (2013) 023510.

[11] J. Cheng, X. Yang, L. Sang, L. Guo, J. Zhang, J. Wang, C. He, L. Zhang, M. Wang, F. Xu, N. Tang, Z. Qin, X. Wang, B. Shen, *Sci. Rep*. **6** (2016) 23020.

[12] D. Zhu, D.J. Wallis, C.J. Humphreys, *Rep. Prog. Phys*. **76** (2013) 106501.

[13] J.A. Floro, S.J. Hearne, J.A. Hunter, P. Kotula, E. Chason, S.C. Seel, C. V. Thompson, *J. Appl. Phys.* **89** (2001) 4886–4897.

[14] E. V. Etzkorn, D.R. Clarke, *J. Appl. Phys.* **89** (2001) 1025–1034.

[15] S. Raghavan, J.M. Redwing, *J. Cryst. Growth*. **261** (2004) 294–300.

[16] J.A. Floro, E. Chason, R.C. Cammarata, D.J. Srolovitz, *MRS Bull.* **27** (2002) 19–25.

[17] R. Hammer, J. Todt, J. Keckes, B. Sartory, G. Parteder, J. Kraft, S. Defregger, *Mater. Des.* **132** (2017) 72-78.